On the generation of theta rhythms in the hippocampus

by

Alexandra Chatzikalymniou

A thesis submitted in conformity with the requirements
for the degree of Doctor of Philosophy
Graduate Department of Physiology
University of Toronto

Abstract

On the generation of theta rhythms in the hippocampus

Alexandra Chatzikalymniou
Doctor of Philosophy
Graduate Department of Physiology
University of Toronto
2021

A prevalent local field potential (LFP) rhythm in the CA1 hippocampus associated with memory processing and spatial navigation is the (3-12 Hz) theta oscillation. Theta rhythms emerge *intrinsically* in an *in vitro* whole hippocampus preparation. This system makes it possible to assess the contribution of different cell types, a problem that remains unresolved, in the absence of state-dependent confounding factors typically encountered *in vivo*.

To decipher the theta generation mechanism we leverage insights from minimal models in application to biologically detailed ones. We extract a piece of a previously published full CA1 model, the *segment model*, on which we test minimal model hypotheses. We distinguish the pyramidal (PYR) cells as the theta rhythm initiators whose activity is regularized by inhibitory cells supporting an 'inhibition-based tuning' mechanism. We find a strong correlation between the PYR cell input currents and the resulting theta frequency, establishing that the intrinsic PYR cell properties underpin frequency characteristics. We analyze contributions of external drives and find that strongest theta responses are generated by the hippocampus CA3 while weakest responses are induced by inputs from the CA1. Subsequently we turn our attention to the full CA1 model and explain the theta activities it produces according to our gathered insights. We demonstrate that the termination of PYR cell theta bursts relies on sequential activation of distinct inhibitory cell classes.

Two main types of inhibitory cells have been considered particularly important for the generation of theta rhythms, the parvalbumin-positive (PV+) and the somatostatin-

positive (SOM+) cells. Having demonstrated the importance of PV+ cells in theta generation, we turn to the SOM+ oriens lacunosum-moleculare (OLM) cells, a heavily studied cell class whose role is still unclear. We find that OLM cells regulate the robustness of the LFP laminar polarity profile without affecting average power, a robust response that depends on co-activation of distal inhibition and basal excitation. Finally, we estimate the spatial extent of the theta LFP, and predict that about 22,000 PYR cells participate in intrinsic theta generation. The work presented in this thesis provides a cellular-based foundation from which *in vivo* theta activities can be explored.

to my mother Evgenia Pierri,
who instilled the principles I live by
and 30 years earlier
dedicated hers to me

Acknowledgements

First and foremost I would like to thank and acknowledge my supervisor Dr. Frances Skinner an outstanding mentor whose strategic planning and organizational skills have supported a well-ordered development of my research projects throughout my degree. Dr. Skinner has offered no shortage of growth opportunities cultivating a holistic perspective of the field of Computational Neuroscience in direct interaction with the Experiment. Dr. Skinner has been a great inspiration both as a scientist and a leader while the knowledge she provided will be invaluable in years to come.

I would like to thank and acknowledge my committee members: Dr. Douglas Tweed for instilling the importance of formulating and communicating my work in a principled manner, intelligible across domains of Computational Neuroscience. I would like to thank Dr. Liang Zhang for always ensuring the biological appropriateness and realism of my biophysical models, and for bringing forth his constructive perspective as an experimentalist. I would also like to thank Dr. Martin Wojtowicz for his guidance at the early stages of my degree.

I would like to thank my colleagues: Dr. Ivan Raikov and Dr. Marianne Bezaire from the Soltesz Lab for the discussions and technical support on the CA1 microcircuit, and also Dr. Benedicte Amilhon and Dr. Jesse Jackson from the Williams Lab for introducing me to the experimental intricacies of the intact hippocampus preparation and for sharing their data.

I would like to acknowledge the members of Frances Skinner Lab for the many stimulating conversations over the years, but also for their collaborative spirit and team work ethic. In chronological order: Katie Ferguson, Vladislav Sekulic, Alexandre Guet-McCreight and Scott Rich. I would also like to acknowledge Melisa Gumus and Anton Lynuov, the summer students who contributed to my projects and publications.

I would like to acknowledge the administrative staff, Rosalie Pang and Colleen Shea from the Department of the Physiology and also Samira Patel from the Krembil Research Institute.

I would like to thank Panos Klaoudatos for his undivided encouragement throughout the years, and for fueling my persistence and determination in pursuing my academic goals. Finally, I would like to thank Aggelos Chatzikalymnios for his care and support.

Contents

List of Tables

List of Figures

Glossary of Terms and Acronyms

AAC axo-axonic cell

aCSF artificial cerebral spinal fluid

AD Alzheimer's disease

AMPA α-Amino-3-hydroxy-5-methyl-4-isoxazolepropionic acid

BC basket cell

BiC bistratified cell

CCK+ cholecystokinin-positive

CCK+BC cholecystokinin-positive basket cell

CSD current source density

DBS deep brain stimulation

DG dentate gyrus

EC entorhinal cortex

EcoG electro-corticogram

EEG electroencephalogram

EPSC excitatory postsynaptic potential

f-I frequency-current

GABA γ-aminobutyric acid

h-channel hyperpolarization-activated cation channel

h-current hyperpolarization-activated cation current

ING interneuron network gamma

IPSC inhibitory postsynaptic potential

ISI inter-spike interval

LFP local field potential

LTD long term depression

LTP long term potentiation

MEC medial entorhinal cortex

MF mossy fiber

mGluR metabotropic glutamate receptor

MS medial septum

NGF neurogliaform

ODEs ordinary differential equations

OLM oriens lacunosum-moleculare

PAC phase-amplitude coupling

PaS parasubiculum

PING pyramidal interneuron network gamma

PIR post-inhibitory rebound

PP perforant path

PRC phase response curve

PrS presubiculum

PV+ parvalbumin-positive

PV+BC parvalbumin-positive basket cell

PYR pyramidal

REM rapid eye movement

SCA schaffer collateral-associated

SC schaffer collateral

SFA spike frequency adaptation

SLM stratum lacunosum-moleculare

SOM+ somatostatin-positive

SO stratum oriens

SP stratum pyramidale

SR stratum radiatum

SPW-R sharp wave ripple

SUB subiculum

TLE temporal lobe epilepsy

VIP vasoactive intestinal peptide

"In scientific subjects, the natural remedy for dogmatism has been found in research. By temperament and training, the research worker is the antithesis of the pundit. What he is actively and constantly aware of is his ignorance, not his knowledge; the insufficiency of his concepts, of the terms and phrases in which he tries to excogitate his problems: not their final and exhaustive sufficiency. He is, therefore, usually only a good teacher for the few who wish to use their mind as a workshop, rather than a warehouse."

Sir Ronald Fisher

Rationale and Organization of the Thesis

LFPs are readily available in many recording configurations. Depending on the specific brain region, experimentalists have access to this rich signal whose information content needs yet to be revealed [60]. A prevalent LFP activity in the hippocampus is the (3-12 Hz) theta rhythm [26]. In an intact hippocampus *in vitro*, the hippocampal CA1 region was shown to possess the minimum circuitry to generate its own intrinsic theta rhythm [67]. This finding implies that the hippocampus contains the necessary circuit to produce theta rhythms. Unfortunately, the mechanism(s) responsible for the generation of the hippocampal theta rhythms are unclear. In this thesis we decipher the origin of the intrinsic hippocampus theta rhythm and unravel the cellular contributions to its generation.

To investigate the theta generation mechanism, in Chapter 3, we follow a multi-granular modelling approach in which we link two models of different biophysical detail that both produce theta activities intrinsic to the hippocampus. The first is a biophysically simplified model, referred to as the "minimal model", while the second model is a state-of-the-art biologically detailed model characterized by cell type diversity, morphologically extended cells, and experimentally derived connectivity. We examine the mechanism proposed by the minimal model and we investigate the extent to which this mechanism applies to the biologically detailed model with its extensive biological intricacies. We implement systematic comparisons of the two models and we identify commonalities and differences in their structure that could support similar or different theta generation mechanisms. We investigate a piece of the detailed model, the "segment model" according to the noted differences with the minimal, and examine how these factors control theta. Next, we test a hypothesis of the minimal model in application to the segment model which allows us to unveil the theta mechanism in the latter.

In Chapter 4, we consider the segment model embedded in the entire CA1 driven by the rest of the CA1 hippocampus and by newly discovered inputs from the SUB.

We refer to this model as the "adapted CA1 model". We fit and validate this model against experimental data and we investigate how the theta rhythms depend on each of the external drives to the network.

In Chapter 5 we leverage the insights from our previous analysis and we explain the theta generation mechanism in the full CA1 model of Bezaire and colleagues [14], a previously published detailed model of the whole CA1 hippocampus. We investigate this model and we obtain a comprehensive perspective of the inhibitory cell-type contributions to theta.

Two main classes of inhibitory cells have been considered particularly important for the generation of theta rhythms, the PV+ and the SOM+ cells. In Chapter 6, we decipher the role of an ambivalent cell type, the SOM+ OLM cell, under conditions of an ongoing intrinsic LFP theta rhythm. OLM cells can influence PYR cells through two distinct pathways: by direct inhibition of PYR cell distal dendrites, and by indirect disinhibition of PYR cell proximal dendrites. We build biophysical LFP models based on volume conductor theory, using a network of spiking inhibitory PV+BCs, BiCs and OLM cells, and a multicompartment PYR cell. We follow a reverse approach in which we predict connection probabilities between newly discovered connections of OLM and BiCs from the LFP. Subsequently we examine the effect of OLM cells to the ongoing intrinsic LFP theta rhythms.

Chapter 1

General Background

1.1 The Hippocampal formation

1.1.1 General anatomical features

The hippocampal formation is a compound structure in the medial temporal lobe of the brain. Arantius [61], first described the appearance of human hippocampal formation and gave it the name hippocampus (derived from the Greek word " $\iota\pi\pi o\kappa\alpha\mu\pi o\varsigma$" for sea horse). It has a prominent C-shaped structure bulging in the floor of the temporal horn of the lateral ventricle (Fig. 1.1). The hippocampal formation encompasses the hippocampus proper (hippocampus) the SUB, the entorhinal cortex (EC) and the dentate gyrus (DG) [3, 160]. Anatomically the hippocampus is divided into three subdivisions: CA1, CA2 and CA3 derived from their anatomical resemblance to a ram's horn (**C**ornu **A**mmonis). Based on its extrinsic connectivity, the hippocampal formation receives a vast amount of highly processed multimodal sensory information that is funneled into the hippocampal formation mainly by the EC. The EC is connected to associational neocortical areas in a reciprocal manner. Extensive hippocampal integration of sensory information is established by a largely unidirectional chain of intrinsic hippocampal projections. Our current knowledge on hippocampal connectivity and function is largely based on studies of rodents and monkeys [15]. The hippocampus is described as having an anterior and posterior part (in primates) or a septal and temporal part in rodents and other animals (Fig. 1.2). In the rat, the two hippocampi resemble a pair of bananas, joined at the stems by the commissure of fornix (also called the hippocampal commissure) [160].

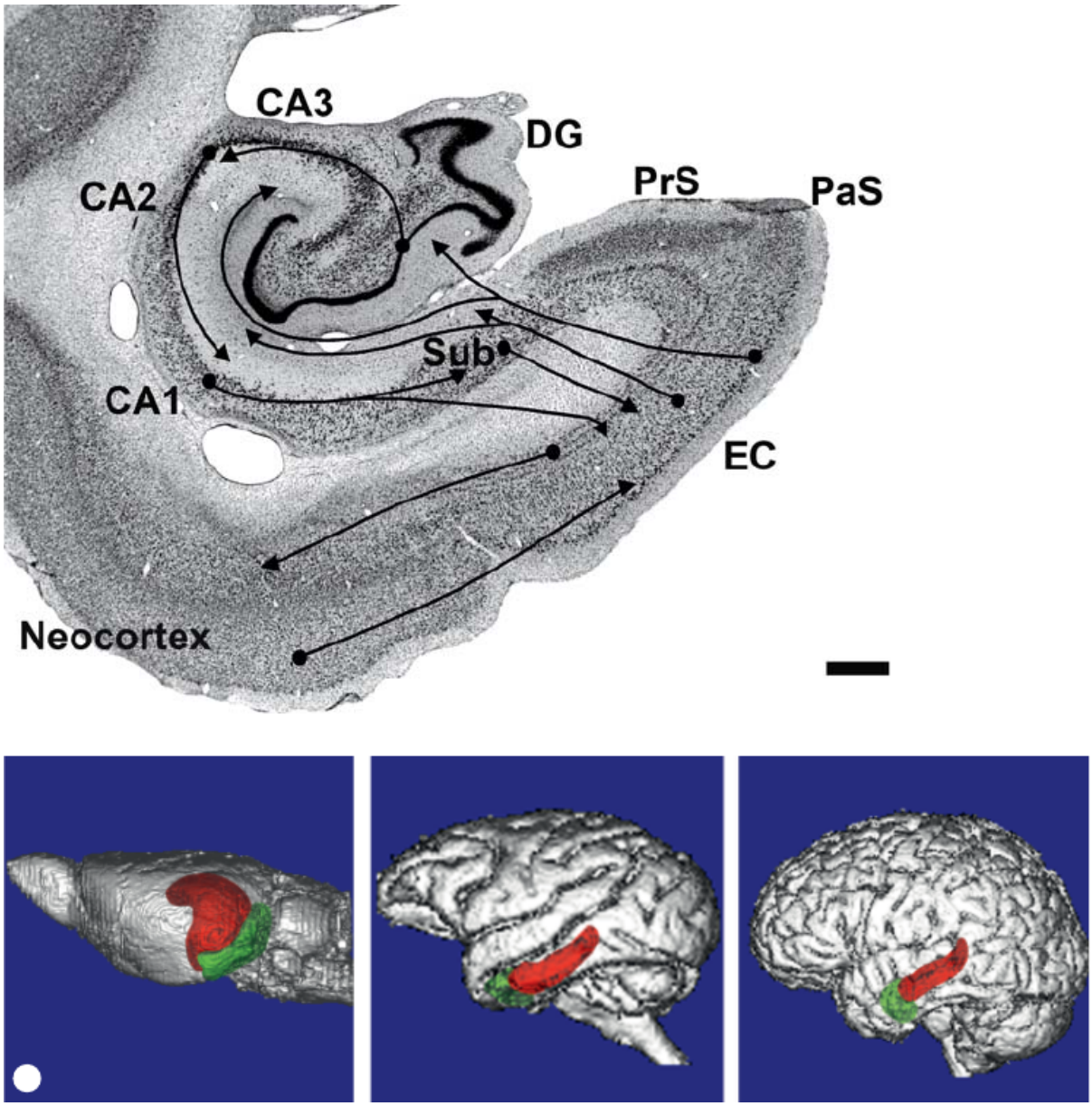

Figure 1.1: The hippocampus anatomy. Top. Schematic representation of the hierarchical organization of the main serial and parallel pathways through the different regions of the hippocampal formation. Scale bar = 1 mm. **Bottom**. MRI of rat, monkey, and human brains illustrating the relative positions of the DG + hippocampus + SUB (in red) and the EC (in green). Figure taken with permission from [1].

1.1.2 Functional role in behavior

Role in memory

The hippocampus is critical for the formation of declarative memories [27]. Its role in memory became apparent in 1957 when Scoville and Milner described the famous case of the epileptic patient H.M. (revealed to be Henry Gustav Molaison upon his death) who underwent a bilateral resection of the medial temporal lobe to treat his intractable seizures [141]. The unexpected outcome of the surgery was severe anterograde and partial retrograde amnesia; Molaison was unable to form new episodic memories after his surgery and could not remember any events that occurred just before his surgery, but he did retain memories of events that occurred many years earlier extending back into his childhood. Since then, lesion studies in animals (and particularly in rodents), have confirmed the role of the hippocampus in episodic and spatial memory [46, 119]. Furthermore, the hippocampus, and hippocampal cell activity, have been implicated in playing a large role in a number of neurological diseases associated with impaired cognition, such as epilepsy [36, 77] and Alzheimer's disease (AD) [3, 143].

Role in spatial navigation

In 1971, O'Keefe and his student Dostrovsky discovered neurons in the rat hippocampus that appeared to show activity related to the rat's location within its environment [125]. Shortly after, O'Keefe and Nadel investigated this phenomenon that eventually led to their very influential 1978 book "The Hippocampus as a Cognitive Map" [126]. There is now almost universal agreement that hippocampal function plays an important role in spatial coding, but the details are widely debated. More recently, studies on freely moving rats and mice have shown many hippocampal neurons to act as place cells that cluster in place fields, firing bursts of action potentials when the animal passes through a particular location [120]. Place cell responses are shown by PYR cells in the hippocampus and by granule cells in the DG [120]. The 2014 Nobel Prize in Physiology or Medicine was awarded to John O'Keefe for the discovery of place cells, and to Edvard and May-Britt Moser for the discovery of grid cells (`https://www.nobelprize.org/prizes/medicine/2014/advanced-information/`).

Later research has focused on trying to bridge the two main views of hippocampal function of memory and spatial cognition. In an attempt to reconcile the two views, it is suggested that a broader view of the hippocampal function is taken and seen to have a role that encompasses both the organisation of experience (mental mapping, as per Tolman's original concept in 1948 [164]) and the directional behaviour seen as being involved in

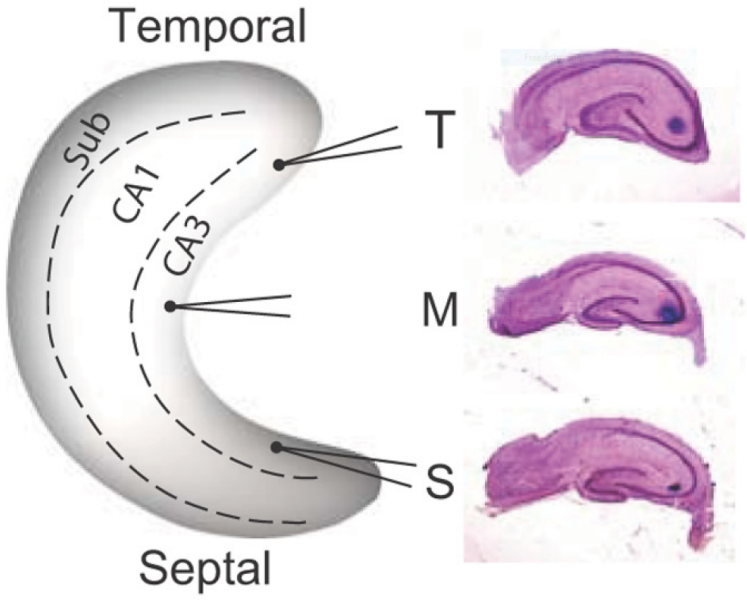

Figure 1.2: The hippocampus shape in rodents. Left. The septotemporal arrangement of the hippocampus. The CA1 is in the middle of the banana-shaped structure surrounded by the SUB on the left and and the CA3 on the right. Three recording electrodes are shown in the CA3 area septally, temporally, and in intermediate region of the intact hippocampus. **Right**. Histological verification of the recording sites. Figure adapted from [68].

all areas of cognition. That way the function of the hippocampus can be viewed as a broader system that incorporates both the memory and the spatial perspectives in its role that involves the use of a wide scope of cognitive maps [4].

1.2 The CA1 region of the rodent hippocampus

1.2.1 Anatomy

The CA1 has a structured architecture, where principal cell bodies lie in a single layer, and dendritic trees and axonal projections compose a well-defined lamina. In the CA1 region, these lamina are defined as follows: stratum oriens (SO), where the principal cell basal dendrites are aligned; stratum pyramidale (SP), the principal cell body layer; stratum radiatum (SR), the principal apical dendritic layer; and stratum lacunosum-moleculare (SLM), where the distal dendrites of the principal cells are found (Fig. 1.4). Early literature emphasized the largely unidirectional flow of information through the hippocampus, and defined the "trisynaptic circuit" as the pathways from the EC to DG,

DG to CA3, and CA3 to CA1 [175]. The trisynaptic circuit is a large over-simplification of hippocampal projections, defined in a time when the main output of the hippocampal formation was thought to be from the hippocampus proper. However, we now know that the main source of projections from the hippocampus to the neocortex is through the EC, while the SUB provides the primary subcortical projections [1]. In addition, the hippocampus may not function as unidirectionally as was once thought [84]. It's been know from older studies [94] that SUB cells target the CA1 but the inputs hadn't been quantified. In a recent study [157], the authors found common inputs to excitatory and inhibitory CA1 neurons from CA3, CA2, EC, the medial septum (MS), and unexpectedly also from the SUB, establishing the existence of a SUB-CA1 back projection pathway in contrast to the general belief of unidirectional information flow from CA1 to the SUB. In Chapter 5, we take advantage of these recently discovered connections and examine how they affect the generation of theta rhythms in the CA1.

1.2.2 Cell diversity

A large variety of interneurons exist in the CA1 and their properties have been widely investigated. The CA1 hippocampal subfield contains more than 21 types of interneurons that possess differences in morphology, electrophysiology and molecular markers [91]. Although excitatory cells outnumber inhibitory interneurons in the hippocampus, these interneurons exhibit a much wider diversity in their characteristics relative to excitatory cells [113]. Interneurons are thought to be critical for hippocampal functioning [171, 28, 19], although the precise functionality of this diversity is an ongoing challenge [178]. Hippocampal interneurons exhibit a wide diversity of morphologies, molecular expression profiles, synaptic targets, and firing properties, and are classified based on these properties [113, 114]. In a recent study [15], Bezaire and colleagues took advantage of decades of observation on the morphology, intrinsic properties, chemical markers, and connections of CA1 cell types [59] to develop a quantitative, evidence-based assessment of the number and connectivity of the vast diversity of interneurons in the CA1. They considered properties such as the arborization patterns of the dendrites and axon, the markers expressed, and the layer in which the soma is usually found [59, 127, 152], to later development a CA1 model [14] which is used as our basis in Chapters 3,4 and 5 of this thesis.

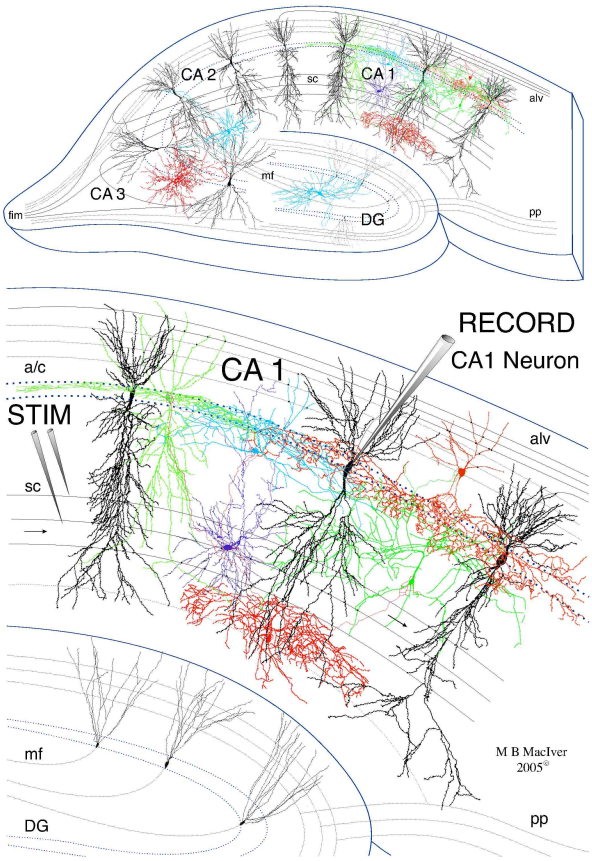

Figure 1.3: Brain slice circuitry for the CA1 area. The trisynaptic pathway (perforant path (PP) to DG, mossy fiber (MF) to CA3 and schaffer collateral (SC) to CA1) and synaptic circuit loop (PP to CA1 directly, and indirectly via DG and CA3). Projection neurons and main synaptic pathways are shown in black, inhibitory interneuron colors represent cells that function in concert (red) vs cells that belong to different inhibitory classes. By activating the appropriate interneuron class, an input can selectively control large groups of projection cells. Thus interneurons can gate or index groups of projection neurons, like CA1 PYR cells, so that sub-populations of CA1 cells can be synchronously active during theta and/or gamma frequency oscillations. Figure taken with permission from: `https://web.stanford.edu/group/maciverlab/hippocampal.html`.

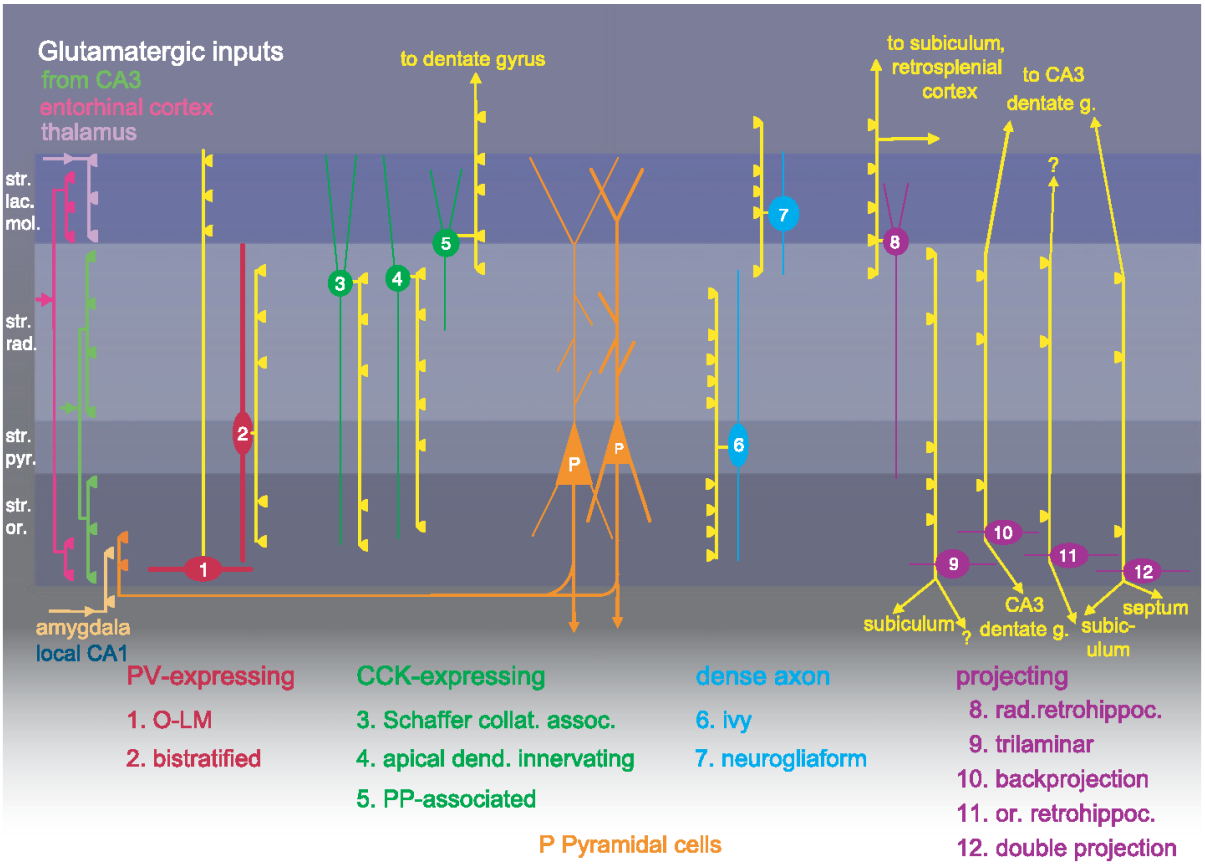

Figure 1.4: Cell diversity of the CA1. At least 12 types of GABAergic interneurons divided into four cell groups innervate dendrites of CA1 PYR cells. The main termination of five glutamatergic inputs are indicated on the left. The somata and dendrites of interneurons innervating PYR cell (orange) dendrites are coloured according to four cell groups. Axons and the main synaptic terminations are yellow. Note the association of the output synapses of different interneuron types with either the SC/commissural or the entorhinal pathway termination zones. Figure taken with permission from [91].

1.3 Theta and gamma rhythms in the CA1

Hippocampal CA1 network oscillations recordings of extracellular activity can provide essential information about underlying network dynamics and the activity of a population of neurons. The highly structured arrangement of the hippocampal formation makes it ideal for LFP recordings and analysis: the cell bodies are densely packed and the principal cell dendrites are generally arranged in parallel, producing LFP signals with a significant magnitude [3]. Extracellular recordings analyzed in conjunction with simultaneously recorded intracellular signals of individual cell types can lead to an understanding of the underlying mechanisms involved in network rhythms, and their relation to behaviour.

1.3.1 Theta rhythms

The theta oscillation (3-12 Hz) is a prominent LFP rhythm observed in mammals in a variety of brain structures (e.g. the hippocampus, the prefrontal cortex, the SUB complex, the EC, the amygdala), but is most robustly recorded from the CA1 region of the hippocampus [26]. Theta rhythms were first discovered in rabbits [95] in 1972 and have since been recorded in many species including cats, rats, mice, bats, monkeys and humans [38]. Further, they can be separated into higher or lower frequencies that are atropine-resistant or atropine-sensitive respectively [26, 38, 39].

The LFP theta rhythm is correlated with spatial navigation, episodic memory and rapid eye movement (REM) sleep [38, 39, 75]. Recent work has shown that low theta rhythms were elicited in rats with fearful stimuli and high theta with social stimuli [162]. The hippocampal theta rhythm is also associated with mechanisms of synaptic plasticity [26], and with hippocampal place cell firing [125]. What is more, disruptions of hippocampal theta rhythms are associated with memory impairments [137], and schizophrenia [101, 167].

Theta generators intrinsic to the hippocampus

A classic theta model predicts that pacemaker neurons in the MS drive the hippocampal rhythm, as septal neurons fire in synchrony with hippocampal theta, and lesions to the MS appear to remarkably reduce theta [128]. Subsequent models have included the phasic excitatory synaptic input from the EC, which plays the role of a second pacemaker [26]. However, experimental studies [67, 84], suggest that these classic models may propose a mechanism which is too simple, and that the hippocampal formation actually possesses the necessary and sufficient circuitry to generate its own theta rhythm. These studies

showed that theta rhythms emerge spontaneously at the distal CA1 in the border between the CA1 and the SUB in an intact *in vitro* hippocampus preparation (we also refer to this preparation as a "whole hippocampus" [176, 89]). Further, surgically removing the CA3 subfield confirmed that these rhythms can emerge independent of CA3 as the frequency and amplitude of the CA1 rhythms remained unchanged [67]. This preparation revealed that theta rhythms can be produced by local interactions between interneurons and PYR cells across the septo-temporal axis. While it is clear that they do not fully encompass *in vivo* theta rhythms, they undoubtedly exist without any special manipulations, and so are arguably part of the underlying biological machinery generating theta rhythms in the hippocampus.

The intrinsic rhythms recorded in CA1 are produced by networks of independent theta generators between the septal and temporal poles of the intact hippocampus. In [67], these generators were distinguished by blocking synaptic transmission between the two poles with the application of procaine, and recording simultaneously from each end of the axis. After procaine application, the authors found that the coherence of the recorded theta rhythms was significantly reduced, without altering the power of the oscillations [67]. Thus, they showed that multiple theta generators exist along the septotemporal axis indicating that theta-related information processing may vary across this axis.

The whole hippocampus preparation presents a number of benefits. Recordings of hippocampal theta rhythms *in vivo* are very dynamic as they depend on the behavioural state of the animal. Thus, confounding information makes it difficult to decipher responsible mechanisms. On the other hand, hippocampal slices may not contain the necessary circuitry required to produce theta rhythms, which may explain why these activities have not been recorded in hippocampal slices *in vitro*. All aspects considered, the whole hippocampus offers a unique opportunity to study the basis of theta mechanisms in the minimum circuitry required to produce these activities.

Mechanisms of theta rhythm generation

Insights to the mechanism of theta rhythms stem from various experimental and computational studies [78, 39]. The challenge with these studies has been that each have considered different experimental contexts and conditions. Theta rhythms are state-dependent and thus in the absence of a generalized framework, isolated observations from different groups can, at first glance, appear contradictory. Here we summarize current knowledge on theta rhythm generation and cell-type contributions to these activities.

In 2002, Gillies and colleagues [63] produced atropine resistant theta oscillations in the CA1 region of *in vitro* hippocampal slice preparations by applying a metabotropic gluta-

mate receptor (mGluR) agonist and an α-Amino-3-hydroxy-5-methyl-4-isoxazolepropionic acid (AMPA) receptor blocker [63]. During this pharmacologically induced CA1 theta oscillation they implicated OLM interneurons, and specifically the hyperpolarization-activated cation current (h-current)s in these cells, as a critical component of the generation of theta. Modelling studies supported this early view [138] but emphasized certain caveats. Using single-compartment OLM cell models with h-channel dynamics, Rotstein and colleagues [138] tested whether a network of two cells could produce network theta oscillations. They found that although their OLM cell models individually fired intrinsically at 12 Hz, the two cells could not produce a robust coherent rhythm. In later experimental studies [90], Kispersky and colleagues demonstrated, in hippocampal slice preparations, that OLM cells do not fire preferentially at theta frequencies when injected with broadband artificial synaptic inputs, but do phase-lock well to theta-modulated inputs. However, they showed that OLM cell phase-locking was not due to h-currents.

In the whole hippocampus preparation conclusive evidence came later by Amilhon and colleagues in 2015 [2]. To examine the role of specific hippocampal interneurons Amilhon and colleagues optogenetically activated and silenced interneurons expressing PV+ or SOM+. Interneurons expressing these markers are believed to be important contributors to theta generation [108, 42], with the majority of the SOM+ cells being OLM cells. Despite evidence suggesting that SOM+ interneurons are crucial for theta, optogenetic manipulation of these interneurons modestly influenced theta rhythms. In contrast, activation of PV+ enhanced theta while silencing them disrupted theta. These results demonstrated an important role for PV+ but not SOM+ interneurons for the emergence of intrinsic hippocampal theta.

Computational studies have also shed light on the theta generation mechanism in the whole hippocampus preparation. In our recent modeling study [53], Ferguson and colleagues proposed that theta emerges as a result of inhibition-mediated population bursting in a CA1 network of minimally interconnected excitatory PYR cells and fast-firing PV+ inhibitory cells. In a second study [14], Bezaire and colleagues developed a data-driven, supercomputer-based, full-scale (1:1) model of the rodent CA1 area that could spontaneously generate theta rhythms without rhythmic inputs. Their model summarized a large amount of experimental data with extensive biophysical cellular detail and empirical connectivity. It encompasses eight different γ-aminobutyric acid (GABA)ergic interneurons of the CA1. These are the PV+BCs, the BiCs, the axo-axonic cell (AAC)s, the OLM cells, the cholecystokinin-positive basket cell (CCK+BC)s, the neurogliaform (NGF) cells and the schaffer collateral-associated (SCA) cells which together constitute 70% of GABAergic interneurons in hippocampus [15]. Although this model produces in-

nate theta rhythms which arise naturally, almost unforced, due to the inclusion of enough biological detail, how they come about remains unclear. As it is mostly the case with biologically realistic models, the inherent computational complexity makes this model computationally expensive. In fact, depending on the supercomputer resources available to a given research group, carrying out even a handful of simulations of this model can be infeasible. Indicatively, for a four second simulation, the full-scale CA1 model requires 3–4 terabytes of RAM and four hours of execution time on a supercomputer using 3000 processors (or up to 12 hr for simulations calculating a high-accuracy LFP analog) [13]. The CA1 microcircuit [14] is in fact the greatest in size and biological complexity model of the CA1 hippocampus currently that produces theta rhythms. In this thesis, we propose a systematic approach for the investigation of this computationally expensive model to unravel of the theta mechanism it produces.

1.3.2 Gamma rhythms

Fast oscillations in the range of low gamma (25-50Hz) and high gamma (150-250 Hz) are associated with sensory processing and memory formation [39]. Activity in the lower end of the frequency range (≈25-55 Hz) has been termed "low gamma" or "slow gamma" and is driven by CA3 [40]. A second type of gamma rhythm exhibits a higher range of frequencies (≈60-100 Hz) and is entrained by inputs from medial entorhinal cortex (MEC) [40]; this type of activity has been termed "fast gamma" in some studies [40] and "midfrequency gamma" in others [140]. It has been suggested that cross-frequency coupling of theta/gamma rhythms might play a functional role in neuronal computation, communication and learning [30].

Two main theoretical models of gamma rhythms are proposed to account for the mechanisms of gamma synchrony in the hippocampus and other brain regions [28, 58]. Gamma oscillations can theoretically be generated purely through networks of mutually connected inhibitory interneurons (interneuron network gamma (ING) model) or through networks of reciprocally connected excitatory PYR and inhibitory interneurons (PYR-interneuron network gamma oscillations, pyramidal interneuron network gamma (PING) model) [58, 172, 163, 7]. In the ING mechanism, gamma is generated by a network of recurrently connected inhibitory interneurons. This model postulates inhibitory interactions between interneurons can sustain gamma frequency synchronization via tonic depolarization of connected interneurons. This gamma is independent of phasic PYR cell firings, although the interneurons do require a depolarizing drive. The frequency and coherence of the gamma generated is dependent on the amount of recurrent connectivity

in the network, the excitatory drive to the interneurons, and the decay time constant of the IPSCs. Conversely, the PING mechanism requires the interaction between principal cells and inhibitory interneurons, but does not require recurrent connections among the interneurons. In this model, excitatory PYR cells provide feedforward excitation of interneurons, which then provide inhibitory feedback to the comparatively more numerous PYR cell population. PING networks require specific firing ratios between the PYR and the interneuron populations, and oscillations only occur when principal cells have high firing rates. Physiologically, gamma may be generated by a combination of mechanisms, including ING and PING.

Both ING and PING mechanisms have been proposed by mathematically abstract, single compartment models, and as such to this day they remain theoretical. How these mechanisms apply in biologically realistic scenarios is unclear. ING and PING mechanisms assume that gamma activities merely reflect the firing of neurons however, gamma rhythms are measured in LFP recordings which is a complex signal, and as such the generation of gamma LFPs might be multifactorial. In Chapter 5, we discuss the generation of slow gamma LFPs.

1.4 Theta-gamma coupling

Low-frequency theta rhythms are dynamically involved across distributed brain regions by sensory signals or cognitive tasks; at the same time, high-frequency gamma brain activities reflect local brain processing [31]. It has been shown that phase coupling reflects various cognitive processes in humans [30], monkeys [31], rats [72] and mice [177]. Theta/gamma PAC or "nested" oscillations is in fact one of the most studied phenomena of phase coherence [31], reflecting the interrelations between local micro-scale and system-level macro-scale neuronal networks [40].

In non-epileptogenic hippocampi of neurosurgical patients and in a healthy brain of rodents, the degree of theta–gamma PAC increases with learning [165]. In the hippocampus, gamma and theta oscillations normally show a marked PAC cross-frequency-coupling considered to be central to hippocampal functions [165]. Thus, during spatial learning, the strength of hippocampal theta–gamma coupling usually directly correlated with the increase in correct performance of a cognitive task.

For these reasons developing frameworks of PAC mechanisms is pivotal for the understanding of the cognitive functions they correlate with. So far, contributions to theta-gamma PAC in the hippocampus have been investigated from a pathway perspective [111, 105]. In this thesis we consider cell-type contributions to theta-gamma PAC.

1.5 LFPs

1.5.1 Background

Oscillatory LFPs are extracellularly recorded potentials with frequencies of up to ≈500 Hz. The LFP is a widely available signal in many recording configurations, ranging from single-electrode recordings to multi-electrode arrays. It is recorded in the extracellular space in brain tissue, typically using micro-electrodes (metal, silicon or glass micropipettes). LFPs differ from electroencephalogram (EEG)s, which are recorded at the surface of the scalp, with macro-electrodes. It also differs from the electrocorticogram (EcoG), which are recorded from the surface of the brain using large subdural electrodes, while LFPs are recorded in depth, from within the cortical tissue (or other deep brain structures). A comprehensive overview of our present understanding of the mechanisms that underlie the generation of extracellular currents and fields is described in [27].

LFPs are associated with a number of cognitive processes and physiological functions in health and disease and complement the information obtained by analysis of spikes. Noticeably, studies analyzing sensory cortical processing [11] often rely on a combination of different types of electrophysiological signals, including LFPs. The role of LFPs has also been emphasized in spatial position encoding [100, 98] and memory processes [51] which includes the study of LFP theta rhythms [26]. Despite their indisputable importance, the generation mechanisms describing these activities remain largely unknown. In *in vivo* recordings the LFPs occur typically due to subthreshold activity as well as dendritic processing of synaptic inputs. LFPs are a less local measure of neural activity than network spiking as the LFP measured at any particular point will typically have sizable contributions from neurons located several hundred micrometers away and thus their interpretation is more complex.

Computational neuroscience has largely focused on how neurons and neural networks may process information, while less attention has been given to the relationship between the neural activity and measurable quantities. Fortunately, a precise biophysical modeling scheme linking activity at the cellular level and the recorded signal has been established. The biophysical origin of LFPs is well understood in the framework of volume conductor theory [132] in which extracellular electrical potentials are generated by transmembrane currents passing through cellular membranes in the vicinity of the electrode (-see Eq. 2.16 in Methods). The simulation of LFPs in combination with spiking models allows us to obtain a more holistic representation of the electrical activity and gives us the opportunity to effectively address a variety of questions associated with cognition

and perception in health and disease.

1.5.2 The necessity for biophysically realistic LFP models

In terms of modelling of LFPs several proxies have been used over the years. These include pooled spike trains [23], average membrane potentials in neuronal populations [10] and sums of synaptic input currents onto pyramidal neurons [52, 177]. However, none of these proxies can be expected to be generally valid for representing LFPs and thus understanding their emergence. One reason is that the vertical extent of the contributions from each cellular population to the LFP is similar to the vertical extent of the dendrites, and hence the net LFP at each location is a sum of positive and negative contributions from several overlapping neuronal populations that partially cancel each other out. This cancellation effect and the effect of intrinsic dendritic filtering [100, 98] can only be captured with spatially extended multi-compartment models.

Chapter 2

General Methods

2.1 Modelling of neurons and neural networks

2.1.1 Fundamentals

A neural network may be defined as a large, highly interconnected assembly of model neurons which are computing elements with a specified input-output relation. Each neuron in the network receives inputs from and provides output to a large number of other neurons. The connectivity of the network is specified by a synaptic interaction matrix. Neural network models are classified as *abstract models*, *intermediate models* and *biological models* depending on the biological detail they encompass [44]. In *abstract* models, all microscopic details about the working of the individual neurons are left out. The state of a neuron in these models is described by a single variable v which may be interpreted as the firing rate (the rate at which the action potential is generated). The pattern of synaptic connections and the values of the elements of the synaptic matrix (amount of success in find near-optimal solutions of used in models of this kind) bear little resemblance to biology. As these models mostly capture the dynamic output of a given network without much biological realism in their internal structure, they are also called *phenomenological*. In the models belonging to the *intermediate* category, each neuron is still treated as a simple input-output device with no internal structure. However, a number of experimentally observed features are incorporated in these architecture and synaptic connectivity pattern of the network. The main advantage of studying models of this kind lies in the fact that due to the relative simplicity analytic treatments are possible and numerical simulations can be carried out rather than easily. Last, in *biological* models, all known biophysical details of the individual neurons and synaptic connections among them are incorporated in the model. Due to their extreme complexity, models

of this kind are not amenable to analytic treatments. Numerical simulations provide the only way of studying their properties. Such simulations require extreme amounts of computing resources.

2.1.2 Conductance based models

The majority of this section has been adapted from [148].

Conductance-based models are the simplest possible biophysical representation of a neuron in which its protein molecule ion channels are represented by conductances and its lipid bilayer by a capacitor. These are models that contain enough biological detail to be classified as *intermediate* or *biological* according to the classification of the previous section.

Conductance-based models are based on an equivalent circuit representation of a cell membrane as first put forth by Hodgkin and Huxley [76]. These models represent a minimal biophysical interpretation for an excitable cell in which current flow across the membrane is due to charging of the membrane capacitance, I_C , and movement of ions across ion channels. In its simplest version, a conductance-based model represents a neuron by a single isopotential electrical compartment, neglects ion movements between subcellular compartments, and represents only ion movements between the inside and outside of the cell. Ion channels are selective for particular ionic species, such as sodium (Na) or potassium (K), giving rise to currents I_{Na} or I_K , respectively. Thus, the total membrane current, $I_m(t)$, is the sum of the capacitive current and the ionic current,

$$I_m(t) = I_C + I_{ionic} \tag{2.1}$$

where

$$I_C = C_m \frac{dV(t)}{dt} \tag{2.2}$$

In the Hodgkin-Huxley model, the original conductance-based model,

$$I_{ionic} = I_{Na} + I_K + I_L \tag{2.3}$$

The leak current, I_L , approximates the passive properties of the cell. Each ionic current is associated with a conductance (inverse of resistance) and a driving force which is due to the different concentrations of ions in the intracellular and extracellular media of the cell.

$$I_{ionic} = g_{Na}(V)[V(t) - V_{Na}] + g_K(V)[V(t) - V_K] + g_L[V(t) - V_L] \tag{2.4}$$

The voltage dependence or non-constant nature of the conductance, g (1/resistance) of ion channels is captured using "activation" and "inactivation" gating variables which are described using first-order kinetics. A current due to ionic species S with an activation gating variable, a , but no inactivation variable would be given by $g_S = g_S$ x a, where a is described by first-order kinetics and g_S represents the maximal conductance for the particular ion channel.

From the theoretical basis described above, the standard formulation for a conductance-based model is given as:

$$C_m \frac{dV}{dt} = \sum_j g_j(V_j - V) + I_{ext} \tag{2.5}$$

where:

$$g_j = g_j a_x^j b_y^j \tag{2.6}$$

$$\frac{da}{dt} = \frac{a_\infty(V) - a}{\tau_a(V)} \tag{2.7}$$

$$\frac{db}{dt} = \frac{b_\infty(V) - b}{\tau_b(V)} \tag{2.8}$$

for each j. V_j is the Nernst potential or reversal potential for current j, $(V - V_j)$ is called the driving force for j, and I_{ext} is an external current. a,b are gating variables raised to small integer powers x,y , respectively. a_∞, b_∞ are the steady-state gating variable functions that are typically sigmoidal in shape. τ is the time constant, which

can be voltage-dependent. Thus, conductance-based models consist of a set of ordinary differential equations (ODEs), as derived from current flow in a circuit representation following Kirchoff's laws. The number of differential equations in the set of model equations depends on the number of different ion channel types being represented with their particular activation and inactivation gating variables. The conductances can depend not only on transmembrane potential V, but also on concentrations of different ions.

These are some general formulations which very in their parameters according to the specific conductance that is represented in a given model. In Chapters 3, 4 and 5, we use the biologically realistic model of Bezaire and colleagues [13] as foundation, and the conductance equations of the ion channels included in the model can be found in this Appendix of the study [13].

2.1.3 Single and multi-compartment models

Conductance based models are classified as single and multi-compartment models according to their morphological detail. In the case of the single compartment conductance based models the morphological complexity of the cell is reduced in one (somatic) compartment. In multi-compartment cell models the dendritic complexity of the cell is taken into consideration and the dendrites are explicitly modelled.

The majority of this section has been adapted from [72].

2.1.4 Biophysical modelling of dendritic neurons

Around 1889, the "neuron doctrine" started to take form, driven by the leading anatomist the Spaniard Santiago Ramón y Cajal, who assumed that dendrites serve as the input region for other neurons and that the signal then flows from dendrites to the soma and axon —"the theory of dynamic polarization" [65]. However, it was only in the late 1960s that the biophysical nature of dendrites and their role in signal processing became the focus of direct experimental research, following Wilfrid Rall's groundbreaking theoretical framework for modeling electrical current flow in dendritic trees [132]. During the 1960s, cable models (a cylinder of finite length, and a ten-compartment model) were used to predict experimental results of the olfactory bulb. His linear cable theory for branching dendrites handled analytically the case of the passive dendrites [133, 132, 135] and his compartmental modeling method could treat the case of nonlinear (excitable) dendrites [132] numerically. This research established the significance of synaptic input to distal dendritic locations; it also explored properties of dendritic spines, and predicted dendro-dendritic synapses in the olfactory bulb. Since then Rall's theory has been in-

tensely employed and extended in order to explore the biophysical principles that link together the structure, physiology and function of dendrites. This theoretical foundation for modeling dendrites [132] has guided experimental studies for the last 50 years and has dramatically advanced our understanding of signal processing in dendrites [72].

2.1.5 Rall's biophysical framework

Until recently, most of the stable electrical recordings from neurons were made from the relatively large soma. However, most of the membrane area of central neurons is in their dendrites and it is there where synaptic input contacts the neuron. Can one learn about what happens locally at synaptic sites in the dendrites from recordings made at the soma? This question motivated Rall to formulate his cable theory for dendrites [133], followed by his compartmental modeling approach [134]. These groundbreaking studies have provided the theoretical framework for understanding how electrical current (both passive and active) flows in complicated dendritic trees.

Briefly, the one-dimensional cable theory for dendrites decomposes the dendritic tree into a set of interconnected cylindrical cables, each representing a small section of the dendritic tree. At any point along this cable the axial current (which flows along the axial resistance, r_i) may continue to either flow longitudinally or to flow into the membrane (either charging the membrane capacitance, c_m or crossing the membrane resistance, r_m). As a first approximation, Rall assumed that the dendrites are passive. Namely, that all the electrical parameters are constant (i.e., independent of time and voltage). The flow of current in a passive cable can then be described mathematically by the one-dimensional passive cable equation:

$$\frac{r_m}{r_i}\frac{\partial^2 V(x,t)}{\partial x^2} - r_m c_m \frac{\partial V(x,t)}{\partial t} - V(x,t) = 0 \tag{2.9}$$

where V is the transmembrane potential, and r_i (in Ω/cm), r_m (in Ω cm), and c_m (in F/cm) are all per unit length. The general solution for this equation can be expressed as an infinite sum of decaying exponentials [135]:

$$V(x,t) = \sum_{i=1}^{\infty} C_i \exp\{-t/\tau_i\} \tag{2.10}$$

where, for a given tree, the coefficients C_i are independent of time, t but they do depend on the point of observation, x and on the input current (the initial conditions). In contrast, for a given passive tree, the values for the ("equalizing") time constants, τ_i, are independent of input location or input current [135]. Rall showed that, for any passive tree, there is an analytic solution for the cable equation (namely, Ci and τ_i can be written explicitly). Thus, it became possible to combine the anatomical and physiological knowledge about a given dendritic tree and (assuming the tree is passive) to analytically describe how the input current flows from any input site to any other dendritic location, and specifically the soma [134]. Important insights were obtained when these analytic solutions were applied to both synthetic and to real dendritic trees. However, when a strong synaptic input (a transient conductance change, rather than a current input) or significant nonlinearities exist in the dendritic tree, such as voltage-dependent membrane conductance numerical (compartmental) methods for solving the corresponding (nonlinear) cable equation should be employed [134, 142].

In the compartmental approach, the continuous cable equation is discretized into a finite set of compartments, each representing a small section of the dendritic tree. The membrane properties of this dendritic section are grouped into a single RC element (where the membrane resistance, r_m, may depend on time and/or voltage, whereas c_m, the membrane capacitance, is typically assumed to be constant). The resistivity of the dendritic cytoplasm is lumped into a single (typically passive) axial resistivity, r_i. Thus, in an unbranched neuron, the current flowing in compartment j is:

$$\frac{d_j}{4r_{i,j}}\frac{V_{j+1}-2V_j+V_{j+1}}{\Delta x^2}-c_{m,j}\frac{dV_j}{dt}-i_{ion,j}=0 \tag{2.11}$$

where d_j, r_i,j, and c_m,j are respectively the compartment's diameter, axial resistivity, and membrane capacitance; i_{ion}, j includes all currents flowing through ionic channel conductances within the compartment, and Δx is the length of the compartment.

These two complementary approaches, the cable and compartmental models, have been utilized very successfully and have become even more popular due to their implementations in user-friendly software packages, such as NEURON [33] and GENESIS [20]. In this thesis we use the NEURON [33] simulator which implements the numerical solution of the cable equation of the multi-compartment, dendritic models.

2.2 Theoretical framework of LFPs

2.2.1 The general biophysical forward-modeling formula

The extracellular potentials are generated by transmembrane currents, and in the commonly used volume conductor theory the system can be envisioned as a three-dimensional smooth extracellular continuum with the transmembrane currents represented as volume current sources. In this theoretical framework the fundamental relationship describing the extracellular potential (ϕ) at position r due to a transmembrane current $I_0(t)$ at position r_0 is given by:

$$\phi(r,t) = \frac{1}{4\pi\sigma}\frac{I_o(t)}{|r - r_o|} \tag{2.12}$$

Here the extracellular potential is set to be zero in infinitely far away from the transmembrane current, and σ is the extracellular conductivity, assumed to be real, scalar (the same in all directions) and homogeneous (the same at all positions). The validity of Eq. 2.12 relies on several assumptions:

A. *Quasistatic approximation of Maxwell's equations*: This amounts to neglecting the terms with the time derivatives of the electric field E and the magnetic field B from the original Maxwell's equation, i.e.,

$$\bigtriangledown xE = -\frac{\partial B}{\partial t} \approx 0 \tag{2.13}$$

so that the electric (Eq. 2.13) and magnetic (Eq. 2.14) field equations effectively decouple. With $\bigtriangledown xE = 0$ it follows that the electric field E in the extracellular medium is related to an extracellular potential via:

$$E = -\bigtriangledown \phi \tag{2.14}$$

For the frequencies inherent in neural activity, i.e., less than a few thousand hertz, the quasistatic approximation seems to be well justified.

B. *Linear extracellular medium*: Linear relationship between the current density j and the electrical field E,

$$j = \sigma E \tag{2.15}$$

This constitutive relation is quite general, and σ in Eq. 2.15 may in principle be (i) a tensor, accounting for different conductivities in different directions, (ii) complex, accounting also for capacitive effects, and/or (iii) position-dependent, that is, vary with spatial position. (Note that Eq. 2.15 is valid only in the frequency domain. In the time domain j is generally given as a temporal convolution of σ and E.)

C. *Ohmic (resistive) medium*: Imaginary part of the conductivity σ is assumed to be zero, that is, the capacitive effects of the neural tissue is assumed to be negligible compared to resistive effects. This appears to be well fulfilled for the relevant frequencies in extracellular recordings.

D. *Isotropic (scalar) extracellular conductivity*: Conductivity σ is assumed to be the same in all directions, i.e., $\sigma_x = \sigma_y = \sigma_z = \sigma$. Recent cortical measurements indeed found the conductivities to be comparable across different directions in cortical grey matter; in white matter, however, the conductivity was found to be anisotropic.

E. *Frequency-independent extracellular conductivity*: Conductivity σ is assumed to be the same for all relevant frequencies, i.e., $\sigma(\omega)$ is constant. The validity of this assumption is still debated: while some studies have measured negligible frequency dependence, other investigations have suggested otherwise.

F. *Homogeneous extracellular conductivity*: Extracellular medium is assumed to have the same conductivity everywhere. This appears to be roughly fulfilled within cortical gray matter and frog and toad cerebella, but maybe not in the hippocampus. Frequency filtering properties and modeling of LFPs in inhomogeneous extracellular spaces have been considered [29, 117] however, in this thesis we consider the hippocampus extracellular space to be fairly homogeneous and isotropic [50] and these properties are not taken into consideration.

Eq. 2.12 applies to the situation with a single transmembrane current I_0, but since contributions from several transmembrane current sources add linearly, the equation straightforwardly generalizes to a situation with many transmembrane current sources. With N current point sources the formula in Eq. 2.12 generalizes to:

$$\phi(r,t) = \frac{1}{4\pi\sigma}\sum_{n=1}^{N}\frac{I_n(t)}{|r-r_n|} \tag{2.16}$$

It is clear that the measured extracellular potential will not only depend on the position of the electrode, but also the distribution of transmembrane currents. Fig. 2.1 further illustrates an important 'conservation' law when calculating extracellular potentials due to neural activity. This is Kirchhoff's current law: $\sum I_n(t) = 0$.

2.2.2 Numerical forward-modeling scheme

The numerical evaluation of extracellular potentials naturally splits into two stages:

1. Calculation of transmembrane currents for all neuronal membrane segments using multicompartment neuron models, typically using neural simulation tools such as NEURON [33].

2. Calculation of the extracellular potential on the basis of the modeled transmembrane currents and their spatial position using a forward modeling formula similar to Eq. 2.16. When a neuron is split into N compartments, the formula in Eq. 2.16 should correspond to a characteristic 'mean' position for compartment n, e.g., the center of a spherical soma compartment or the midpoint of a cylindrical dendritic compartment. This scheme corresponds to the so called point-source approximation since all transmembrane currents into the extracellular medium from a particular compartment are assumed to go through a single point.

2.3 Computational resources and tools

The single cell and network modelling in this thesis were implemented in NEURON [33]. The LFPs in Chapter 6, were implemented using LFPy [99], a Python package that implement the forward LFP formula of Eq. 2.16. In Chapters 3, 4 and 5 LFPs were explicitly coded in the CA1 microcircuit which we downloaded from: `https://senselab.med.yale.edu/ModelDB/showModel.cshtml?model=187604#tabs-1`. Analysis of results was done by custom MATLAB [112] and Python [169] scripts. Simulations were carried out on local machines and on Scinet [102] on the Niagara cluster, a large cluster of 2,024 Lenovo SD530 servers each with 40 Intel "Skylake" at 2.4 GHz or 40 Intel "CascadeLake" cores at 2.5 GHz.

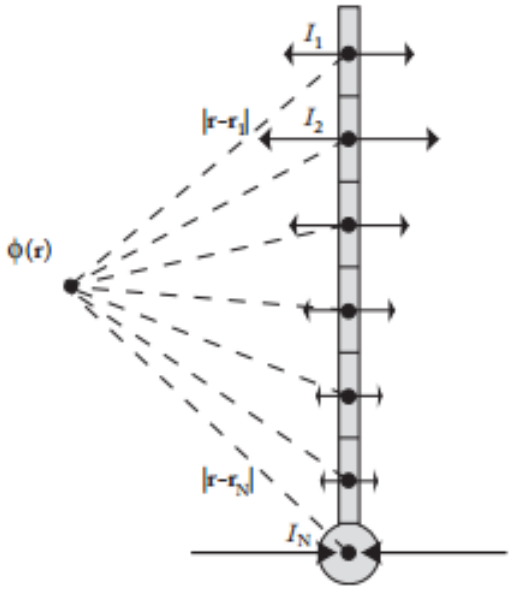

Figure 2.1: The LFP is produced by transmembrane currents passing across the cell membrane. Illustration of mathematical formula Eq. 2.16 providing the extracellular potential from transmembrane currents in a single neuron. The size and direction of the arrows illustrate the amplitudes and directions of the transmembrane currents. The law implies that the net transmembrane current (including the capacitive current) coming out of a neuron at all times must equal zero. Thus with the neuron depicted this Figure divided into N compartments, one must at all times have $\sum I_n(t) = 0$. Therefore a one-compartment model cannot generate any extracellular potential since the net transmembrane current necessarily will be zero. The simplest model producing an extracellular potential is a two-compartment model where transmembrane current entering the neuron at one compartment leaves at the other compartment. The simplest possible multipole configuration is thus the current dipole.

Chapter 3

Linking Minimal and Detailed Models of CA1 Microcircuits Reveals How Theta Rhythms Emerge and How Their Frequencies Are Controlled

Conceptualization and project design of the work presented in this Chapter was done by me and Dr. Skinner. Simulations and analysis of the results were done by me. The analysis presented in Chapter 3.4.1 was carried out by Melisa Gumus, an undergraduate student at the time, co-supervised by Dr. Skinner and me. To support Melisa's Network Clamp simulations of Chapter 3.4.1, I repaired the software *Network Clamp* of the Tool *SimTracker* [13]. This was done with guidance from one of the software developers, Dr. Ivan Raikov at Stanford University. The work presented in this Chapter is available as a biorxiv at:

Chatzikalymniou, Alexandra P., Melisa Gumus, Anton R. Lunyov, Scott Rich, Jeremie Lefebvre, and Frances K. Skinner. "Linking Minimal and Detailed Models of CA1 Microcircuits Reveals How Theta Rhythms Emerge and How Their Frequencies Are Controlled." BioRxiv, July 29, 2020, 2020.07.28.225557. https://doi.org/10.1101/2020.07.28.225557.

3.1 Preamble

The level of biological realism characterizing neuronal models is a spectrum, with phenomenological models (or abstract models as presented in the Background) on the one end and biophysical models on the other. Phenomenological models are typically described by a set of mathematical equations that reproduce the dynamic behavior of a neuron without containing explicit representations of the underlying biological intricacies. On the other hand, biophysical models contain realistic representations of biological cellular aspects. Phenomenological and biophysical models serve different, but complementary goals.

As biologically detailed models encompass many of the biophysical components that could contribute to a phenomenon of interest, the dynamic output they produce can be regarded as more realistic compared to that of abstract models. However, the advancement of biologically realistic models poses a challenge on our ability to analyze them using theoretical tools, a challenge that stems from the high-dimensional and multi-parametric nature of these systems. We propose that this problem can be addressed in part by leveraging insights from mathematically abstract models in application to those that are biologically detailed. In principle, such insights need to be verified experimentally. However, biophysically realistic computational models can act as an intermediate between abstract mathematical models and experiment, serving as a test-bed for theory examination. With this approach biologically detailed models can be better understood and theoretical predictions may be strengthened or questioned further. By no means can a theory be verified merely against biologically elaborate models, as theory verification can only occur against experimental data. However, testing a theory against complex models can primarily help us understand complex model mechanisms and facilitate the deduction of further predictions.

In this Chapter, we consider two models, an abstract (*minimal*) and a biologically detailed model, that both generate theta rhythms intrinsic to the hippocampus. We test insights of the minimal model in application to the biological model to understand how theta activities arise in the latter.

3.2 Introduction

Exactly how theta rhythms emerge is a complicated and multi-layered problem. It is now well-documented that theta rhythms can be generated intra-hippocampally, and emerge spontaneously from an isolated whole hippocampus preparation *in vitro* [67]. As

mentioned in the Background, two computational modelling studies have captured these intrinsic theta rhythms. The first study by Ferguson and colleagues [53], used minimal network models of biophysically simplified neurons, while the second study by Bezaire and colleagues [14], used biophysically detailed network models. These models can help us understand how these rhythms are generated while taking into consideration each model's advantages and challenges.

The biophysically minimal model [53] represents a 'piece' of the CA1 region of the hippocampus, and it was developed and constrained against data from the whole hippocampus preparation [56, 54]. We used this model to examine what 'building block' features could underlie theta rhythms [52, 53]. It was found that spike frequency adaptation (SFA) and post-inhibitory rebound (PIR) building block features of excitatory PYR cells in large minimally connected recurrent networks with fast-firing PV+ inhibitory cells could produce theta frequency population rhythms. Fitting the model to experimental observations of EPSC and IPSC amplitude ratios yielded the prediction that the connection probability from PV+ to PYR cells is larger than from PYR to PV+ cells. The minimal model design, strategy and setup suggests that the theta oscillation generation mechanism could be due to SFA and PIR building block features. However, the challenge is to determine how these insights could apply in the biological, hippocampal system with its larger complement of diverse inhibitory cell types and additional biological details.

The detailed model [14], is a full-scale biological model of the CA1 hippocampus with 338,740 cells that includes PYR cells, PV+BCs, AACs, BiCs, CCK+BCs and SCA cells. The model provides a realistic representation of the hippocampus which is grounded upon a previously compiled, extensive quantitative analysis [15]. It describes the activities of the PYR cells and the eight inhibitory cell types during theta rhythms. In broad terms, this model distinguishes the importance of certain cell types against others, and predicts that cell type variability is necessary for theta rhythms to occur.

To understand the theta generation mechanism in the biophysical model, we follow the strategy schematized in Fig. 3.1, according to three main steps. Results from **Step 1** are only summarized in this thesis while **Step 2** and **Step 3** are presented in detail. In [34] we first extended the minimal model, **Step 1**, to test the robustness of the theta rhythms in the face of PYR cell heterogeneity. We developed heterogeneous PYR cell networks and we examined the sensitivity of theta rhythms to the building block features of SFA, Rheo (the neuron's rheobase) and PIR. As a result, we established that theta frequency population bursts are particularly sensitive to PIR and Rheo feature values, and less sensitive to SFA values. Moreover phase response curve (PRC) examinations showed that the PV+ cell population creates a strong inhibitory 'bolus' that tunes and regularizes

the PYR cells and their firing frequency. We proposed from this observation, that the net input (recurrent excitation, excitatory drive and incoming inhibition) received by the PYR cell situates it in a frequency range that allows theta frequency population bursts to occur. However, just from these minimal model examinations, it was unclear whether such a relationship between PYR cell inputs and network frequency would exist in biologically realistic networks.

Moving on to **step 2** we compared minimal and detailed models, to identify commonalities and differences in their structure that could underlie similar or different theta generation mechanisms. Finally, in **step 3**, we extracted a 'piece' of the detailed model, the segment model, which is comparable in cell numbers to the minimal model, and we investigated the effect of the noted differences from **step 2** on the theta output. Following a principled exploration of the segment model, we tested hypothesis proposed by the minimal model in application to the segment model and we deciphered how the theta rhythm is produced.

3.3 Methods

3.3.1 The segment and detailed model explorations

The segment model is simply a 10% piece of the detailed model of the rodent CA1 microcircuit [14] as illustrated in Fig. 3.1 and Fig. 3.3A. To create and use the segment model, one must first be able to access and use the detailed model.

In segment and detailed models, there are eight different inhibitory cell types and excitatory PYR cells. All of these cell types are connected in empirically specific ways based on an extensive knowledge-based review of the literature [15]. The cells are evenly distributed within the various layers of the CA1 (SLM, SR, SP, SO) in a three-dimensional prism. Afferent inputs from CA3 and EC are also included in the form of Poisson-distributed spiking units from artificial CA3 and EC cells. We note that although there are layer-dependent specifics regarding how the different cell types are arranged in the full-scale detailed model (Fig. 3.1), there are not any differences along the longitudinal axis of the full-scale model. As such, the connection profile at any location along the longitudinal axis does not vary. In other words, the connection probabilities in any particular part of the longitudinal axis would be the same assuming that there are enough cells for meaningful calculations.

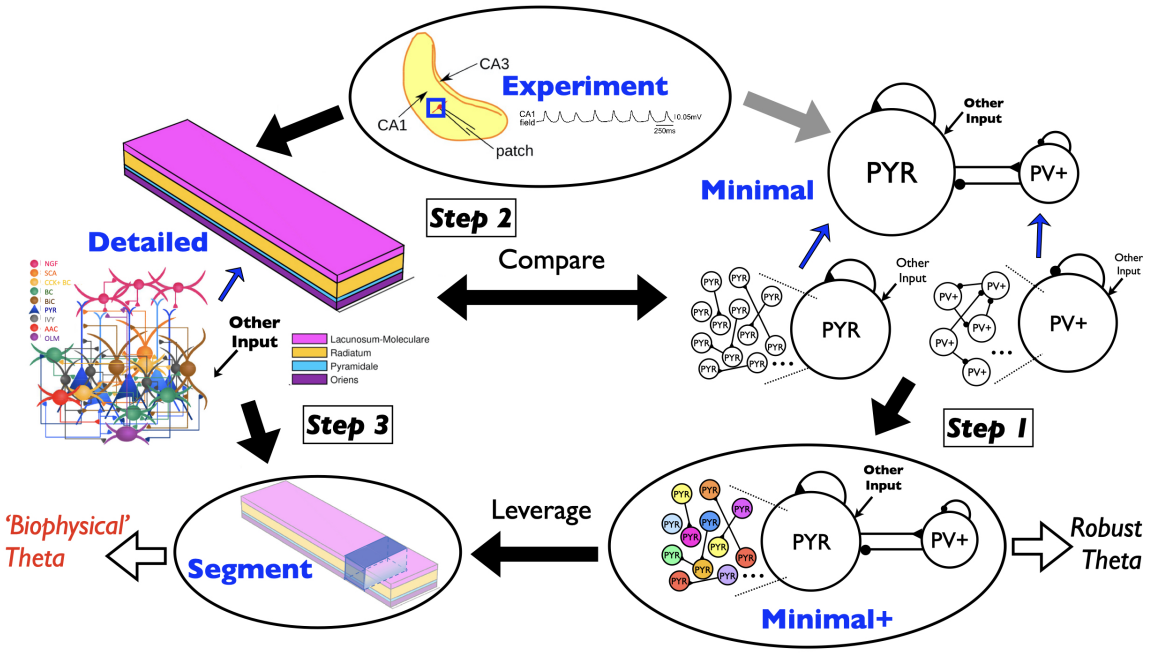

Figure 3.1: Schematic illustrating overall paper flow and strategy. The experimental context and four model types are referred to in the paper: *Experiment* - a whole hippocampus preparation that exhibits spontaneous theta rhythms [67]; *Minimal* - a previously published work of minimal network models representing a 'piece' of the whole hippocampus (blue square in *experiment* illustration) that generates theta rhythms within experimental constraints [53]; *Minimal+* - an expansion of the minimal model using heterogeneous PYR cells (as illustrated with differently coloured PYR cells) that is used in the present paper; *Detailed* - a previously published work of a full-scale detailed CA1 microcircuit model (eight different inhibitory cell types and PYR cells) that generates theta rhythms without any oscillatory input [14]; and *Segment* - a network model representing a 'piece' of the detailed model, that is used in the present paper. The three main steps in the flow of the paper are shown (**Steps 1-3**), and the foci of the work in the present paper are illustrated by the black arrows: The detailed model is examined in light of the experimental data; a systematic comparison between minimal and detailed models is done; the segment model is created from the detailed model; the minimal+ model is constructed based on the minimal model, and mechanistic insights resulting from the minimal+ model are leveraged in the segment model. The black open arrows illustrate that 'Robust Theta' in the minimal+ model is examined leading to hypothesis development, and leveraging this in the segment model helps with an understanding of 'Biophysical Theta' where multiple cell types can be considered. The grey arrow illustrates previously done work where the minimal model was developed and examined in light of the experimental data [53]. Illustrations include: *Minimal* model setup with PYR and fast-firing PV+ cells, *Detailed* model setup with 9 cell types (NGF, SCA, CCK+BC, BC, BiC, PYR, IVY, AAC, OLM) and layer-specific connectivity, *Experiment* of whole hippocampus preparation with a LFP theta example, heterogeneous PYR cells as different colors in *Minimal+* model, and a shaded portion of the *Detailed* model prism to illustrate the *Segment* model. This figure is adapted from: Figs. 1,8 of [79], Fig. 2 of [53], and Fig. 1 of [14]

.

Accessing the CA1 microcircuit model

The code that we use for this work starts from the original CA1 microcircuit repository which can be found at ModelDB at: `https://senselab.med.yale.edu/ModelDB/showModel.cshtml?model=187604`. The model version we used can be downloaded from: `https://bitbucket.org/mbezaire/ca1/pull-requests/3/d1efeb957848/commits`. Analysis of simulation outputs can be recreated using the publicly available SimTracker tool [13] which can be downloaded from: `http://mariannebezaire.com/simtracker/`. It is recommended that users install SimTracker first and then install and register the CA1 model under SimTracker, to take advantage of the visualization functionalities of the SimTracker package. This tool is offered both as a stand-alone, compiled version for those without access to MATLAB [112] (for Windows, Mac OS X, and Linux operating systems), and as a collection of MATLAB scripts for those with MATLAB access. Once the SimTracker and the ca1 repository are installed, users can run simulations either on their local machines using a small scale of the CA1 network, or on supercomputers as needed for full scale network simulations. To reproduce the findings presented here, one needs to first familiarize oneself with the CA1 microcircuit background and code.

The segment model is created from the detailed model by setting the "Scale" parameter = 10, which reduces the number of cells and the volume of the CA1 prism by a tenth, and by dividing all connections in the network by a factor of 10. If this latter step is not done, then each cell would have ten times as many connections relative to a cell in the full-scale detailed network. That is, the parameter scaling is a 'normalization' in which the 'scaled' network assumes that each cell is a representative of '10 cells'. We did not want this, as the segment model is simply a piece of the detailed model and so we 'removed' the normalization by dividing the number of connections by ten.

Calculation of connection probabilities and synaptic weights in the detailed model

To be able to compare connectivities between minimal and detailed models, we compute connection probabilities in the detailed model. They are computed by dividing the total number of connections from a single presynaptic cell of a given type, to the cells of the postsynaptic population, divided by the total number of (postsynaptic) cells, of that particular population. They are thus computed as divergent connection probabilities, as it was done in the minimal model where random divergent connection probablities were employed. To compute connection probabilities when PV+ cells are assumed to consist of more than one inhibitory cell type, a combination is required. For example, in consid-

ering basket cell (BC)s and BiCs as fast-firing PV+ cells in one population, the number of connections each cell (either BC or BiC) receives is the average of presynaptic connections each receives, as given in the detailed model. For example, the number of connections from PYR cells onto BC/BiC population equals the total number of presynaptic connections that BCs and BiCs receive from PYR cells. The connection probability from PYR to PV+ cells (BC/BiC combination) is calculated by dividing this total number of connections by the total number of BCs and BiCs. All numbers and connection probabilities are shown in Table 3.2.

The synaptic weight in the detailed model is given by the synaptic conductance multiplied by the number of synapses per connection. So, for example, as a single BC cell has 11 synapses/connection onto a PYR cell and a synaptic conductance of 0.2 nS, then the synaptic weight is 2.2 nS. In the case of combined cell type populations, the average synaptic weight for the given cell type with its number of synapses/connection and synaptic conductance as reported by [14]. All of the computed synaptic weights are shown in Table 3.2.

Calculation of EPSC/IPSC amplitude ratios in the detailed model

For comparison with experimental data, we examine what EPSC/IPSC amplitude ratios exist for cells in the detailed model. We choose 15 cells of each type from the full-scale model [14]. These types are PYR cells and fast-firing PV+ cell types - BCs, BiCs and AACs. In doing this examination it is important to note that experimental estimates of these ratios as derived from voltage clamp recordings are not precise as there are associated experimental limitations such as due to space clamp. However, the experimental data shows that EPSCs received by PV+ cells are much larger in amplitude than EPSCs received by PYR cells, and since IPSCs received by PV+ and PYR cells are similar in amplitude, the experimental limitations are moot as it is clearly the case that the EPSC/IPSC amplitude ratios for PYR cells are much less than for PV+ cells [79].

In considering the detailed model, several aspects need to be taken into consideration. First, in the detailed model, we consider fast-firing PV+ cell types as BCs, BiCs or AACs in different combinations. Next, with the detailed model, morphological representations of cells are used and there are eight different inhibitory cell types. These different inhibitory cell types synapse onto different parts of the PYR cell tree and as such, IPSCs onto PYR cells would be attenuated by different amounts when examining synaptic currents at their somata. We note that to directly compare synaptic currents from the experiments with the detailed model, one could consider performing a voltage clamp on model cells and separately examining EPSCs and IPSCs as done experimen-

tally, but one would additionally need to separate IPSCs that are due to the different inhibitory cell types to consider PV+ or PYR cells. Undertaking this in the detailed model would be a highly non-trivial endeavour, and indeed, decades of research has uncovered the richness and complexities of dendritic integration [155]. Thus, since we know that the EPSC/IPSC amplitude ratios are very different on PYR and PV+ cells, we focus on EPSCs and IPSCs on either PYR or PV+ cells at somatic locations without trying to compensate for voltage clamp or attenuation issues due to different synaptic input locations from the different cell types. From the consideration that the comparison is with experiment, we consider that EPSCs onto the different cell types are due to inputs from PYR cells and EC and CA3, whereas IPSCs are from the various inhibitory cell types of the detailed network model [14]. As we are mainly considering comparisons with the minimal model, we consider IPSCs that are due to PV+ fast-firing cell type could encompass BCs, BiCs and AACs.

The network clamp tool in SimTracker enables extraction of a particular cell from the full-scale model while keeping synaptic properties [13]. We network clamp each of the 15 selected cells of each type for 1000 msec and detect the peak EPSCs and IPSCs by implementing the minimum peak distance algorithm in MATLAB. For EPSC/IPSC amplitude ratio calculations for a specific cell, all excitatory currents are summed and divided by the summed inhibitory currents that the cell receives. For EPSC/IPSC amplitude ratios on to PYR cells, IPSCs due to only BCs, only BiCs, a combination of BCs and BiCs, a combination of BCs/BiCs/AACs, and all inhibitory cells are shown in Table 3.1. We note that there is no EPSC/IPSC amplitude ratio consideration of AACs to themselves as there are no AAC to AAC synapses in the detailed model. When there is a combination, the ratio calculations are based on dividing the mean EPSCs by mean IPSCs, after summing IPSCs from each PV+ cell type. The EPSCs are flipped before peak detection for its mechanistic advantage using the MATLAB code. All 225 (15x15) combinations of EPSC/IPSC amplitude ratios in each BC/BiC/PYR and BC/AAC/PYR populations as well as 3375 (15x15x15) combinations in BC/BiC/AAC/PYR are examined, and they are in accordance with the experimental data. The mean EPSC/IPSC amplitude ratios and their standard deviations for the various cell types are given in Table 3.1. Voltage recordings and currents plots from the 15 chosen cells can be accessed at `https://osf.io/yrkfv/`. The scripts for the EPSC/IPSC amplitude ratio calculations can be found at `https://github.com/FKSkinnerLab/CA1_SimpleDetailed`.

Parametric explorations in the segment model

To generate the heatmaps of Fig. 3.4 we use the following process on the created segment model. We perform exhaustive parametric explorations of the theta power dependence on the excitatory drives in the segment model. We vary the EC/CA3 to PYR cell synaptic conductance $g_{ec/ca3-pyr}$, the PYR-PYR synaptic conductance $g_{pyr-pyr}$ and the level of external stimulation, which represents the firing rate of our external EC and CA3 cells. For every pair of $g_{pyr-pyr}$ and $g_{ec/ca3-pyr}$, we search for the level of external stimulation that maximizes the normalized theta power. The normalized theta power is defined as the maximum theta power (net theta power) in the power spectrum, divided by the mean power across all frequencies. We search a range of 0.15-0.65 Hz of stimulation per network (below that range the network is inactive, above that range the network is hyper-active). We plot the value of that maximum normalized theta power in Fig. 3.4Bi, and the corresponding stimulation required to reach that value in Fig. 3.4Biii. Every pair of $g_{pyr-pyr}$ and $g_{ec/ca3-pyr}$ corresponds to a specific conndata#.dat file. These conndata#.dat files should be created and stored under the "datasets" directory of the CA1 repository. The code for the generation of the heatmaps of Fig. 3.4B can be found here: `https://github.com/alexandrapierri/CA1-Segment-Microcircuit`

Current extractions and linear regression in the segment model

As described above for ratio calculations in the detailed model, we use the network clamp tool of SimTracker to extract PSCs delivered to the PYR cells in the model from all other cells in the network and the external drives. We examine the EPSCs and IPSCs received by 10 PYR cells for each of the 50 networks underpinning the heatmaps of Fig. 3.4B. We calculate the mean current amplitude for each of the 10 cells over a 4sec simulation period, and refer to this as the net current. We take the average and standard deviation of the net current of the 10 cells and plot it against the frequency of that network (Fig. 3.5C).

As we examine 10 cells per network and we have 50 networks, this gives as a total of 500 network clamp simulations which corresponds to analysis of 500 cells' input currents. To perform a linear regression of net current vs network frequency, we use custom MATLAB code which can be found here: `https://github.com/alexandrapierri/CA1-Segment-Microcircuit`. The correlation coefficient between theta frequency and net current (ρ) and the p-value for testing the hypothesis of no correlation (null hypothesis) against the alternative hypothesis of a nonzero correlation, are estimated using MATLAB's built-in functions.

Power analysis and signal filtering

To analyze the signal power we used the Welch's Periodogram, a method for estimating power spectra based on FFT analysis `https://ccrma.stanford.edu/~jos/sasp/Welch_s_Method.html`. To filter the raw LFP signal for theta (see for example Fig. 3.3Bii,iii) we used a broadband filter with stopband frequencies ± 1 Hz and passband frequencies $\pm$ 1.75 Hz from the peak theta frequency as derived from the Welch's Periodogram.

High performance computing simulations

We implement our simulations on Scinet [102, 130] on the Niagara clusters, using 10-12 nodes per simulation with 40 cores per node. Each network simulation takes approximately 8 hours real time to be executed. The results we present in this study are the distillation of approximately 300 network simulations requiring a total of 150 core years processing power on the clusters.

3.4 Results

The flow of the results section is as follows. To investigate the theta mechanism in the detailed model we first compare EPSC/IPSC amplitude ratios in the detailed model with those in the whole hippocampus preparation to examine if the detailed model can successfully reproduce available experimental observations. This was already done with the minimal model [34]. Next, we carry out a systematic comparison between minimal and detailed models by comparing connectivities, synaptic weights and external drives. We perform this comparison to unveil commonalities and differences in the network structure of the two models that could underlie similar or different theta mechanisms. Finally, we isolate a 'piece' of the detailed model - the segment model - comparable in cell numbers to the minimal model. We examine the segment model in a principled manner according to minimal and detailed model differences to further elucidate the implications of these differences on the theta rhythms produces by each model. We test predictions of the minimal model in application to the detailed. As the segment model is much smaller than the detailed model, we can perform extensive explorations and establish how intra-hippocampal theta rhythms are generated and how their frequencies are controlled.

3.4.1 Linkage explorations between minimal and detailed models generating intrinsic theta rhythms intra-hippocampally

To consider whether the detailed model uses similar theta-generating mechanisms as the minimal model, we examine commonalities and differences between the two models, as illustrated by 'compare' in Fig. 3.1. However, we first turn to an examination of EPSC/IPSC amplitude ratios in the detailed model relative to those observed in the whole hippocampus preparation.

EPSC/IPSC amplitude ratios in the detailed model are consistent with those in the whole hippocampus preparation

The detailed model is experimentally constrained in a bottom up fashion, using cellular data and connectivity information from a plethora of experimental data [15]. Whether the detailed model yields meso-level measurements, such as EPSC/IPSC amplitude ratios that agree with experimental observations from the whole hippocampus preparation, has not been directly assessed. Thus, we here examine whether the detailed model exhibits ratios that match those observed in experiments from the whole hippocampus preparation, as was already considered in the minimal model. From the experimental data it is abundantly clear that the EPSC/IPSC amplitude ratios for PYR cells are much less than for PV+ cells. For the detailed model, we consider PV+ cells to represent BCs, BiCs, or combinations of BCs, BiCs and AACs. We choose 15 cells of each type and extract EPSCs and IPSCs at the somata of the different cell types and compute the ratios. We find that regardless of the PV+ cell type or combination considered, it is always the case that the EPSC/IPSC amplitude ratios are consistent with experiment - larger on PV+ cells than on PYR cells - as shown in Table 3.1. Further details are provided in the Methods.

Minimal model connectivity prediction validated using detailed model empirical numbers

In the minimal model we predicted that to have EPSC/IPSC amplitude ratios that are consistent with the experimental observations, it is necessary for the connection probability from PV+ to PYR cells to be larger than from PYR to PV+ cells. The connectivities in the detailed model are based on empirical determinations [15]. Thus, if the minimal model is an appropriate representation of the CA1 microcircuitry, its connection probabilities should be in line with those in the detailed model. To consider this, we note two things. First, the minimal model only includes fast-firing PV+ and PYR

Table 3.1: EPSC/IPSC amplitude ratios from detailed model network cells.

PV+ cell type	**EPSC/IPSC amplitude ratio (on PYR cell)**
= BC	4.05 ± 0.86
= BiC	7.21 ± 1.19
= BC/BiC	2.95 ± 0.62
= BC/AAC/BiC	1.78 ± 0.39
= All inhibitory cell types	1.32 ± 0.24
	EPSC/IPSC amplitude ratio (on PV+ cell)
= BC	11.71 ± 2.66
= BiC	34.97 ± 5.28

cells, and second, it uses a random connectivity scheme. Thus, to make comparisons, we consider only PV+ cell types and PYR cells from the detailed model and determine connection probabilities between them using their empirically-based connection schemes. Three inhibitory interneuron cell types in the detailed model can be considered as fast-firing PV+ cell types. These are the BCs, the BiCs and the AACs. Considering only these three inhibitory cell types and the PYR cells, we extracted the number of their post-synaptic connections. This is shown in schematic form in Fig. 3.2. To compare connection probabilities between minimal and detailed models we considered that the fast-firing PV+ cell type in the minimal model could correspond to: (i) only BCs; (ii) only BCs and AACs; (iii) only BCs and BiCs; (iv) BCs, AACs and BiCs. BCs represent the majority of fast-firing PV+ cell types and so they are included in all of the different combinations.

The connection probabilities computed from the detailed model are given in Table 3.2 along with connection probabilities from the minimal model (details are given in the Methods). To avoid repetition, minimal model connection probabilities are only shown for the "PV+=BC" case in row #2 of Table 3.2. We found that regardless of the PV+ cell type consideration (i-iv), the connection probability from PV+ to PYR is greater than from PYR to PV+ in the detailed model, indicating that one of the predictions of the minimal model is in effect in the CA1 microcircuitry. Thus, this comparison yields a 'validation' of the minimal model as one of its main predictions is in effect in the detailed model which has empirically determined connection probabilities from many experimental determinations [15]. We consider this a validation because the connectivity profile of the detailed model is directly derived from experimentally identified connections

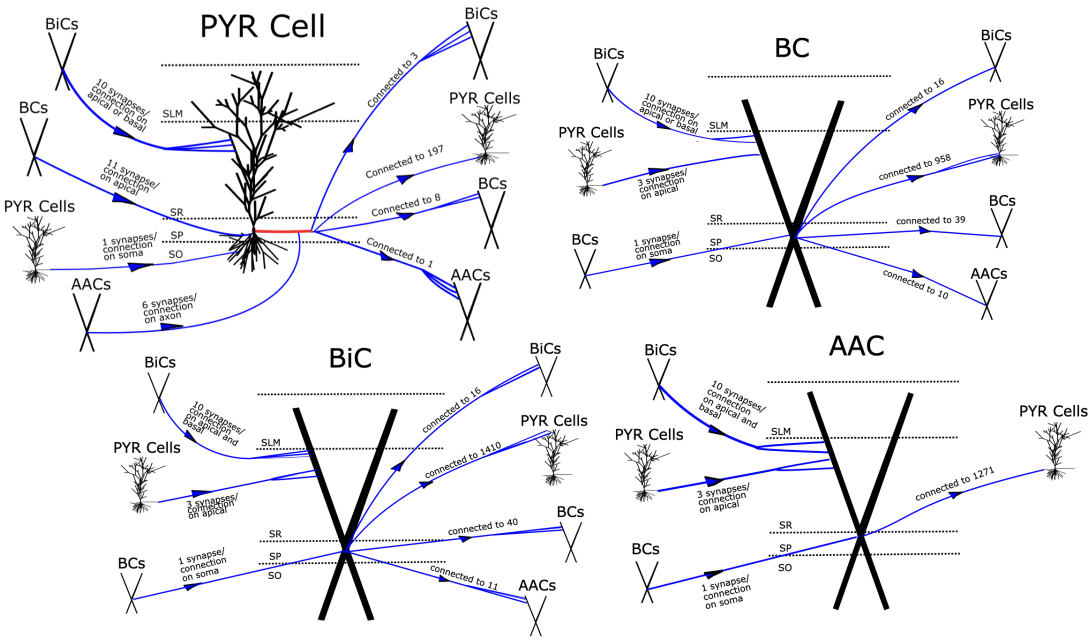

Figure 3.2: Schematics summarizing connections in the detailed model for PYR and PV+ cell types. The four schematics illustrate the connection schemes that exist in the detailed model, where we only consider PYR and PV+ cells (BCs, BiCs, AACs) [14]. For each large centered cell, the number of synapses per connection and its approximate location on the cell is specified for whichever cells are presynaptic, and the number of cells that the large centered cell connects to is also illustrated for whichever cells are postsynaptic. These numbers are also reflected in Fig. 3.2. The morphological structure along with its layer location from the detailed model is also shown. The red line in PYR cell denotes its axon.

between cell types and it is hence biologically realistic. We note that comparison of PYR to PYR and PV+ to PV+ connection probabilities between minimal and detailed models are expected to be appropriate as these connection probabilities in the minimal model were derived from the experimental literature [57, 55]. As noted in Table 3.2, the PYR to PYR connection probability (see row #1) is an order of magnitude less than it is for the PV+ to PV+ connection probability (see rows #2-#5) for both minimal and detailed models.

In making these comparisons, we do not expect to have an exact matching of connection probability values. Besides the fact that the minimal model consists of a subset of different inhibitory cell types in the detailed model, the cellular models differ in their compartmental and mathematical biophysical 'structure'. Specifically, the detailed model has multi-compartment models that include conductance-based ion current representations, and the minimal model has single compartment models with an Izhikevich mathemat-

Table 3.2: Detailed model connection probabilities and synaptic weights.

Row	**Cell Types and Connections**	**Number of cells**	**Number of connections**	**Connection Probability**	**Number of synapses per connection**	**Synaptic Weight*** $g(nS)$
#1	**PYR**	311,500				
	PYR to PYR		197	0.00063 [*0.01 for minimal model (MM)*]	1	70.0 [*0.094 for MM*]
#2	**PV+ = BC**	5,330				
	PYR to BC		8	0.0015 [*0.02 for MM*]	3	2.1 [*3.0 for MM*]
	BC to PYR		958	0.0031 [*0.3 for MM*]	11	2.2 [*8.7 for MM*]
	BC to BC		39	0.0071 [*0.12 for MM*]	1	1.6 [*3.0 for MM*]
#3	**PV+ = BC/AAC**	7,000				
	PYR to BC/AAC		9	0.0014	6	4.4
	BC/AAC to PYR		1,115	0.0036	8.5	5.7
	BC/AAC to BC/AAC		49	0.0070	1	0.8
#4	**PV+ = BC/BiC**	7,740				
	PYR to BC/BiC		11	0.0014	6	16.0
	BC/BiC to PYR		1,184	0.0038	10.5	3.7
	BC/BiC to BC/BiC		111	0.014	11	77.1
#5	**PV+ = BC/AAC/BiC**	9,210				
	PYR to BC/AAC/BiC		12	0.0013	9	23.8
	BC/AAC/BiC to PYR		1,213	0.0039	9	5.6
	BC/AAC/BiC to BC/AAC/BiC		132	0.014	11	54.0
#6	**Other Input**					
	CA3 to PYR	n/a	5,985	n/a	2	0.40
	EC to PYR	n/a	1,299	n/a	2	0.40
	CA3 to BC	n/a	6,047	n/a	2	0.44
	CA3 to AAC	n/a	4,170	n/a	2	0.24
	EC to AAC	n/a	485	n/a	2	0.24
	CA3 to BiC	n/a	5,782	n/a	2	0.30
	EC to BiC	n/a	432	n/a	2	0.30

* Synaptic Weight = Synaptic Conductance × number of synapses/connection

ical representation [83, 52]. It is however reassuring that the connection probabilities compare favourably as described above, since both minimal and detailed models produce intrinsic, intra-hippocampal theta rhythms.

E-I balance considerations in minimal and detailed models expose differences

So far we have shown that the connection probabilities in the minimal model are appropriate relative to the empirical ones in the detailed model and that the detailed model has appropriate EPSC/IPSC amplitude ratios from the perspective of the whole hippocampus preparation that generates intrinsic theta rhythms. Let us now exploit these linkages.

We first note that since both the minimal and full-scale detailed models produce theta rhythms, the underlying E-I balances that are present in both models must be appropriate for the generation of theta rhythms. Now, besides connection probabilities

between excitatory and inhibitory cells, synaptic weights and any other external drives to the network models would also affect E-I balances.

Synaptic Weights: Similar to the comparison consideration of connection probabilities above, we compare synaptic weights in minimal and detailed models. As before, we focus on a cellular subset of the detailed model the fast-firing PV+ cells. The number of connections and synaptic weights for PV+ and PYR cells are given in the last two columns of Table 3.2. Note that the synaptic weight refers to a connection between cells so that the number of synapses per connection is taken into consideration. From a comparison of these weights, it is clear that there is about three orders of magnitude difference between the synaptic weights of PYR to PYR cells whereas the synaptic weights from PV+ to PYR, PYR to PV+ and PV+ to PV+ are comparable (i.e., same order of magnitude), if PV+ cells are considered to be BCs or a combination of BCs and AACs (see Table 3.2). Thus, on the face of it, the detailed model has much stronger connections between PYR cells relative to the minimal model.

External Drives: The minimal model is driven by an external excitatory input, denoted as 'other input' in the schematic of Fig. 3.1, that is applied only to the PYR cells of the E-I networks. The amount of this other input is comparable or smaller than any of the 'internal' EPSCs (see Table 5 in [53]), as it has a zero mean with fluctuations of $\approx$ 10-30 pA. For the detailed model, the excitatory and inhibitory cells are driven by activation of excitatory afferents from the CA3 and the entorhinal cortex (EC) with connectivity of empirical estimation (see row #6 in Table 3.2). Unlike the minimal model, these CA3/EC excitatory inputs are larger relative to the 'internal' EPSCs and so likely play an important role in maintaining the appropriate E-I balance for theta generation in the detailed model. Specifically, the CA3, EC and PYR cell excitatory currents onto PYR cells are approximately 10, 6 and 10 nA. The detailed model is only loosely based on the whole hippocampus preparation. Its theta rhythms are produced intra-hippocampally but the network is driven by external EC and CA3 noisy afferents. These afferents conceptually represent remaining inputs from cut afferents after extraction from the whole brain. Given that the external drives in the minimal and detailed models are not represented in a similar way, we cannot compare them directly. However, it is possible that the large difference in PYR to PYR synaptic weights between minimal and detailed models is partly because of their external drive differences.

In summary, our consideration of linkages between minimal and detailed models via the whole hippocampus preparation (see Fig. 3.1) that generates intrinsic theta rhythms leads to the following: the minimal model has appropriate connection probabilities relative to the biological system, as represented by a biologically detailed full-scale CA1

microcircuit model; the full-scale detailed model has appropriate EPSC/IPSC amplitude ratios relative to experiment; and although both minimal and detailed models produce intra-hippocampal theta rhythms, there are notable differences between their PYR to PYR synaptic weights and external drives.

3.4.2 Using a 'piece' of the detailed model to understand the initiation of theta rhythms and how their frequencies are controlled

It is worth re-stating that despite its several limitations (e.g., only 70% of inhibitory cell types were included), the detailed model produces robust theta rhythms. However, because of its large size and computationally expensive nature, extensive parameter explorations were not performed. As a result, even though the detailed model produces theta rhythms, and model perturbations indicated that some cell types and not others are important for their emergence, we do not know how the rhythm generation is initiated or controlled. To address this, we first isolate a part of the detailed model, the segment model (see Fig. 3.3A), that has comparable cell numbers to the minimal model. We investigate the segment model according to the noted differences with the minimal model and examine how this is manifest in the power and frequency of LFP theta rhythms that we subsequently interpret in light of the minimal model mechanism. From this investigation, we unveil an understanding of how the 'biophysical' theta rhythms are generated and how their frequencies are controlled in a biologically detailed model with multiple inhibitory cell types.

Creating the segment model and examining its initial behaviour

We start by extracting a 'piece' of the detailed model which has a comparable number of cells relative to the minimal model, and we refer to it as the segment model - see Fig. 3.3Ai. Our segment model represents 10% of the original detailed model and it has all of the same cell types with the same layer location positioning and synaptic connection structure as the detailed model. That is, the segment model contains eight inhibitory cell types and is driven by excitatory afferents representing inputs from the EC and the CA3 region, as illustrated in Fig. 3.3Aii. The activation of the EC/CA3 synapses is modeled as an independent Poisson stochastic process and the strength of this activation is represented by the Poisson stimulation parameter. These afferents project to the majority of the cell types in the network with the exception of the OLM cells which are only driven by the PYR cells. Therefore, in contrast to the minimal

model, the segment model is driven by external inputs that in addition to the PYR cells, also project to the inhibitory cells of the network (see Fig. 3.1). Even though the segment model represents only 10% of the original detailed hippocampus model, its much smaller size makes it now possible to investigate the network dynamics by undertaking extensive parameter explorations using high-performance computing. We carried out this investigation by exploiting the noted differences between minimal and detailed models, and by considering the minimal model insights.

Let us start by examining the segment model without changing any of its parameters relative to the detailed model. As expected, the segment model does not produce any output. Instead, this 'fraction' of the detailed model produces hyperactive cell populations (not shown) indicating that the E-I input balances to the cells are shifted in favour of excitation. This suggests that to get a theta rhythm in the segment model, one could simply reduce the activation of the external afferents via the stimulation parameter. This is a reasonable consideration given that our model essentially consists of a smaller piece of tissue. We found that theta rhythms arise in the segment model when we decrease the stimulation parameter, but they have very low power and are very noisy. The raw LFP signal, as recorded in stratum pyramidale, is shown in Fig. 3.3Bi, and it can be seen to be quite noisy. Guided by the Welch's Periodogram, as shown in Fig. 3.3C, theta rhythms at two peak frequencies (3.7 and 9.2 Hz) can be discerned. The filtered LFP signal is shown above Fig. 3.3Bii and Fig. 3.3Biii. In essence, this finding predicts that a 10% piece of a whole hippocampus preparation is enough of a tissue volume to generate theta rhythms. This supports the viewpoint, supported by experimental observations, that the hippocampus is comprised of multiple theta oscillators along its septotemporal axis [67].

Designing an extensive parameter exploration of the segment model

As shown above, the segment model, without any changed parameter values besides the stimulation parameter, produces weak and noisy theta rhythms - see Fig. 3.3B. Is it possible to obtain robust theta rhythms in the segment model? That is, can we increase the power of the theta rhythms expressed by the segment model? To answer this, we were motivated to determine whether bringing the segment model to a similar E-I parametric regime as the minimal model could 'enhance' the theta rhythms. To test this, we examined whether by adjusting for differences between the models, we could increase the power of the theta rhythms expressed by the segment model.

From the comparison between the minimal and detailed models, we found that their two main differences stemmed from the external drives to the network and the synaptic

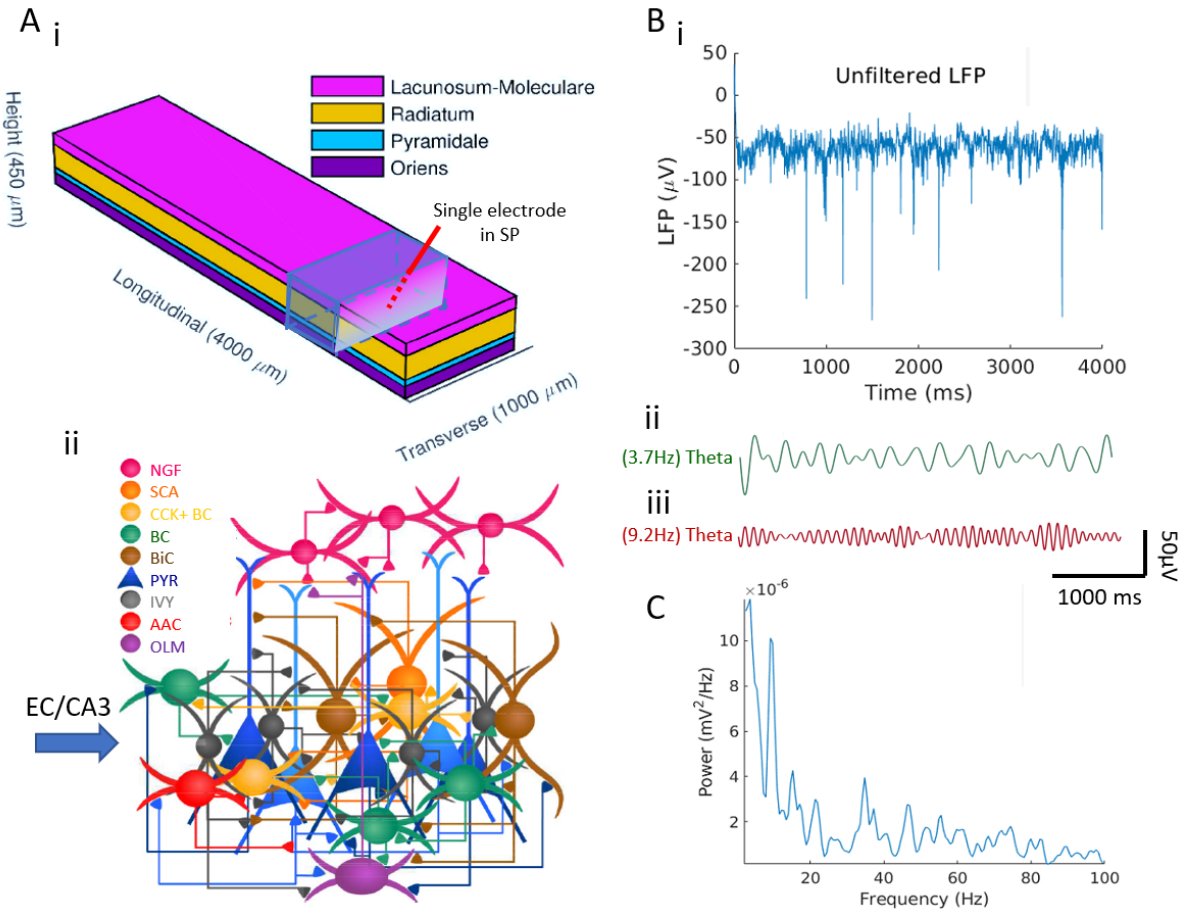

Figure 3.3: Theta rhythms in the segment model. A. (i): The model network is arranged in a layered prism. Image is adapted from Fig. 1 of [13]. The segment model shown in blue, represents 10% of the original volume. It contains 31,150 PYR cells, 553 BCs, 221 BiCs, 358 NGF cells, 40 SCA cells, 360 cholecystokinin-positive (CCK+) BCs, 881 Ivy cells, 164 OLM cells, 147 AACs. LFP output is based on a single micro-electrode placed in SP. (ii): The number, position and cell types of each connection are biologically constrained, as are the numbers and positions of the cells. Image is adapted from Fig. 1 of [13]. **B**. The segment network generates theta rhythms once the stimulation is reduced to 0.26Hz (it is 0.65Hz in the original detailed model). (i): Unfiltered LFP, (ii): filtered for low theta (peak at 3.7Hz) and (iii): filtered for high theta (peak at 9.2Hz). See Methods. **C**. Welch's Periodogram of the LFP shows a peak at two theta frequencies.

weights between the PYR cells, which we will refer to as $g_{pyr-pyr}$. In the minimal model, the external drive is only applied to the PYR cell population and is relatively weak (fluctuations of $\approx$ 10-30 pA) compared to what it is in the detailed model - about 10 nA (similar for the segment model). Also, the external drive in the detailed and segment models is applied not only to the PYR cells but also to the majority of the inhibitory cells. It is also important to keep in mind that the PYR cells in the segment model are

bombarded by substantially more inhibition in comparison to the minimal model, as there are eight different inhibitory cell types projecting to them, as compared to just the fast-firing PV+ cells in the minimal model. This means that in the segment model, relative to the minimal model, it is possible that the stronger external drive to the PYR cells and the stronger $g_{pyr-pyr}$ are required to counterbalance the larger inhibitory presence due to the multiple inhibitory cell inputs. Due to these aspects, we designed an expansive exploration of how the segment model depends on $g_{pyr-pyr}$ and the external drive to the PYR cells in creating theta rhythms. For the external drive, we explored both the stimulation parameter as well as the excitatory conductance from EC/CA3 to the PYR cells, which we will refer to as $g_{ec/ca3-pyr}$. This examination is schematized in Fig. 3.4A.

For each $(g_{pyr-pyr}, g_{ec/ca3-pyr})$ conductance pair, we performed a set of simulations to find the stimulation parameter that maximizes the theta power (3-12 Hz) for the given conductance pair. Given that these networks exhibit two theta peaks, a low and a high one, as shown by their Welch Periodogram, this analysis considers the stronger theta peak which is usually the one corresponding to the lower theta. A separate analysis for the higher theta peak power vs conductance pairs (ranges 6-12 Hz) can be found in Fig. 8.4. The theta rhythm dependence of our parametric explorations is shown in Fig. 3.4Bi-iii. From left to right we show the normalized theta power, the theta frequency and the required stimulation to maximize the theta power for each conductance pair examined. These results show that the normalized theta rhythm power increases with increasing $g_{pyr-pyr}$ or $g_{ec/ca3-pyr}$ (similar is the trend for the net theta power Fig. 8.2) while theta frequency approximately decreases with increasing $g_{ec/ca3-pyr}$ or $g_{pyr-pyr}$. We note that these patterns are disrupted for the largest $g_{ec/ca3-pyr}$ or $g_{pyr-pyr}$ conductance values, where the power of the networks is shifted to lower 'delta' frequencies below 3 Hz (see Fig. 8.3). From the heatmaps of the net theta power in Fig. 8.2 we notice that the power of the theta rhythms has significantly increased, approximately doubled, relative to the initial behaviour of the segment model shown in Fig. 3.3B. It is thus clear that there are particular parameter combinations that can significantly increase the power of the theta rhythms in the segment model to make it more robust.

Theta rhythm robustness and degeneracy of theta rhythm generation

To get an understanding of what underlies the results from our extensive parameter explorations, we took a detailed look at the inner mechanics of the network. We did this by examining two sets of conductance pair examples, *case a* (Fig. 3.4C,E,G) and *case b* (Fig. 3.4D,F,H), which correspond to small and large $g_{ec/ca3-pyr}$ values, respectively. These two examples exhibit elevated theta power relative to the initial behavior of the

segment, which we notice by comparing the amplitudes of the raw LFP recordings in Fig. 3.4Ei,Fi to Fig. 3.3Bi, and the periodograms in Fig. 3.4G,H to Fig. 3.3C, where the theta power can be seen to be larger by about two orders of magnitude. From our explorations, we observed the following: When $g_{ec/ca3-pyr}$ is small, the EC/CA3 afferents have to be strongly activated to elicit a strong response to the PYR cells, hence requiring a large stimulation value - see Fig. 3.4Biii. However, because these afferents connect to most of the inhibitory cells, a large stimulation value means strong concurrent activation of most of the inhibitory cells in the network. This is why the majority of the inhibitory cells in the network are fairly active in these regimes as shown in Fig. 3.4C. When $g_{ec/ca3-pyr}$ is large, the activation of EC/CA3 afferents don't have to be as strong (see corresponding stimulation value in Fig. 3.4Biii) to elicit a similar response of the PYR cells given that the $g_{ec/ca3-pyr}$ itself is already large. In this regime, the activity of most inhibitory cells is low exactly because the stimulation parameter is low and the inhibitory cells are not strongly activated. This can be seen in Fig. 3.4D.

Overall, these results expose the degeneracy of the theta rhythm-generating system which can occur in at least two ways depending on the exact pathway of activation of the PYR cells. It can be by either by low activation of the external afferents given a large $g_{ec/ca3-pyr}$ conductance value, inducing a high concurrent activation of the inhibitory cells (*case a*), or by high activation of the external afferents given a small $g_{ec/ca3-pyr}$ conductance value, inducing low concurrent activation of the inhibitory cells (*case b*). From this exploration, it is clear that regardless of the exact pathway of activation, what is critical for robust theta rhythms is the net amount of input to the PYR cells. Thus, the proposition brought forth by the minimal model that the theta frequency is controlled by the net amount of input that is received by the PYR cells seems likely. With the segment model, we are now in the position to directly examine whether this is the case.

Frequency control of theta rhythms and how they are initiated

Based on the minimal model's proposition, we examined the frequency of the LFP theta rhythms from the perspective of the net current received by the PYR cells irrespective of whether the pathway is of a *case a* or of a *case b* type. To do this, we took advantage of the numerous network simulations underpinning the heatmaps of Fig. 3.4B. Specifically, we examined whether the frequency of those networks correlate with the net current to the PYR cells. We selected a sample of 10 PYR cells from each of the segment models, as schematized in Fig. 3.5A, and computed the average and standard deviation of the net current that each of these 10 PYR cells received. An example of IPSCs and EPSCs received by a particular PYR cell is shown in Fig. 3.5Bi-ii. In Fig. 3.5C, we plot means

and standard deviations of the net current for all of the segment model networks in Fig. 3.4B, and we see that there is indeed a strong correlation between the theta frequency of each segment model and the net input received by the PYR cells (see Methods for calculations). This plot clearly demonstrates that the frequency of the theta rhythm can be predicted by the input to the PYR cells.

So far we've shown that the frequency of the theta rhythm relies on the net input received by the PYR cells in the segment model representing the smallest volume of tissue required to produce theta rhythms. Indeed if we chose to consider an even smaller tissue volume some of the inhibitory cells wouldn't even be part of the network purely because of their empirically derived connectivity profiles. At this point, we note that the presence of theta rhythms requires that PYR cells are connected with each other, since the rhythms do not exist if $g_{pyr-pyr}$ conductances are zeroed (see Fig. 3.3 and Fig. 8.5). That is, some recurrent excitation is required, as was already shown in [14]. Also, not surprisingly, given the large contribution of the external drive in the detailed model, the theta rhythm cannot be maintained if external drive to the PYR cells is removed by setting $g_{ec/ca3-pyr}$ to zero (see Fig. 3.3 and Fig. 8.5). Interestingly, what becomes evident in the segment model is that the generation of the theta rhythms is not specifically due to phasic drives from the inhibitory cells. Indeed, in these networks most of the inhibitory cell populations haven't yet organized into periodically firing populations. This is particularly noticeable in Fig. 3.4D where theta rhythms are present and can be seen to be due to the PYR cell population firing in bursts of theta frequency. Even more, we notice that the pattern of the input current to the PYR cells isn't theta-paced or periodic (see Fig. 3.5Bi). Despite this, the PYR cell population can organize into a theta frequency bursting population, and initiate the theta rhythm. This indicates that provided the appropriate level of net input to the PYR cells, a theta rhythm can start, and the initiation does not depend upon sequential, externally imposed inhibition form other rhythmically firing inhibitory cells. Of course, with a larger network, other inhibitory cells organize into periodically firing populations and contribute to the robustness and strength of the theta rhythm. However, at its initiation stages, we can clearly say that the theta rhythm 'sparks off' from the PYR cells.

Experimental constraints expand the understanding of theta-generating mechanisms in the hippocampus

Given the degeneracy in the segment model, an important aspect to consider is which of the theta rhythm-generating pathways might be occurring in the biological system. As a step in this direction, we turn to experimental observations from the intact hippocampus

in which PV+ cells were optogenetically manipulated [2]. Specifically, it was found that optogenetically silencing the PV+ cells significantly reduced the theta rhythm. Thus, removing PV+ cells in the segment model should have a detrimental effect on theta rhythms as well. As already noted, there are several sets of parameters that produce theta rhythms, and these are shown in Fig. 3.4B.

Let us go back to our previous examples of *case a* and *case b*. As can be seen in Fig. 3.4G,H, these two networks produce theta rhythms of similar power. To consider the experimental results of [2], we removed the PV+ cells (BCs, AACs, BiCs) from the two network cases to mimic an 'optogenetic' silencing, and we measured the resulting change in the theta rhythm. This was done by removing the PV+ cells from the network by zero-ing all of the inhibitory synaptic conductances emanating from them (Fig. 3.6A, Fig. 3.6B-G). It is evident that the PV+ cell removal has a negative effect on the power of the theta rhythms in *case a* but not in *case b*, simply based on their respective periodograms (compare Fig. 3.6F,G with Fig. 3.4G,H). Interestingly, there was a large increase in beta frequencies (13-22 Hz) with PV+ cell removal in *case a*. In *case a*, the net input to the PYR cells is the sum of both strong inhibitory and excitatory currents; thus, the rhythm cannot be maintained when the inhibitory inputs from PV+ cells are lost due to the severe disruption of the E-I balance. However, in *case b*, the net input to the PYR cells is mostly defined by the excitatory cells. In this case, removing the PV+ cells did not affect the E-I balance enough to disrupt the theta rhythms - indeed, it enhanced them (compare the peak values in the periodograms of Fig. 3.4H and Fig. 3.6G). This implies that the different E-I balances in the segment model that allow LFP theta rhythms to emerge are not all consistent with the experimental data, and by extension, the biological system. Thus it appears that lower $g_{ec/ca3-pyr}$ conductance values, as in *case a*, that rely on both inhibitory and excitatory currents are more consistent with the experimental data.

In Fig. 3.7 we show a summarized, aggregate comparison of the measurements for *case a* and *case b* segment models before and after the removal of the PV+ cells from the network. In *case a* (Fig. 3.7Ai-iv), removing the PV+ cells diminishes the theta power, while the frequency of the LFP signal and the net input current to the PYR cells which are correlated, remained intact. A noticeable decrease appears in the standard deviation of the current. This decrease reveals that removing the PV+ cells in this regime increases the 'noisiness' of the net current, or the fluctuation around its mean, which could potentially underlie the decrease in theta power in this example. Indeed, after examining the minimal model in the first part of this study, we proposed an 'inhibition-based tuning' mechanism for the theta rhythm, in which the PV+ cells 'tune' the PYR

cell firing and by consequence regularize and enhance the robustness of the theta rhythm. Such a mechanism is supported by the segment model for *case a*.

As shown for *case b* (Fig. 3.7Bi-iv), removing the PV+ cells actually increases the power of the theta rhythm while keeping the same theta frequency in the LFP signal and the same net input current. However, in this case, the standard deviation of the net current did *not* change, unlike for *case a*. Thus, from the perspective of the experiments of [2] theta rhythm generation via a *case a* type pathway seems more biologically realistic while it also supports the proposed inhibition-based tuning mechanism from the minimal model. In Fig. 3.7C, we provide a schematic of the biophysical theta generation mechanism and frequency control. This comparison with experiment brings forth the importance of understanding the inner mechanisms underpinning the dynamic output of a system, as high-dimensional models are likely to express degeneracy, which could however come forth via separable "pathways" of different biological implications.

3.5 Discussion

We have brought together two previously published models of the CA1 microcircuit that generate theta rhythms without oscillatory inputs. The two models mimic the intrinsic theta rhythms of an intact, whole hippocampus preparation [67]. One of them - the minimal model [53] - only has fast-firing PV+and PYR cells, whereas the other - the detailed model [14] - has eight different inhibitory cell types and PYR cells. The minimal model uses a simplified Izhikevich mathematical model structure for cellular representations, with parameter values determined from fits to experimental data from the whole hippocampus preparation, whereas the detailed model uses multi-compartment conductance-based cellular representations, determined from an extensive knowledge-based review of the literature [15].

The wide variety of cell types that make up brain circuits leads to high-dimensional sets of nonlinear, differential equations described by large sets of parameters incorporated into models. This makes application of theoretical analyses difficult and parametric explorations computationally expensive. In our approach of bringing together the two models in this study, we implemented a focused, hypothesis-driven parametric search of a fragment of the detailed model, the segment model, guided by the minimal model. This allowed us to establish a cellular basis for how intrinsic theta rhythms are generated and how their frequencies are controlled in CA1 microcircuits of the hippocampus. The importance of considering multi-level and multi-granular networks to understand brain phenomena as done here, was recently discussed by [49].

3.5.1 Summary overview

In [34], using heterogeneous PYR cell populations and quantification of SFA, Rheo and PIR building block features, we explored the robustness of the theta generation mechanism in the minimal model and found that it is sensitive to specific Rheo and PIR quantified values, but not to SFA. In the same study, we subsequently used PRCs to determine how the frequency of theta rhythms could be controlled, and proposed an 'inhibition-based tuning' mechanism in which inhibitory inputs to the PYR cell population allow a stable theta rhythm to emerge, given an appropriate net input to the PYR cells. This paved the way for investigations with the detailed model where this could be directly examined.

In this Chapter we presented the analysis of the detailed and segment models which went as follows. Since the detailed model was not explicitly built with the whole hippocampus preparation in mind, we computed EPSC/IPSC amplitude ratios and confirmed that they were in line with those observed experimentally in the whole hippocampus. Comparisons between minimal and detailed models validated the predicted connectivity balance in the minimal model and exposed notable differences.

We extracted a 'piece' of the detailed model of comparable cell numbers as the minimal model - termed the segment model - and showed that it could generate theta rhythms, albeit noisy and of low LFP power. This finding supports the experimental observations of [67] that the theta rhythm in the whole hippocampus is composed of a set of coupled oscillators, and only a part of the entire hippocampus is required to generate theta rhythmic output, an 'oscillator'. With this smaller segment model, we focused our investigation on the differences between the minimal and the detailed model, namely the PYR-PYR synaptic weights and the external drives.

We found a strong correlation between the theta oscillation frequency and the average net input delivered to the PYR cells. This indicates that the frequency of the LFP theta rhythm can be predicted by the inputs to the individual PYR cells of the network. Further investigations of the segment model revealed that the theta rhythm is initiated by the PYR cells but is regularized by the PV+cells since their removal caused a large decrease in the LFP power in the theta band, and an increase in the variability of the net current received by the PYR cells. Together, this supports an inhibition-based tuning mechanism for theta generation (see Fig. 3.7C).

3.5.2 Mechanism underpinnings and leveraging of theoretical insights

From our previous work we already knew that minimally connected PYR cell networks produced theta frequency population bursts on their own [55], but the majority of the PYR cells would fire during population theta bursts which is unlike the experimental observations of sparse PYR cell firing. With the inclusion of PV+ cells to create E-I networks, the population of PYR cells fired sparsely, which makes sense since the addition of inhibitory cells leads to less firing of PYR cells due to silencing from the inhibition. Relatedly, it has been shown that feedforward inhibition plays a role in maintaining low levels of correlated variability of spiking activity [115].

It is important to point out different PYR cell aspects in the minimal and detailed models. As mentioned, for the minimal model we know that the PYR cell population on its own can generate a population theta rhythm, and this is by virtue of its intrinsic properties that includes an SFA building block feature [55]. In that previous work, we had used a PYR cell model that is strongly adapting based on fits to the experimental data, or weakly adapting based on another experimental dataset in the same paper [54], that could produce theta frequency population bursts in both cases. As discussed in [54], it is unlikely that there are distinct types of biological PYR cells that are strongly or weakly adapting, but rather a continuum of adaptation amount dependent on the underlying balances of biophysical ion channel currents. Our explorations of the robustness of the theta generation mechanism in the minimal model revealed that theta rhythms are not sensitive to the specific quantified value of the SFA building block feature, so long as there is some adaptation. Thus, although the minimal model from [53] used a strongly adapting PYR cell model and the minimal model database used here started from this strongly adapting PYR cell model basis, it is unlikely that our results would be affected.

For the detailed model, the PYR cell model is based on experimental data in which some adaptation can be seen in the experimental recording, but is not apparent in the PYR cell model output of the detailed model (see Appendix of [14]). This then suggests that the prediction of the segment model that the PYR cells are the initiator of theta rhythms is not simply due to adaptation. It must thus involve other intrinsic characteristics of the biophysical PYR cell models. That excitatory networks can produce population bursts in of themselves is not new to the theoretical, modeling world, but it has not been previously shown that this could be the case in a biophysically detailed CA1 microcircuit model. An important candidate among PYR cell intrinsic properties that affect PIR is the hyperpolarization-activated cation channel (h-channel) [5]. The

h-channel has been shown to be a pacemaking current and contributes to sub-threshold resonance [18]. It has been a focus in general network modeling studies (e.g., [6]), as well as specific to inhibitory cells in the generation of coherent oscillations [138]. It is interesting to note that the h-channel, with its non-uniform distribution, has been shown to play an important role in shaping the output of LFP recordings, as determined from multi-compartment LFP modeling studies [122, 123, 146]. How exactly h-channels in PYR cells influence the dynamics and frequency of LFP theta rhythms in CA1 microcircuits will be interesting to investigate further. Aside from h-channels, t-type calcium channels may also be implicated in theta oscillation frequencies [88], and their role could be investigated further as well.

3.5.3 Physiological considerations and related studies

Based on the number of cells, the minimal and segment models are designed to represent a 'piece' of CA1 microcircuitry, and not the whole hippocampus preparation. However, the ability of these models to generate population theta rhythms on their own, is in line with the observations of [67] where transmission between portions of the whole hippocampus preparation were blocked with procaine (see their supplementary Fig.11). With each piece of tissue being able to generate theta oscillations on its own, the whole hippocampus would represent a set of coupled oscillators. Indeed, traveling theta waves in hippocampus and neocortex have been considered in this fashion [103, 179]. In previous work, we used phase-coupled oscillator models, assumed inhibitory coupling between oscillators and examined asymmetries in coupling strengths that could be responsible for the experimentally observed propagation of slow rhythms [147]. In that vein, it may be worth considering whether one could combine the mechanistic insights from microcircuit and coupled oscillator model studies.

The extensive set of simulations performed with the segment model showed that different cell-specific pathways dominate LFP theta rhythms of similar frequency and power, exposing degeneracy. While model degeneracy in high-dimensional model systems is expected, it underlines the importance of probing generation mechanisms whenever possible, and not just comparing outputs. There are multiple pathways in the circuitry, and at the *in vivo* level, one cannot unambiguously disentangle these pathways or have cell-type considerations [12]. Using the segment model, we were able to consider two distinct 'pathways' by which theta rhythms are generated - one where the EC/CA3 to PYR cell inputs dominated (*case b*) and another where they did not (*case a*). Based on perturbative responses to the model to mimic the experiments, only *case a* was in

accordance with experimental data [2]. We note that the differences between the cases could actually reflect differences in the contributions of particular inhibitory populations since, for example, the recordings that we compare our simulations to are taken from the superficial layers of the hippocampus. Indeed, in a very recent modeling study by [121] that built on the detailed model of [14], it was shown that deep and superficial PYR cells fire at different phases of the theta oscillation and are driven by different inhibitory cell populations. In that study, the authors found that in CA1, PV+BCs preferentially innervate PYR cells at the deep sublayers while CCK+ BCs are more likely to target superficial PYR cells. It is possible thus, that our *case b* regime reflects a theta rhythm relevant to the deep CA1 layers which is highly modulated by the CCK+ BCs, which, in contrast to the PV+BCs, happen to be particularly active in *case b*. However, what is clear from our work is that specific perturbations could determine the dominance of different cellular pathways by comparing LFP output characteristics.

The determination of an inhibition-based tuning mechanism for theta generation stemmed from this study is essential, as it forms a foundation from which to consider E-I 'balances' during theta rhythms from detailed physiological and experimental perspectives. E-I balances have been shown to be quite precise in feedforward networks from CA3 to CA1 [16], and fine-scale mapping studies show structured synaptic connectivity between different cell types in these regions [93]. Thus, in the absence of a detailed enough cellular-based network model one could not really situate emerging biological details' contributions to theta rhythms. On the other hand, in the absence of some mechanistic understanding, the importance of various biological details is challenging to contain. In this work, we have combined the strengths of minimal and detailed models, and have perhaps reached an 'inflection point' [64] by having enough, but not too much, biological realism to obtain a cellular-based mechanistic understanding. Had we started from models that were either more abstract or more detailed, model linkages and mechanism translations may have not been possible (i.e., too far from an 'inflection point').

3.5.4 Limitations and future work

Even though our modeling study sheds light on the foundation of the theta mechanism, more can still be unveiled in terms of the specific roles of the variety of inhibitory cell types in the segment model and their inter-relationships. Through optogenetic perturbations, experimental studies have already explored how PV+as well as SOM+ (putative OLM cells) cells affect intra-hippocampal theta rhythms [2]. Our previous modeling

work examined the contribution of BiCs, BCs and OLM cells to ongoing theta rhythms and LFP generation [35, 55] in light of these experimental studies. However, the segment model, with its complement of eight inhibitory cell types and its computational tractability, provides an exciting opportunity to extract and predict specific inhibitory pathways and their activation machinery during theta rhythms. Achieving this will help guide and target perturbation and stimulation paradigms in pathological states.

Besides [14], other detailed CA1 microcircuit models that include multiple inhibitory cell types have been developed ([43, 144, 166]). However, these models were used to examine higher level behaviours and theta rhythms were imposed, not generated within the models. Recently, a very detailed quantification of synaptic anatomy and physiology that includes short-term plasticity has been done, and is provided as a resource for the community [48]. It may be possible to examine these other detailed models in light of our mechanistic understanding, and further, to design a strategy that would appropriately include additional inhibitory cell types in the CA1 microcircuit model via the determined mechanism.

3.5.5 Concluding remarks and a proposal: A 'pacemaker circuit'

Six years ago, Siegle and Wilson's work [145] showed strong support for phase coding in the hippocampus, using the encoding and retrieval paradigm developed by Hasselmo [71] with theta rhythms. Recognizing the multi-layered aspects of theta rhythms - different cholinergic sensitivities, distinct phase relationships with different inhibitory cell types, low and high frequency theta types, different behavioural correlates and information processing, dorsal and ventral differences, heavy dependence on medial septal circuitry interactions [37, 38, 39, 75] - our work plants a seed.

Until now, it was not clear how one could consider theta rhythms from both cell-type pathways with E-I balances and functional behavioural perspectives. Our work suggests that there is no longer a need to separately impose theta rhythms on network models, as the cells in these networks are themselves part of the theta rhythm-generating machinery and this 'separation' eliminates some of the interactions that may be critical and thus hinder our understanding of the system. What is clear is that there *is* a theta rhythm generator in the hippocampus, i.e., intrinsic theta rhythms can be generated in a whole hippocampus preparation [67]. We know that interactions with the MS are important for theta, but we note that lesioning the MS reduces, but does not terminate theta rhythms [38, 174]. Modeling work has suggested that theta rhythms could arise

due to hippocampo-septal interactions [70, 170]. It is likely that interactions with the MS circuitry act to make the intrinsic hippocampus theta rhythms more robust, and impose theta rhythms in MS. Interestingly, experimental data has shown that rhythmic stimulation of the hippocampo-septal fibers can 'phase' MS neurons at that exact frequency due to rebound dependent h-channels, suggesting that the intrinsic hippocampus theta generator could be transferred to MS neurons via E-I interactions [110]. At present, we are not aware of any evidence supporting that the MS can generate theta rhythms on its own.

Thus we propose that CA1 PYR cells act as theta rhythm initiators tuned by the inhibitory cell populations to create a 'pacemaker circuit' - a core theta generator - in the hippocampus, with PYR cells sensitively dependent on 'pacemaking' h-channels. Amplification of these rhythms occurs due to inputs from the MS, while the net input received by the PYR cells controls the resulting theta frequency. From this intrinsic theta rhythm foundation, we can build, and in the process, disentangle the cellular-based and multi-layered aspects of theta rhythm generation and function in the hippocampus [21, 92, 86], and possibly other brain structures, since interestingly, functional connectivity studies have shown that the hippocampus is a brain hub [8, 118]. A schematic of our proposal is shown in Fig. 3.8.

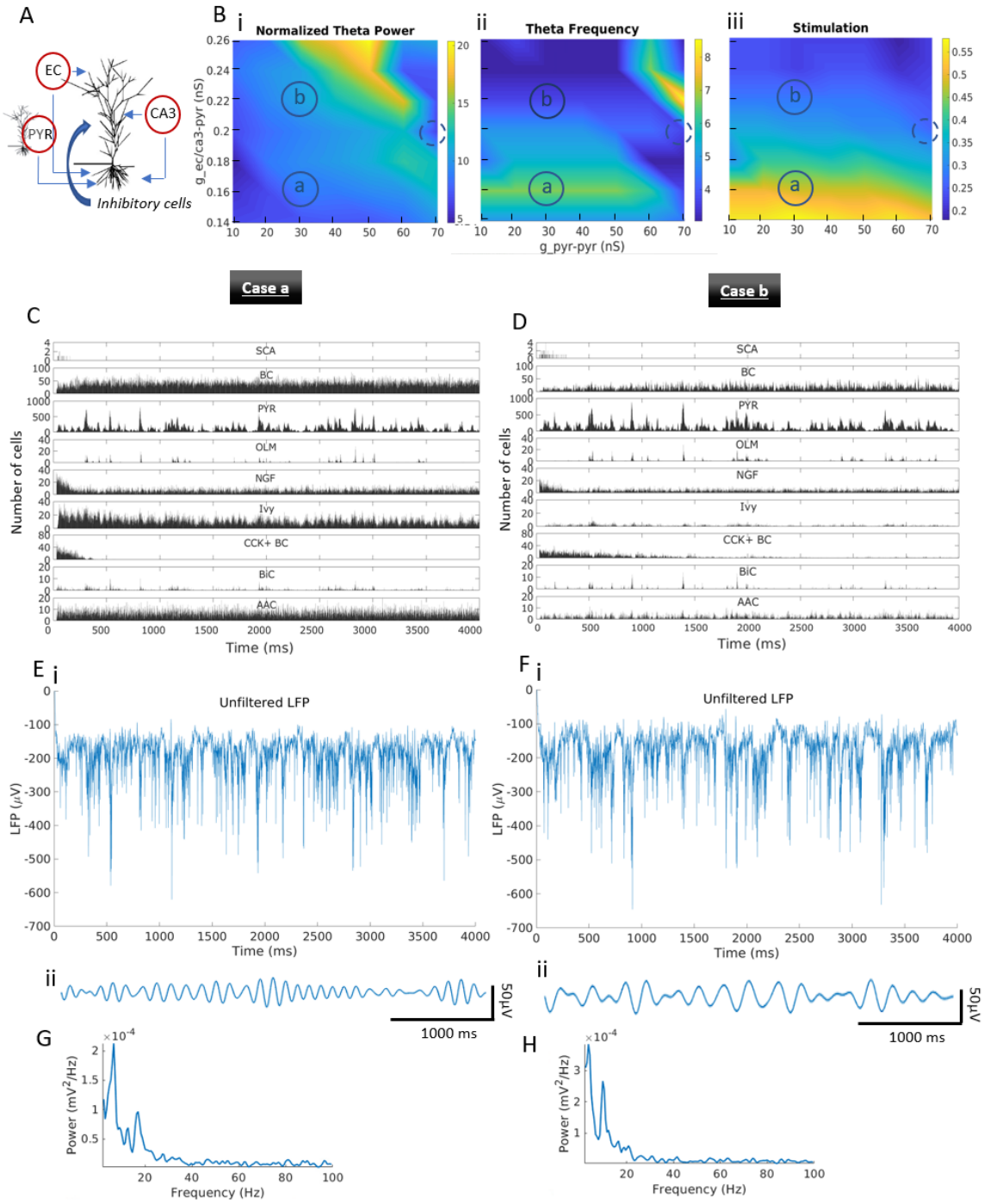

Figure 3.4: Theta power and frequency vs PYR cells' excitatory drives. A. Illustration of the parametric exploration of the excitatory drives to the PYR cells. **B**. Heatmaps of normalized theta power (i), frequency (ii) and afferent input stimulation (iii) as a function of $g_{pyr-pyr}$ and $g_{ec/ca3-pyr}$. Circled a and b regions represent *case a* and *b* networks respectively, with $g_{pyr-pyr} and g_{ec/ca3-pyr}$ values of: 30 nS and 0.16 nS for *case a*, and 30 nS and 0.22 nS for *case b*. Dashed circled regions represent initial network of the segment model as obtained from the 10% 'piece', extracted from the detailed model (Fig. 3.3), with $g_{pyr-pyr} and g_{ec/ca3-pyr}$ values of: 70 nS and 0.20 nS. **C**. Histograms of cellular activities for *case a*. Bin size = 1 ms. **D**. Same as C., but for *case b*. **E**. (i) Unfiltered LFP, (ii) Filtered LFP (peak at 6.7Hz), for *case a*. **F** (i) Unfiltered LFP, (ii) Filtered LFP (peak at 3.7Hz), for *case b*. **G**. Welch's Periodogram of LFP for *case a*. **H**. Same as G., but for *case b*.

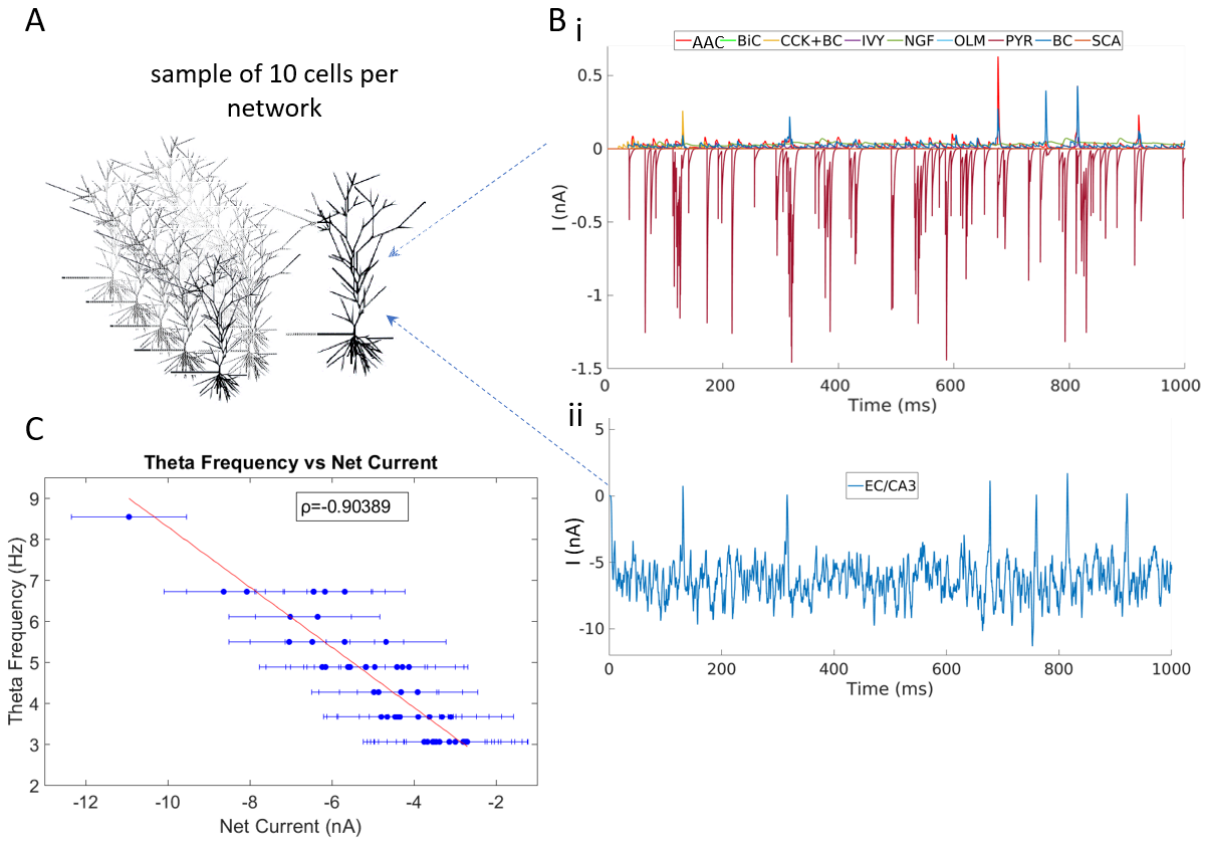

Figure 3.5: PYR cell net current input strongly correlates with frequency. **A**. Schematic to illustrate PYR cell sampling considered for net current analyses. **B**. Illustration of EPSCs and IPSCs onto the PYR cells. (i): current inputs from other PYR cells and the eight inhibitory cell types, and (ii): the excitatory drive from EC/CA3. **C**. Theta frequency plotted versus net current. Ten cells are randomly selected from each one of the 50 networks underpinning the heatmaps of Fig. 3.4B. Each dot represents the average across ten cells of the mean input current amplitudes to a given PYR cell of one of the 50 networks in Fig. 3.4B. Error bars represent the standard deviation of these averages. The correlation coefficient between the theta frequency and the net input current is ρ = -0.9, the p-value = 5.9x10^{-}19 and the slope of the red line of the linear regression fit is r=-0.7 Hz/nA, indicating that the LFP theta frequency increases by about one Hz every time the net drive increases by one nA.

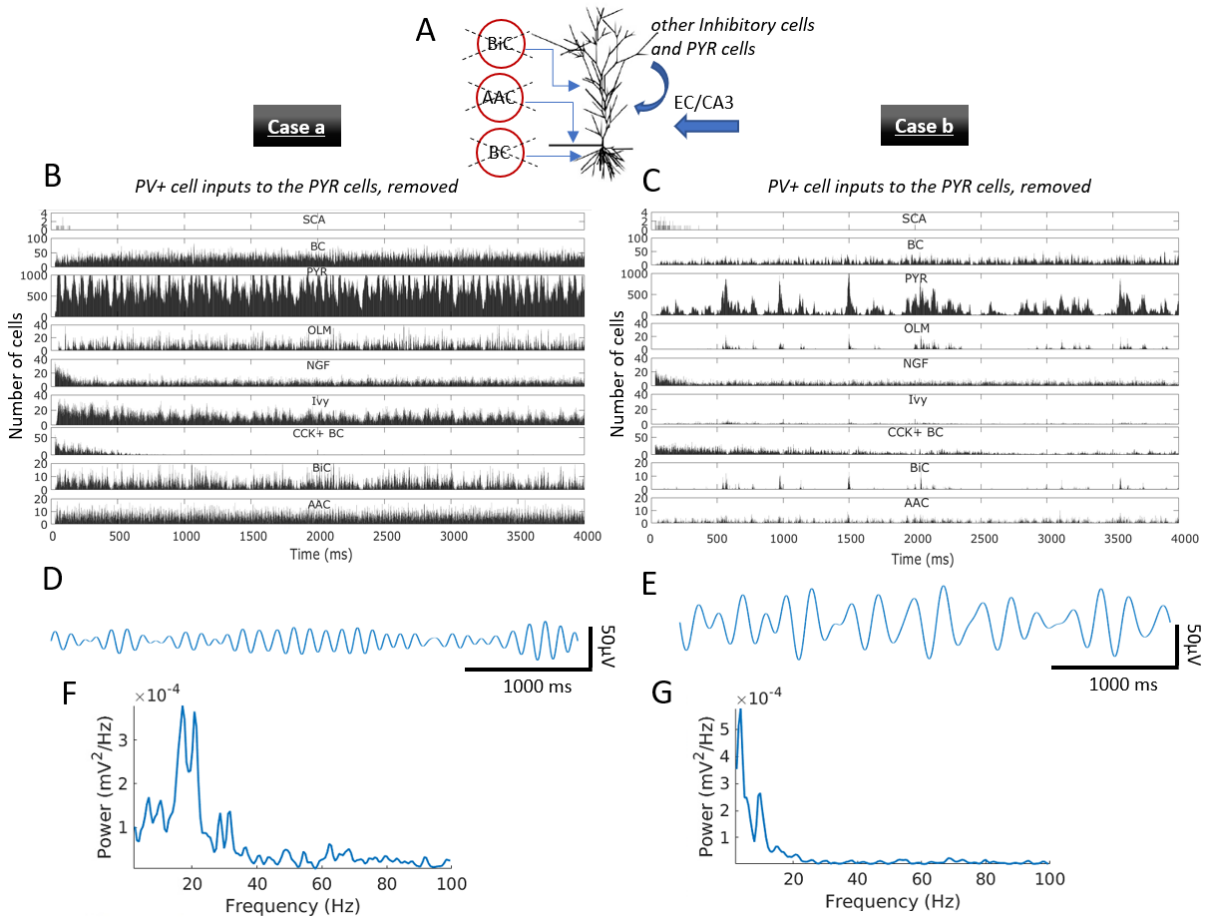

Figure 3.6: Effect on the theta rhythms with removal of input from PV+ cells. **A**. Schematic illustrating examination of the effects of PV+ cell (BCs, AACs, BiCs) input removal to the PYR cells. **B**. Histograms of cellular activities for *case a* with PV+ to PYR cell inputs removed. Bin size = 1ms. **C**. Same as B., but for *case b*. **D**. Filtered theta signal for *case a* with PV+ to PYR cell inputs removed (peak at 6.7Hz). **E**. Same as D., but for *case b* (peak at 3.7Hz). **F**. Welch's Periodogram of LFP for *case a* with PV+ to PYR cell inputs removed. **G**. Same as F., but for *case b*.

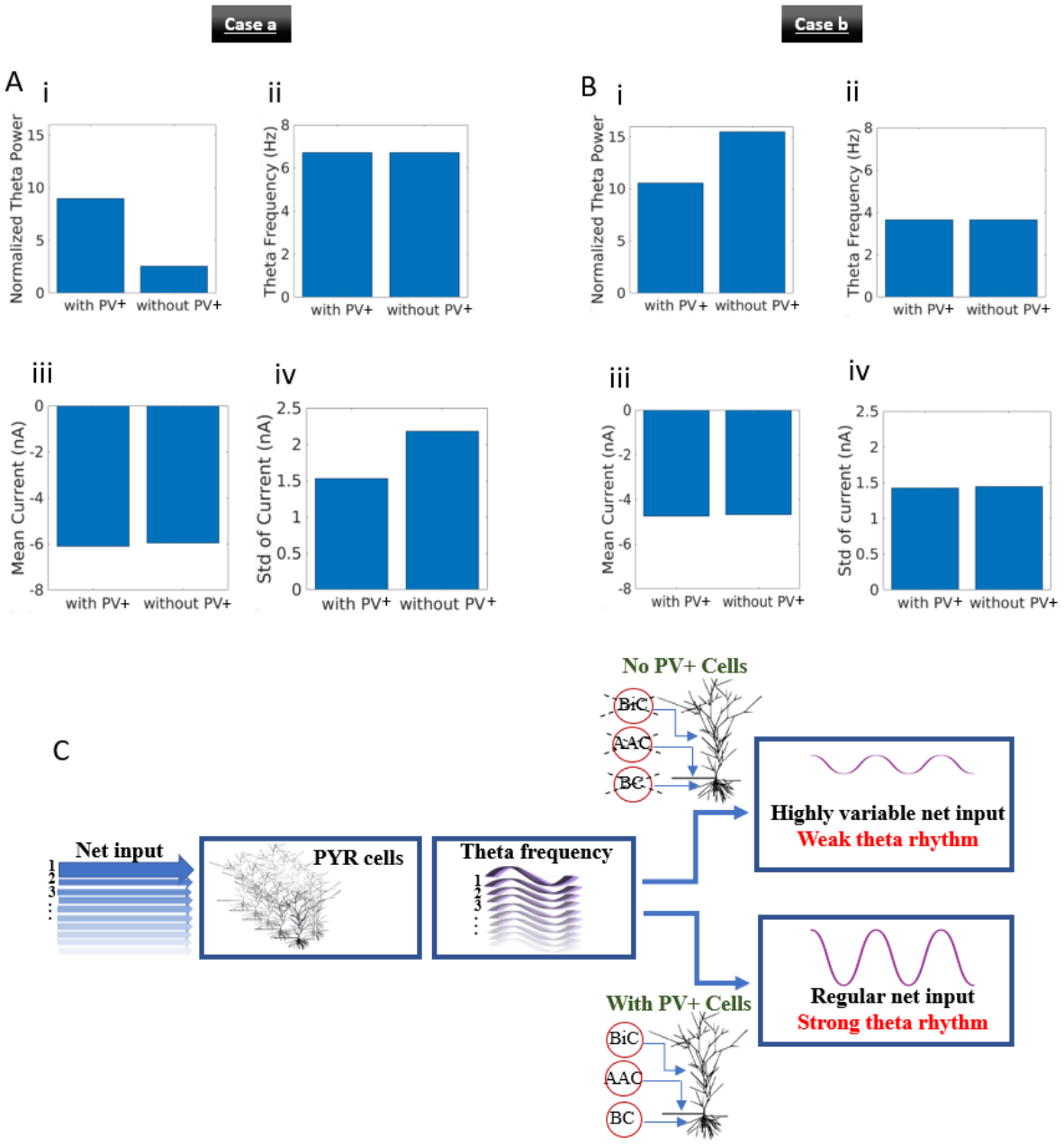

Figure 3.7: Aggregate comparison of theta rhythms before and after the removal of inputs to PYR cells from PV+ cells and schematic of 'biophysical theta'. **A**. Results for *case a*. (i): Normalized theta power, (ii): theta frequency, (iii): mean current, and (iv): standard deviation of current, with and without PV+ cells for *case a*. **B**. Same as **A**., but for *case b*. **C**. The net PYR cell input controls the resulting theta frequency. The PV+ cells contribute to the net input while they also regularize it and amplify theta power.

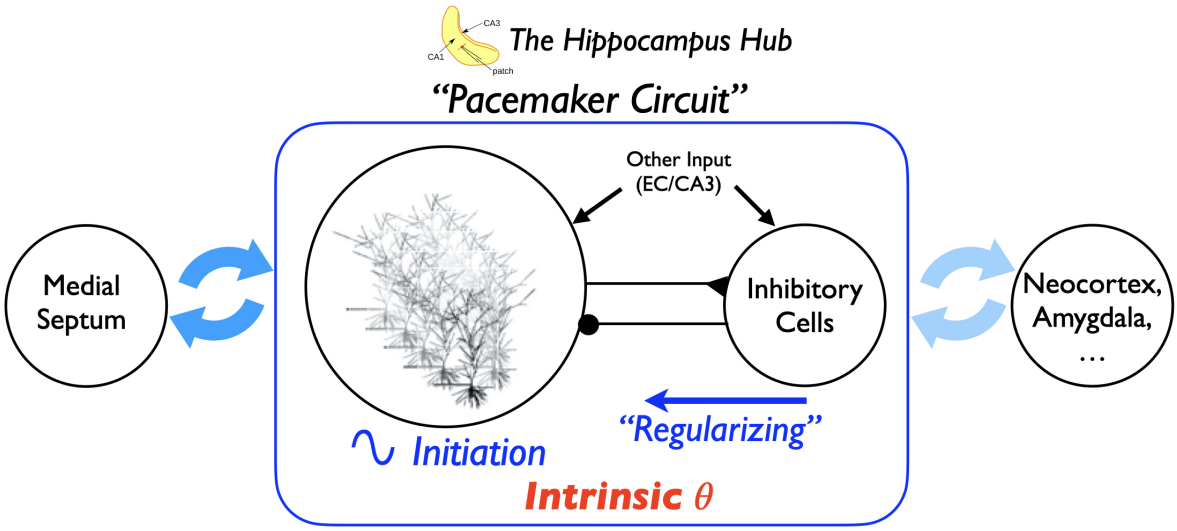

Figure 3.8: Proposing a theta pacemaker circuit in a hippocampus hub. The hippocampus can produce intrinsic theta oscillations on its own, without the need for any oscillatory input. In the work here, we have shown that theta rhythms can be generated by the PYR cell population, and are 'tuned' and regularized by the inhibitory cell population, as illustrated in the rectangle. We propose that this theta pacemaker circuit is amplified by connections with the MS via hippocampo-septal cellular interactions, as illustrated by the dark blue thick arrows. That is, the MS is not a theta rhythm generator, but rather acts to enhance and amplify the existing intrinsic theta rhythm in the hippocampus, and would play a role in setting the particular theta rhythm frequency. This would occur due to the MS cellular inputs affecting the net input current to the PYR cells in the hippocampus. The theta rhythm would further interact with other regions such as neocortex and amygdala, as illustrated by the light blue thick arrows [8]. The possibility of a hippocampus hub is supported by connectivity studies [118]. The whole hippocampus schematic is adapted from Fig. 1 of [79].

Chapter 4

Effect of External Drives on the Intrinsic Theta Rhythms in the Adapted CA1 Model

Conceptualization and project design of the work presented in this Chapter were jointly done by me and Dr. Skinner. Simulations and analysis of results were done by me.

4.1 Preamble

In the previous Chapters, we saw how an isolated piece of the CA1 microcircuit, the segment model, driven by noisy external inputs produces theta rhythms. Here we consider our segment model embedded in the whole CA1 circuitry, receiving inputs from the rest of the CA1 as it would if it was an undivided part of the CA1 network. Newly discovered connections reveal that the hippocampus CA1 also receives strong projections from the SUB [157]. We include these projections to the segment model and we formulate the adapted CA1 model driven by the SUB, the rest of the CA1 and the EC/CA3 as before. The adapted CA1 model is a more complete representation of the whole hippocampus preparation which includes the SUB [67]. We fit this model to available experimental data from the hippocampus preparation [79], and we demonstrate how the theta activity relies on the external drives.

4.2 Introduction

4.2.1 The SUB projections to the CA1

Even though it was known from older studies that the SUB targets all layers of the CA1 [94], the strength and nature of these projections hadn't been fully quantified. In a recent study by Sun and colleagues [157], the authors used rabies tracing to show for the first time the existence of non-canonical inputs from the SUB to the CA1, establishing a SUB-CA1 back projection pathway in contrast to the general belief of unidirectional information flow from the CA1 to the SUB. Overall, these studies demonstrated that comparisons of inputs to CA1 PV+ interneurons versus SOM+ interneurons showed similar strengths of input from the SUB. The authors determined that there are both excitatory and inhibitory SUB cells projecting to the CA1 as determined from their morphology and confirmed using immunochemical staining [157]. This indicates no preferential SUB innervation of CA1 excitatory or inhibitory neurons, instead they found that the proportions of SUB excitatory versus inhibitory cells projecting to either CA1 excitatory or inhibitory neurons are similar. These connections could now explain the directionality of the theta travelling wave from the SUB to the middle CA1 and CA3 reported in [84], and shed light on the mechanisms of theta. In this Chapter, we take advantage of these recently discovered connections and we incorporate them into our segment CA1 model.

4.2.2 Experimental data of PV+ and SOM+ cell firing during intrinsic theta rhythms

In the previous section we showed how the externally imposed feed-forward and recurrent excitation of the PYR cells influences the network dynamics. We found that smaller $g_{ec/ca3-pyr}$ values favor the strong recruitment of most interneurons and yield networks in which the presence of PV+ cells is pivotal for theta. More recent experimental evidence provides specific information with respect to the firing patterns of the PV+ cells during theta rhythms. Huh and colleagues [79], showed that individual PV+ cells fire with an inter-burst frequency analogous to the frequency of the ongoing theta rhythm (Fig. 4.1Ciii), as well as a fast intra-burst gamma frequency (Fig. 4.1Civ). In this Chapter we leverage these data to fit the adapted CA1 model.

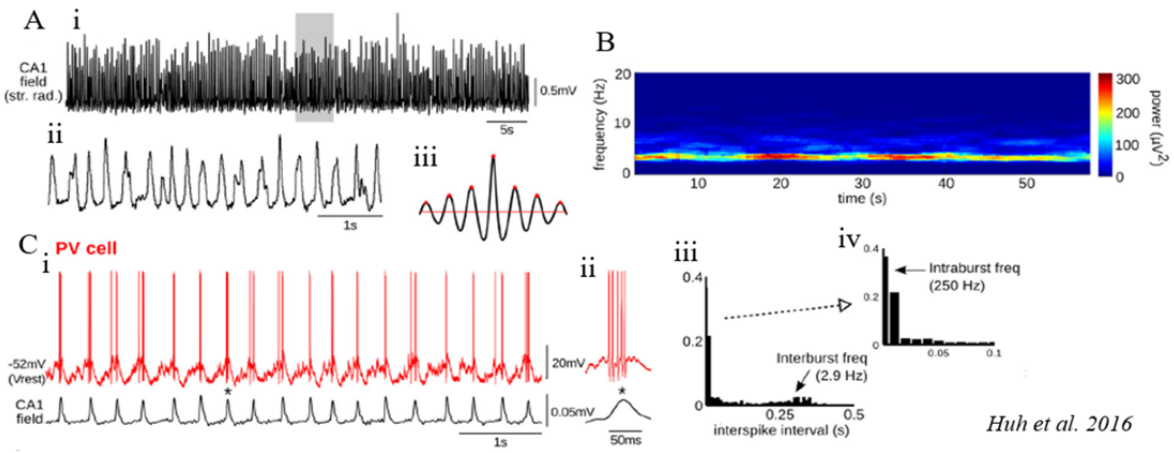

Figure 4.1: CA1 PV+ interneurons firing during theta rhythms. A. (i) An example LFP signal (5s highlighted segment expanded below), (ii) auto-correlogram and (iii) power spectrogram. **B.** Illustration of the stability of LFP rhythm. **C.** (i) A typical PV+ exhibited rhythmic bursts of several spikes. This PV+ neuron fired 3.2 spikes per burst (mean). The spikes marked with an asterisk are expanded on the right (ii). The ISI histogram (iii) shows one peak for intra-burst frequency (inset, zoomed-in for clarity in (iv)) and a second peak for inter-burst frequency. Figure adapted from [79].

4.3 Methods

4.3.1 Model development

Addition of SUB inputs to the CA1

Connectivity information between the SUB and the CA1 was derived from recent rabies tracing studies by [157] and [156]. From [157], we derived the number of excitatory and inhibitory connections projected onto every CA1 layer and we divided these connections across the CA1 cell types according to their relative number ratio in each layer. From [156], we derived the post-synaptic densities onto the CA1 cells.

4.3.2 Model fitting and application of experimental constraints

The network clamp

To explore the effect of the post-synaptic weights onto the PV+BC population, we used a network clamp technique which is part of the software package, SimTracker [13]. This technique allows one to take a snapshot of the incoming synaptic input received by any particular cell in the network. We applied it as follows. First, we obtained the output of an initial full-network simulation and ran network clamp simulations on a PV+BC.

We altered the incoming afferent synapse weights (but not the incoming spike trains) until the cell fired in accordance with the experimental data. This approach gives an estimate of how the synaptic weights affect the PV+BC firing. Guided by this estimate one can tune the post-synaptic weights accordingly in full network simulations to obtain networks of appropriate cellular firings. We explored these synaptic weights as explained below. The experimental data are leveraged from voltage recordings of PV+ cells during ongoing theta rhythms [79].

The parametric exploration of the post-synaptic densities

To search the parameter space of post-synaptic weights and determine how these weights affect the cellular firings of a PV+BC, we developed the following pipeline of analysis.

Step 1. We explore the post-synaptic weights onto a given PV+BC. Starting from a given set of reference values (r.v.), we vary the post-synaptic weights from all eight pre-synaptic cell types to the PV+BC. To do this we search a range of post-synaptic weights for each pre-synaptic cell type. This range is [-50% (r.v.), +50% (r.v.), 25%] (*start value*, *end value*, *step*), and as such it contains 5 values which are:

$$\text{-50\% (r.v.)} \mid \text{-25\% (r.v.)} \mid \text{r.v.} \mid \text{+25\% (r.v.)} \mid \text{+50\% (r.v.)}$$

We explore the co-variation of these values. Given that every post-synaptic weight can take 5 values and given that we explore a set of eight post-synaptic weights, we have a total of $5^8 = 390594$ configurations.

Step 2. We perform network clamp simulations for all configurations and store the voltage trace of the PV+BC for each configuration.

Step 3. We calculate the ISIs of every voltage trace using the open-source eFEL library (https://github.com/BlueBrain/eFEL).

Step 4. We plot the mean ISI across all configurations shown in Fig. 4.2.

For completion purposes, we list below alternative methods of analysis and data visualization methods considered but not used in this thesis:

- To establish if the voltage trace of our PV+BC network clamp simulations matches the experimentally recorded PV+ cell traces, we created a surrogate distribution of the ISIs of the PV+BC experimental recordings and compared this distribution to a second distribution created from the PV+BC ISIs from our network clamp simulations. The comparison of the two distributions was done by means of overlap.

- Aside from the mean ISI, we have considered other, more sophisticated types of analysis which we mention here briefly. In the process of designing this analysis, we determined that plotting the ISI overlap as a function of the eight synaptic weights would be a high dimensional problem hard to visualize. Therefore, we anticipated that we would need a dimension reduction technique to visualize the eight-dimensional space of synaptic conductances and determine how the ISIs depend on those. We employed the t-Distributed Stochastic Neighbor Embedding (t-SNE) (`https://lvdmaaten.github.io/tsne/`) and used it to examine if the combinations of weights that yield high ISI values form clusters. The level of sophistication of this technique was deemed unnecessary for our specific problem but it might be useful for future analysis.

4.4 Results

4.4.1 The adapted CA1 model

Starting from the segment model of *case a* of the Chapter 3 we add the SUB and CA1 inputs and we fit the model according to experimental constraints. Addition of the external SUB and the CA1 inputs yields the adapted CA1 model of Fig. 4.3. We will refer to this as the reference network.

4.4.2 Model fitting

To fit the reference adapted CA1 model to the experimental data of Fig. 4.1 we employ the network clamp technique as explained in the Methods. We investigate how the post-synaptic weights of the PV+BC influence the firing rate by means of the mean ISI. In Fig. 4.2 we show the result of a grid search representing the co-variation of eight post-synaptic conductances. Following the simple visualization scheme shown in Fig. 4.2, we can easily discern the effect that each presynaptic cell has on the firing rate of the PV+BC. We distinguish a number of patterns. As expected, incrementally strengthening the inhibitory PV+BCs post-synaptic weights decreases the PV+BC firing rate (larger ISIs). However, for a critical value of the CCK+BC to PV+BC conductance, we notice a sudden decrease in the PV+BCs firing frequency which can be up to 20Hz. This transition always occurs if the CCK+BC to the PV+BC conductance reaches a critical value. Once that critical value is reached, a small increase in the rest of the conductances, especially the PV+BC-PV+BC, mediates an abrupt elevation of the PV+BC mean firing rate (by means of ISI). This observation reveals that provided that the network operates

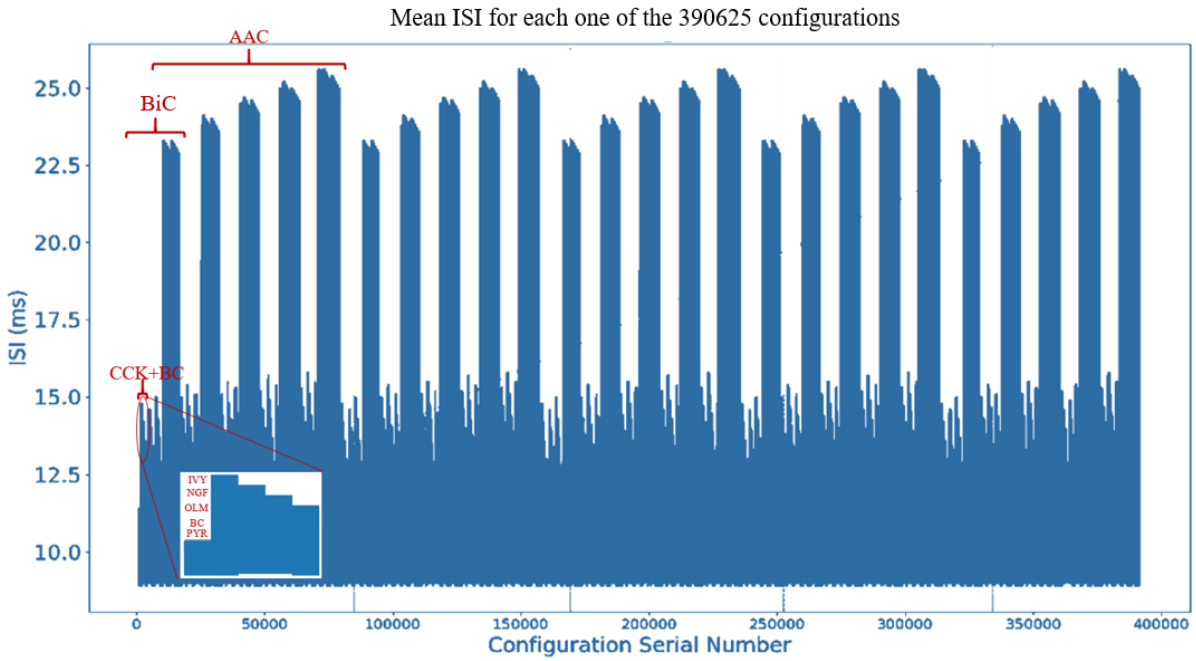

Figure 4.2: The PV+BC ISIs as a function of the configuration number of the post-synaptic weight combinations. We iterate over the post-synaptic PV+BC weights according to the method described Methods and in Fig. 8.1. The largest group of five repetitive motifs represent incremental increases of the five AAC post-synaptic weight values. Within each of these motifs another group of five repetitive motifs represents incremental increases of the five BiC post-synaptic weight values. Equally within each one of these five motifs another group of five similar motifs represents incremental increases of the five CCK+BC post-synaptic weight values and so on. Inset shows incremental increases of the other five post-synaptic cell weights which don't influence PV+BC firing significantly.

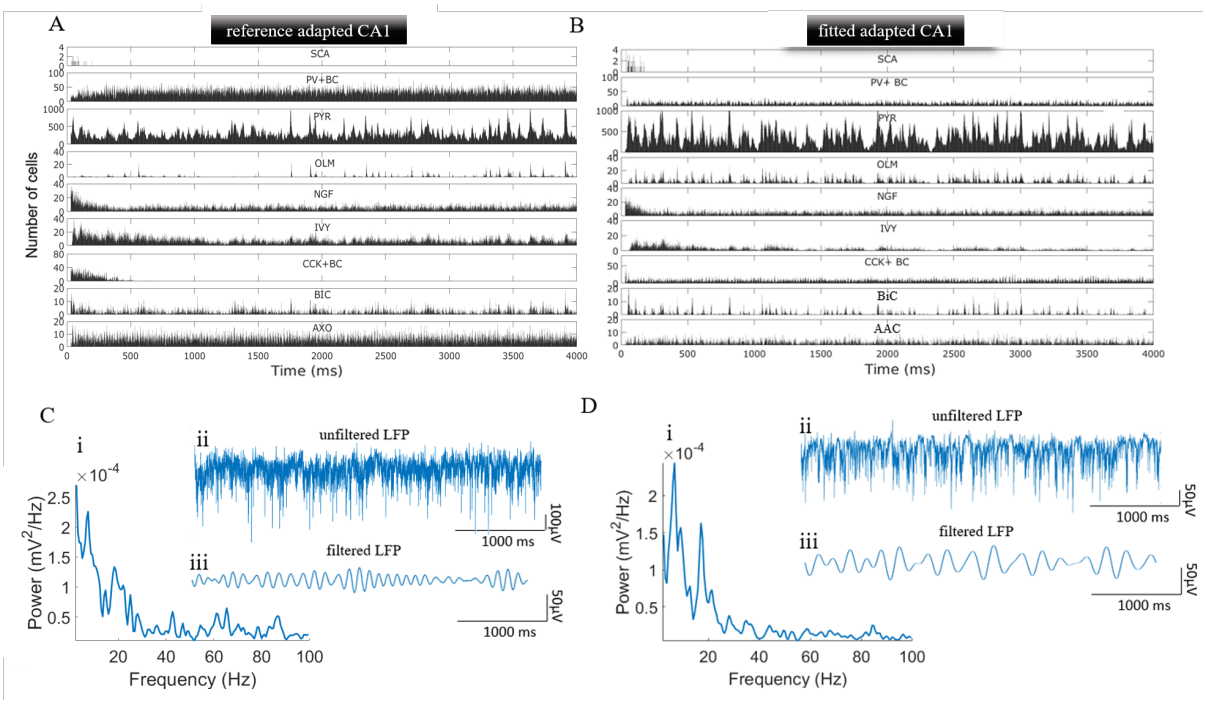

Figure 4.3: The reference and the fitted adapted CA1 networks. A. Histograms of cellular activities for the reference adapted CA1 network. Bin size = 1ms. **B**. Same as A., but for the fitted adapted CA1 network. **C.** (i) Welch's Periodogram of LFP, (ii) Unfiltered LFP, (iii) Filtered LFP (Peak 6.7Hz), for the reference adapted CA1 network. **D.** (i) Welch's Periodogram of LFP, (ii) Unfiltered LFP, (iii) Filtered LFP (Peak 5.6Hz), for the fitted adapted CA1 network.

close to this critical point, small changes in the CCK+BC activity can induce a sudden change (increase or decrease) of the PV+BC firing rate. Such a critical point always exists, regardless of the combination of the rest of the post-synaptic conductances as shown by their co-variation in Fig. 4.2.

Guided by this exploration we tuned the inhibitory conductances to the PV+BCs' of the control network by increasing their inhibitory post-synaptic conductances by a factor of two. Aside from the PV+BCs, the results of [79] apply to all PV+ cells which also include the BiCs and the AACs. We thus increased the inhibitory post-synaptic conductances to the AACs also by a factor of two and obtained the network of Fig. 4.3B, which behaves according to the experimental data Fig. 4.4, as all the PV+ cells fire at theta. Tuning the PV+BC and AACs corrected the firing rate of the BiCs without extra tuning. The network of Fig. 4.3B matches the experimental observations of [79]. This can be verified with inspection of Fig. 4.4, which shows the firing patterns and firing frequencies of the PV+ cells in the reference and fitted adapted CA1 networks comparatively.

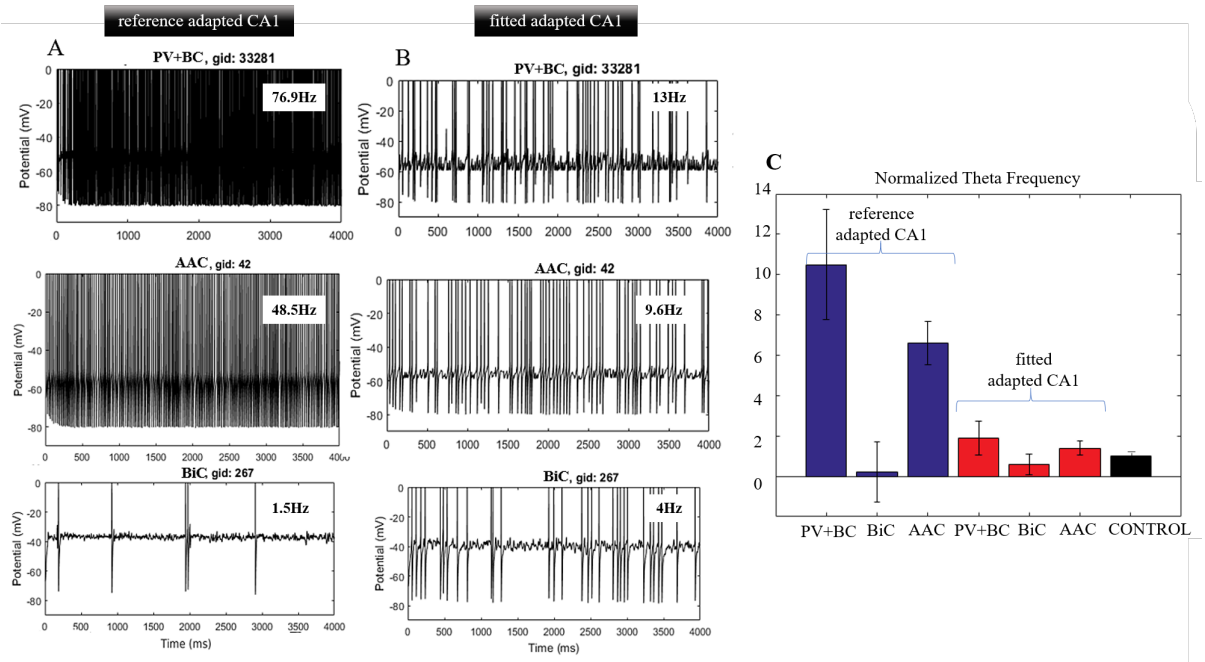

Figure 4.4: Mean firing rate of PV+BCs in the reference and fitted adapted CA1 models. A. Example voltage traces of the three PV+ cell types, the PV+BC, the AAC and the BiC for the reference adapted network and **B.** same, for the fitted adapted network. **C.** Normalized frequency of the three PV+ cell types (PV+BC, BiCs and AACs) for the two cases. Blue: reference adapted CA1 model, red: fitted adapted CA1 model, black: experimental data from 11 PV+ cells, that fired with a mean frequency $4.1 \pm 0.4Hz$, p=0.23 [79]. Firing frequency of PV+ cells in each case is normalized to the frequency of the network theta rhythm. To do this normalization we divided the frequency of a given PV+ cell to the frequency of the theta rhythm as given by the power spectrum.

4.4.3 Model validation

To validate our fitted adapted CA1 model, we once again run a validation test, by selectively removing all the output from the PV+ cells to the rest of the network, anticipating a reduction in the theta rhythm as witnessed in [2]. In Fig. 4.5 we indeed notice that removing the PV+ cell projections to any other cell type in the network, significantly decreases the theta rhythms.

4.4.4 Effect of external drives on the theta rhythms

So far we have examined the adapted CA1 model output in the presence of the SUB, CA1, EC and CA3 external inputs. We noticed that adding the SUB external input changed the network LFP output but not significantly. What is more in [84] the authors showed that theta rhythms emerge, even in the absence of external CA3 inputs. That

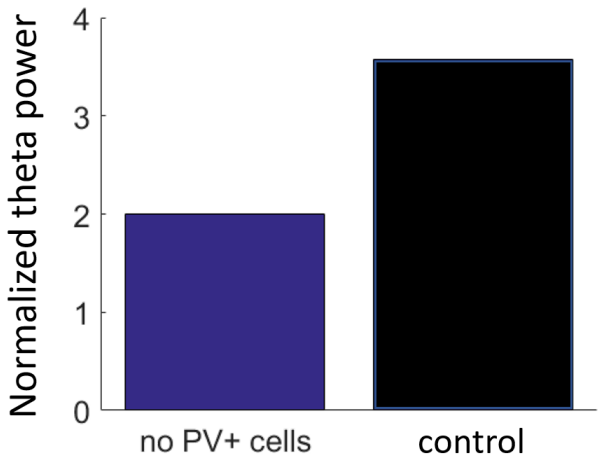

Figure 4.5: Effect of PV+ cell removal on the normalized theta power of the fitted adapted CA1 network. Bar graph of the normalized theta power of the fitted CA1 adapted network once the PV+ cells are removed, mimicking the test by Amilhon and colleagues [2]. The normalized theta power is defined again as the maximum theta power (net theta power) in the power spectrum, divided by the mean power across all frequencies. The control network is the fitted CA1 adapted network.

leads us to the hypothesis that the exact source of external excitation is less critical in driving the theta oscillations and that as long as some external excitatory drive exists, theta rhythms will emerge. Given that the nature of our external input is noisy and not phasic, the theta rhythms are clearly generated by internal process of the CA1 network and possibly, the SUB alone is enough to drive the network. To explore this hypothesis we decompose the external drives driving the constrained CA1 network, and we examine how each one of these inputs contribute to theta rhythms. In Fig. 4.6 we can see the results of this decomposition. Stronger theta responses are generated by external inputs from the CA3, while weakest responses by inputs from the rest of the CA1. EC and SUB inputs also produce theta activities that are close to four times stronger than the other LFP activities in the network, and are very similar to control (when all four external inputs are present). As expected, these results show that the activation of external afferents, even if they are only noisy and not phasic, strengthens theta rhythms compared to an isolated segment that only receives inputs from the rest of the CA1. It is interesting on the other hand, that a small baseline theta rhythm can be detected if the segment is driven only the rest of the CA1.

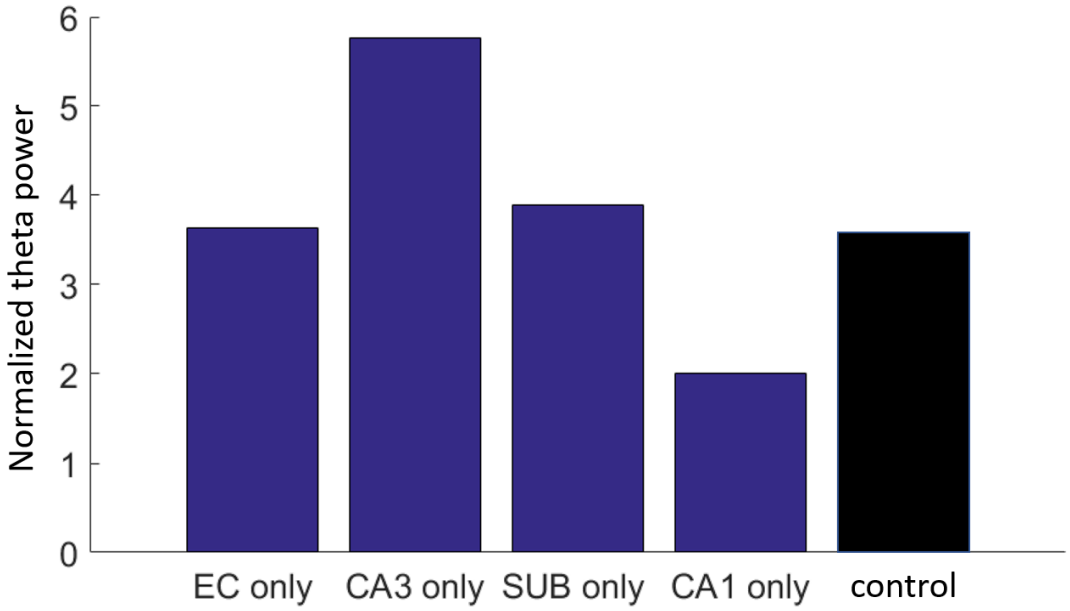

Figure 4.6: Effect of external drives on the normalized theta power of the fitted adapted CA1 network. Bar graph of the normalized theta power of the fitted CA1 adapted network as a function of separate external drives from EC, CA3, SUB and the rest of the CA1. The control network is the fitted CA1 adapted network which is driven by all previous external drives.

4.5 Summary and conclusions

In this Chapter we developed the adapted CA1 model by fitting and then validating the model against experimental data. We revealed the effect of external drives on the theta rhythms of the network. Our findings showed that the theta rhythms are not solely dependent on external drives from the EC and the CA3 that we used in the previous Chapter, but can also occur via inputs from the SUB. Weaker responses were induced by inputs from the rest of the CA1.

Chapter 5

A Cell-Type Dependent Explanation of the Generation Mechanism of the Intrinsic Theta Rhythms

The work presented in this Chapter (conceptualization, project design, simulations and analysis) was done by me.

5.1 Preamble

Can we apply the findings that stemmed from the investigations of the segment model to explain how the theta rhythm is generated in the full CA1 model and by extension the biological system? The full CA1 model was developed by a different group [14], but we regard that in light of the segment model analysis there are further explanations one could dissect with respect to the theta mechanism that the previous developers didn't directly provide. In this Chapter we explain the theta generation mechanism in the full CA1 model of [14], and obtain a more comprehensive perspective of the cell-type contributions.

Table 5.1: Comparison of the segment and the full CA1 model.

	Biophysical detail	**Principles of theta rhythm generation** PYR cell mediated initiation of θ rhythm	Inhibition mediated termination of PYR θ bursts	**Computational efficiency**
Segment model	YES	YES	NO	YES
Full CA1 model	YES	YES	YES	NO

5.2 Introduction

5.2.1 The theta generation mechanism and the termination of the theta bursts in the full CA1 model

We've shown so far that the theta frequency in the segment model depends on the net current input of the PYR cells. As this network is only a segment and many of the inhibitory connections are significantly reduced, many of the inhibitory populations haven't yet organized into rhythmically firing populations. However, this exact attribute of the segment network allowed us to distinguish the PYR cells as the rhythm generators, which despite being driven by noisy inputs, organize into theta bursting populations. The segment model indeed has the advantage of computational tractability, while the full scale model represents a large network and generates more robust dynamics (Table 5.1). As we will see, taking advantage of these properties of the full CA1 model we can explain the termination of theta bursts.

5.3 Results

5.3.1 The theta mechanism based on a macroscopic examination of the cellular activity

The raster plots of Fig. 5.1A show a 4 sec interval of cell firing while Fig. 5.1B shows an interval of the last 500 ms of cell firing. In Fig. 5.1A, we notice several trends across the inhibitory cell firings. Some of the inhibitory cells produce thin, theta frequency bursts, whereas others fire continuously, interrupted periodically by theta-paced windows of quiescence. In the first category belong the BiCs and OLM cells and in the second category belong the AACs, CCK+BCs, PV+BCs, NGF cells and IVY cells. These two

categories arise from the separate excitatory sources that drive these populations. The theta bursting BiCs and OLM cells are primarily driven by the PYR cells and as a result they mirror their activity, whereas the noisy firing inhibitory cells are primarily driven by the noisy EC/CA3 excitatory afferents. Consequently, the OLM cells and the BiCs induce theta-paced windows of quiescence in the firing patterns of the rest of the interneurons which are already discernible in Fig. 5.1A and will be explained below.

5.3.2 The theta mechanism based on closer examination of the cellular activity

The full CA1 model is characterized by larger cellular populations and stronger connectivities across cell types compared to the segment model, which is just an isolated piece of it. As a result, the inhibitory populations (AACs, PV+BCs, CCK+BCs and SCA cells) in the full CA1 model organize into rhythmically bursting gamma firing populations (ING networks) as we can see in Fig. 5.1B.

What is less discernable in the segment relative to the full CA1 model networks, is the sharp termination of any given theta burst shown in Fig. 5.1B. This termination mechanism relies upon the strong connectivity between the inhibitory cells which was significantly decreased in the process of "cutting" the network to create the segment model. Let us take a closer look at the last 500 ms of the raster plot in Fig. 5.1A expanded in Fig. 5.1B. Within it, let's examine a given theta burst and particularly the interval from 3800 to 3900 ms, an interval spanning from the termination of the previous burst to the end of the next. We will first accept that as found earlier, the duration of this interval, which defines a theta cycle, is controlled by the PYR cells and the net input they receive. What is more, we discussed briefly in Chapter 3 that the $g_{pyr-pyr}$ promote the progressive activation of more and more PYR cells forcing them to organize into clusters of bursting cells. Here too, the PYR -PYR conductances reinforce the progressive recruitment of the PYR cells which maximizes at the climax of the theta peak (i.e. at 3900ms). The sharp termination of the theta burst that follows next, involves the sequential recruitment of inhibitory populations according to four steps.

First, the strong recruitment of the PYR cells at the theta peak induces the strong activation of the BiCs and OLM cells. Second, the BiCs form very strong connections with the CCK+BCs, thus their activation strongly inhibits the CCK+BC population. Third, the CCK+BCs form very strong connections with the PV+BCs and as a result the strong inhibition of the CCK+BCs induces a strong disinhibition of the PV+BCs. Once the PV+BCs are strongly disinhibited, meaning activated, as a fourth step, they

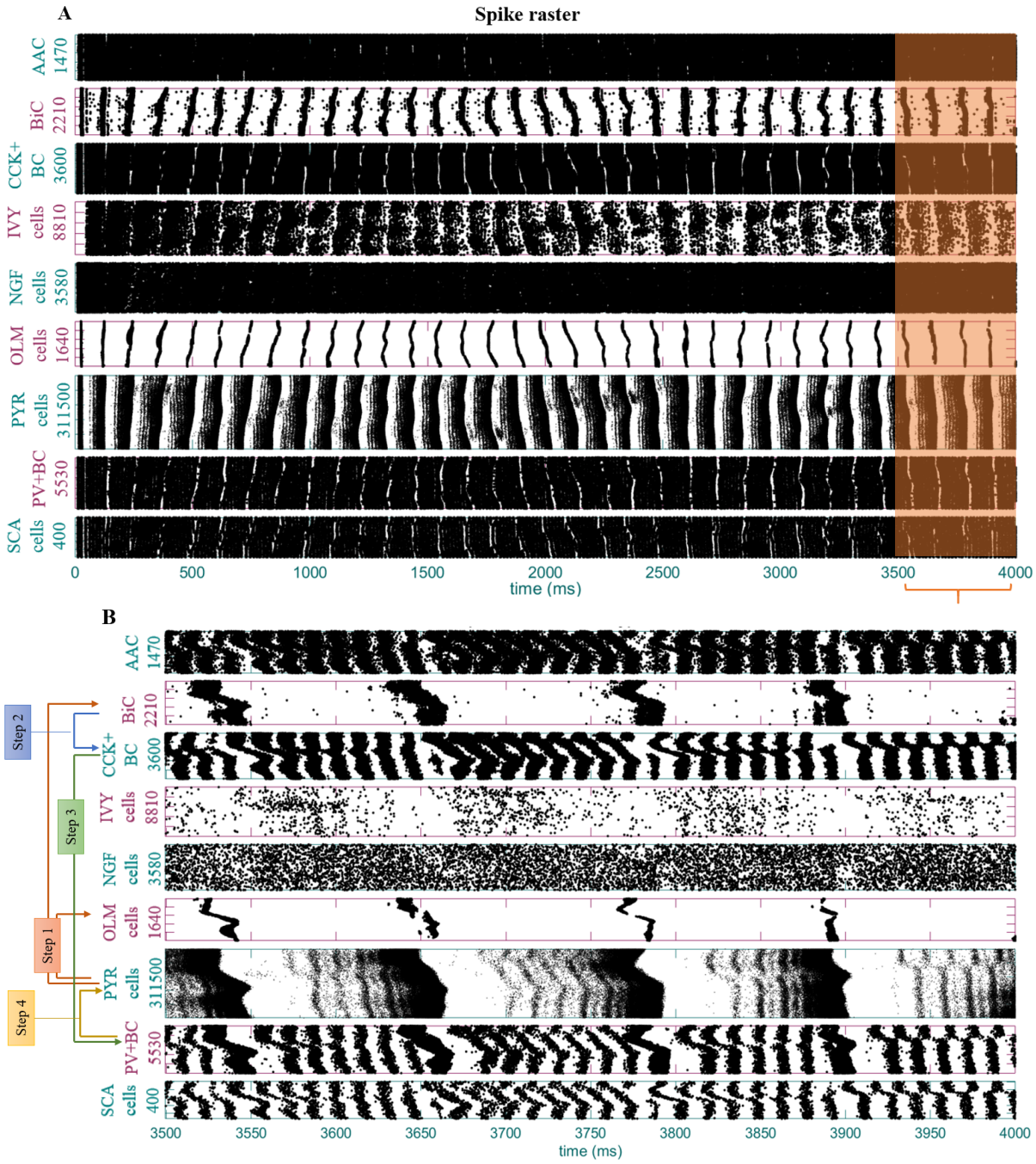

Figure 5.1: Raster plots of the eight inhibitory cell types and the PYR cells in the original full CA1 model. Numbers on the y-axis refer to the number of cells of the given cell type. **A.** A four second plot and **B.** The last 500 ms of **A.** magnified. Steps 1-4 show the sequential activation of the inhibitory populations leading to the termination of the PYR cell theta burst. Step 1: The PYR cells activate the OLM cells and BiCs. Step 2: The BiCs inhibit the CCK+BCs. Step 3: The CCK+BCs disinhibit the PV+BCs. Step 4: The PV+BCs inhibit the PYR cells and terminate the theta burst. These steps are also shown in the histograms of Fig. 5.2B.

inhibit the PYR cells (whom they form very strong connections with) and cause the sharp termination of the theta burst (Fig. 5.2). It is worth noting that as our grid search of Fig. 4.2 showed, if the segment model network sits close to a critical point (a point representing a post-synaptic conductance configuration in Fig. 4.2 close to a sharp transition of the PV+BC ISI), a small decrease in the CCK+BC to PV+BC conductance induces a vast increase in the firing rate of the PV+BCs, even by 20 Hz. This supports the argument that a strong disinhibition of the PV+BCs, mediated by the CCK+BCs at the peak of the theta burst, can induce a sudden increase in the PV+BC firing rate and mediate the sharp termination of the PYR population burst at the theta peak. Indeed, the individual PV+BCs in the full CA1 model fire at slow theta frequencies in accordance to the ongoing LFP theta rhythm. If the dynamics follow those of our grid search (Fig. 4.2) of the segment model, then a strong inhibition of the CCK+BCs would effectively release the PV+BCs from the CCK+BC inhibition causing a sudden increase in the firing rate of the PV+BC. The four steps of the theta burst termination are also shown in the histogram of Fig. 5.2.

5.3.3 The gamma rhythm and the theta/gamma PAC

Along with the theta rhythm, a gamma rhythm is also present in the LFP exhibiting PAC with the theta rhythm. This slow gamma rhythm is produced by the gamma-paced entrainment of the noisy-firing PYR cells as follows. The PV+BCs, the AACs and the CCK+BCs are gamma-bursting cell types that organize into coherently firing populations likely via an ING mechanism (see Background). The PV+BCs, the AACs and the CCK+BCs also form strong connections with the PYR cells. As a result, during a theta cycle, (for example the one spanning from 3800 to 3900 ms in Fig. 5.1B), these gamma-firing cells periodically inhibit the noisy firing PYR cells forcing them to burst in a gamma-paced manner. This results in a slow gamma rhythm, progressively maximizing in amplitude as the recruitment of the PYR cells increases towards the peak of the theta cycle. This PYR cell gamma rhythm is conceptually similar to a PING mechanism (see Background). Because the amplitude of the slow gamma LFP maximizes at peak of the PYR cell theta burst (which corresponds to the peak of the theta cycle), the amplitude of the gamma rhythm is coupled with the phase of theta, giving rise to the phenomenon of theta/gamma PAC.

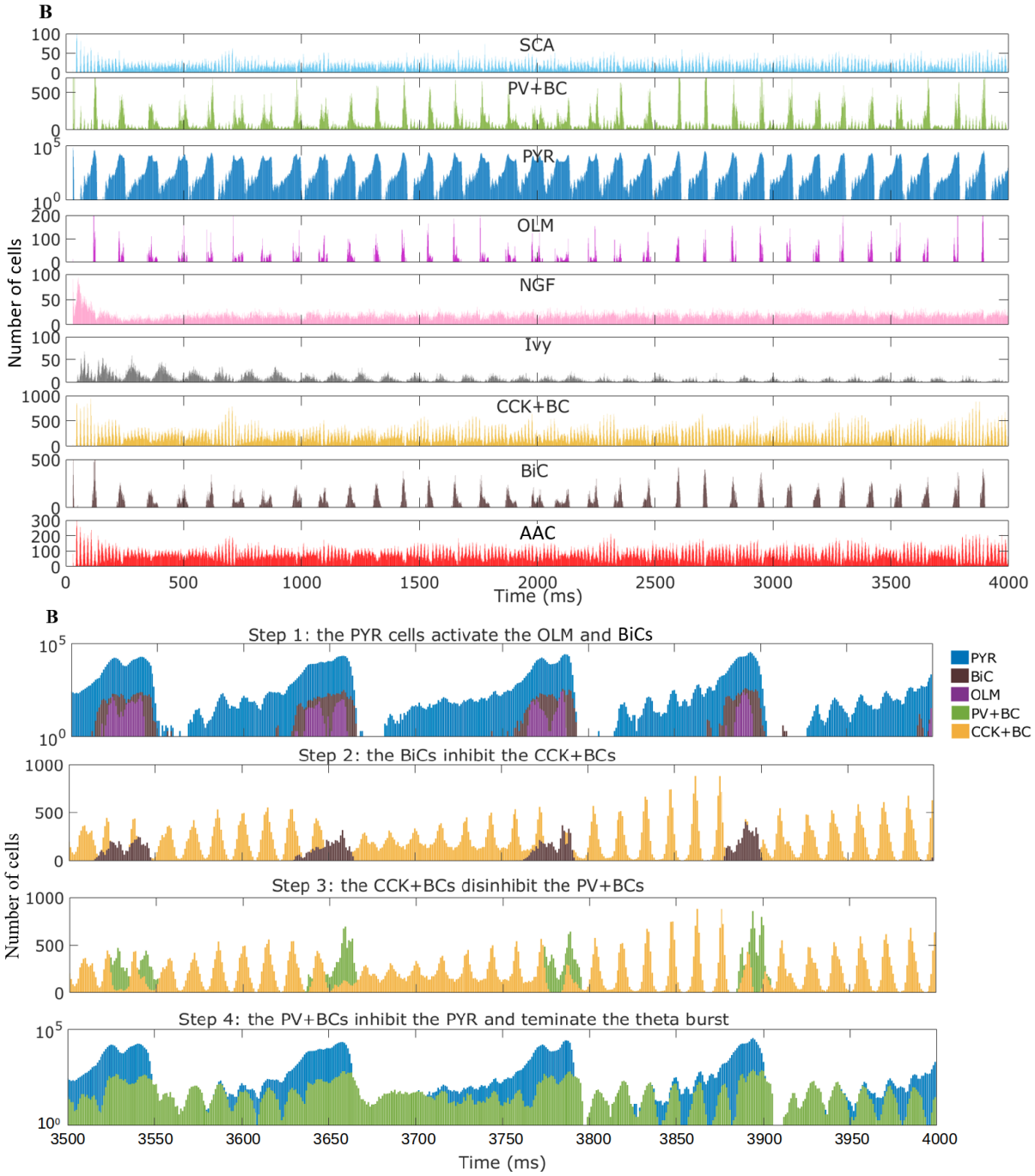

Figure 5.2: The termination of the theta burst is mediated by a sequential activation of inhibitory cells. **A**. Histogram plots of the eight inhibitory cell types and the PYR cells in the original full CA1 model. **B**. The termination of the theta burst is mediated by a sequential activation of inhibitory cells according to 4 steps as described in the main text. The last 500 ms of the histogram in **A**. are shown.

5.4 Summary and conclusions

5.4.1 How this mechanism advances our understanding of theta generation

In this Chapter, we presented a comprehensive explanation of the theta mechanism which relies upon preceding analysis of the segment model. We showed that the theta rhythm generation is mediated by the PYR cells, but the termination of the theta bursts is an inhibition-mediated mechanism which contributes to the robustness and stability of the rhythm.

In their original study [14], Bezaire and colleges mentioned that the PYR cells preferentially discharge at the trough of the LFP analog, strongly recruiting especially the PV+ basket and BiCs, which in turn cause a silencing of the PYR cells for about the first third of the rising half (i.e., from 0 to about 60 degrees) of the LFP analog theta cycle, but the exact sequence of events that lead to the termination of the theta burst were not parsed out. Bezaire and colleagues also addressed how the PYR cell collaterals reinforce the progressive recruitment of the PYR cells and amplify the PYR cells firing towards the peak of the theta cycle, but the prominent role of the PYR cells as theta rhythms initiators was first demonstrated and discussed in this thesis and in our submitted work [34].

Although the theta mechanism wasn't extensively formulated and only premature steps were taken in that direction, in [14] Bezaire and colleges implemented perturbations to examine which cell types are important for theta rhythms. In Fig. 5.3 colored are the cell types that were deemed important in [14], as muting them would abolish the rhythm. Among them were the BiCs, PYR cells, PV+BCs, CCK+BCs, which are part of the mechanism described in this Chapter and thus it is expected that removing any of these cell types would abolish theta. As the AACs form strong connections with the PYR cells it is likely that they contribute to the termination of the theta burst along with the PV+BCs. The NGF cells are noisy firing cells and it is not clear why eliminating them from the network would abolish theta. However, it is possible that they contribute to the net current driving the PYR cells and thus removing them would have an effect of on the frequency of the LFP output. Indeed, a closer inspection of the network output after the removal of NGF cells in [14] suggests that removing these cells increases the frequency of the network rhythm driving them out of the theta range (these results are posted on `https://crcns.org/data-sets/sim/sim-1`).

While the theta mechanism presented in this study is based on the specific connec-

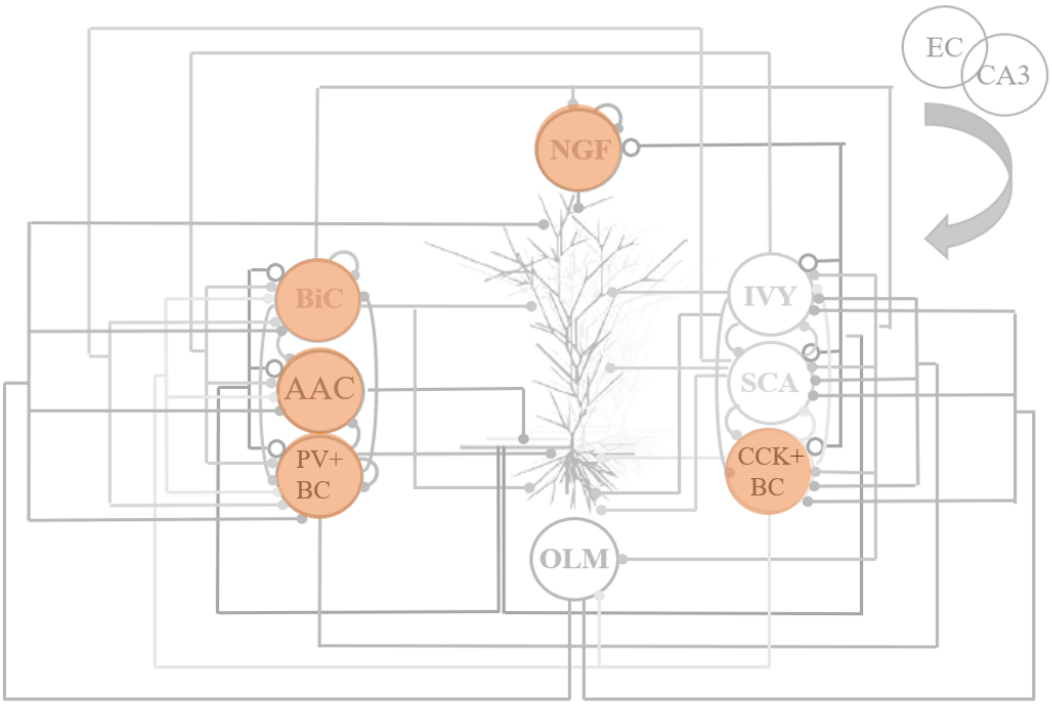

Figure 5.3: Inhibitory cell types important for theta rhythms. Muting each cell type's output caused a range of effects in [14]. Highlightened in orange are the cell population whose mutation from the network abolished theta in [14].

tivity of the network, the relative strength of connections between inhibitory populations evidently changes across the septotemporal axis of the CA1 and across layers [151, 121]. The mechanism we propose in this Chapter supports alternative steps of inhibitory cell activation under the same general framework, as follows:

- **Step 1.** The PYR cells set the clock of the theta rhythm. The frequency of the rhythm is defined by the net input the PYR cells receive.
- **Step 2.** Firing of the PYR cells maximizes at the theta peak activating the theta-firing inhibitory cells (BiCs and OLM cells.)
- **Step 3.** Activation of the theta-firing cells inhibits a group of gamma bursting cells (mainly PV+BCs, CCK+BCs but also AACs).
- **Step 4.** The PV+BCs, CCK+BCs form strong connections with each other, and thus strong activation of one population inhibits the other. Here we showed that CCK+BCs silencing due to BiCs activation dis-inhibits the PV+BCs. In principle, if the connectivity allows an alternative path could take place. If OLM to PV+BC connections were sufficiently strong, then strong recruitment of the OLM cells could silence the PV+BCs and as a result dis-inhibit the CCK+BCs. Activation of CCK+BCs would then lead to the termination of the PYR cell burst so long as the connectivity between the two populations was appropriate. In fact, recent studies [121] have shown that in CA1, PV+BCs preferentially innervate PYR cells at the deep sublayers while CCK+BCs are more likely to target the superficial PYR cells. Interestingly, the same study predicted different innervation of PYR cells by BiCs and OLM cells in deep versus superficial PYR cells, which could support the existence of the alternative mechanism of theta burst termination we just described.

Chapter 6

Deciphering the Contribution of SOM+ Cells to Intrinsic Theta Rhythms Using Biophysical LFP Models

Both me and Dr. Skinner conceptualized and designed the project and wrote the paper. The results presented in this Chapter (simulations and analysis) were done by me.

The work presented in this Chapter has been published in:

Chatzikalymniou, Alexandra P., and Frances K. Skinner. "Deciphering the Contribution of Oriens-Lacunosum/Moleculare (OLM) Cells to Intrinsic θ Rhythms Using Biophysical Local Field Potential (LFP) Models." ENeuro 5, no. 4 (July 1, 2018). `https://doi.org/10.1523/ENEURO.0146-18.2018`.

6.1 Preamble

In the previous Chapter we showed how the termination of the PYR cell theta burst is mediated by the sequential activation of the BiCs, the CCK+BCs and the PV+BCs. Another class of inhibitory cells, the OLM cell has been prominently involved in theta rhythms and its reported role in literature has remained unclear (see Background). With respect to the whole hippocampus preparation, recent studies [2] provided clear evidence that the OLM cells don't contribute to the power of intrinsic theta rhythms. Similarly,

in their modelling study [14], Bezaire and colleagues found that removing the OLM cells from the full CA1 network doesn't influence theta power. As such, it's becoming more and more established that the OLM cells don't affect theta rhythms as originally thought. However the effect that OLM cells may exert on theta activities is a complex one. These cells target the distal dendrites of the PYR cells and can exert an indirect effect by disinhibiting the middle dendrites. In this Chapter, we take advantage of experimental recordings of SOM+ cells, the majority of which are OLM cells, from the intact preparation to shed light on the contributions of this ambivalent cell type to ongoing theta rhythms.

6.2 Introduction

Given the reduced nature of the whole hippocampus *in vitro* preparation [67], this system presents an opportunity to understand cellular contributions to LFP theta rhythms by removing several complicating pathways that exist in *in vivo* scenarios. Ambiguities are greatly reduced and our ability to understand cellular contributions to LFP recordings is greatly enhanced. OLM cells are a major class of GABAergic interneurons [106]. They play an important role in gating information flow in the hippocampus by facilitating intrahippocampal transmission from CA3 while reducing the influence of EC inputs [96]. Since OLM cells project to the distal dendrites of PYR cells they would be expected to generate large LFP deflections due to large dipole moments [129]. However, these expectations may need to be modified since in addition to inhibiting distal layers they can have an effect on inner and middle layers, by inhibiting interneurons that target PYR cells at those layers [96].

In this Chapter, we use computational modeling to determine the contribution of OLM cells to ongoing intrinsic LFP theta rhythms, considering their interactions with local targets, in the context of the *in vitro* whole hippocampus preparation. We take advantage of a previous modeling framework of inhibitory networks [55], and generate biophysical LFP models to investigate the factors that influence theta LFP characteristics. By directly comparing our LFP models with experiment, we constrain the required connectivity profile between OLM cells and other inhibitory cells types, and we show that OLM cells control the robustness, but not the power, of intrinsic LFP theta rhythm polarity profile. We also assess the spatial reach of the extracellular signal and estimate the number of cells that contribute to it. The many complex interactions lead to emergent LFP output that is non-intuitive, and would not be possible to decipher without biophysical LFP modeling in an experimentally constrained microcircuit context. As

such, our work shows a way forward to obtain an understanding of cellular contributions to brain rhythms.

6.2.1 Intrinsic theta rhythms in the hippocampus and the role of OLM cells

To examine the role of specific hippocampal interneurons in the intrinsic theta rhythms, Amilhon and colleagues [2] optogenetically activated and silenced PV+ or SOM+ interneurons. PV+ cell types exhibiting fast firing characteristics include BCs, AACs and BiCs [9]. OLM cells are SOM+ but it is not the case that SOM+ interneurons are necessarily OLM cells. However, reconstructions of SOM+ cells during intrinsic theta rhythms, confirmed that they were likely OLM cells [79]. Amilhon and colleagues [2] later found that optogenetic manipulation of SOM+ cells modestly influenced the intrinsic theta rhythms. In contrast, activation or silencing of PV+ cells strongly affected theta. These results thus demonstrated an important role for PV+ cells but not SOM+ cells for the emergence and presence of intrinsic hippocampal theta, as given by the LFP recordings.

LFP recordings in this preparation have a particular sink and source distribution across the different layers [67]. It is given by a single dipole characterized by positive deflections in SLM and SR and negative deflections in SP and SO. The dipole is illustrated in Fig. 6.1A. This LFP laminar polarity profile has been found to be consistent across preparations [67]. We note that since theta rhythms persist even when the CA3 region is removed, excitatory collaterals from the CA3 do not seem to be a necessity for the emergence of theta rhythms and the sink/source density profile. Thus, in our LFP model in this work, we assume that excitatory input to CA1 PYR cells is restricted to the basal dendrites due to CA1 PYR cell collaterals [67].

6.2.2 Using a previous network model framework as a basis

To understand how the complex interactions between different inhibitory cell types contribute to theta LFP rhythms, we use a previously developed computational network framework representing a CA1 microcircuitry [55]. Given the newly discovered connections between OLM cells and BiCs [96], this network model was developed to explore how OLM-BiC interactions influence the characteristics of theta rhythms. The model contained PV+ fast-firing [57] and OLM cell models [55], previously developed based on recordings from the whole hippocampus preparation. Because of distal contacts of OLM cells with PYR cells, a multi-compartment PYR cell model was used to incorporate in-

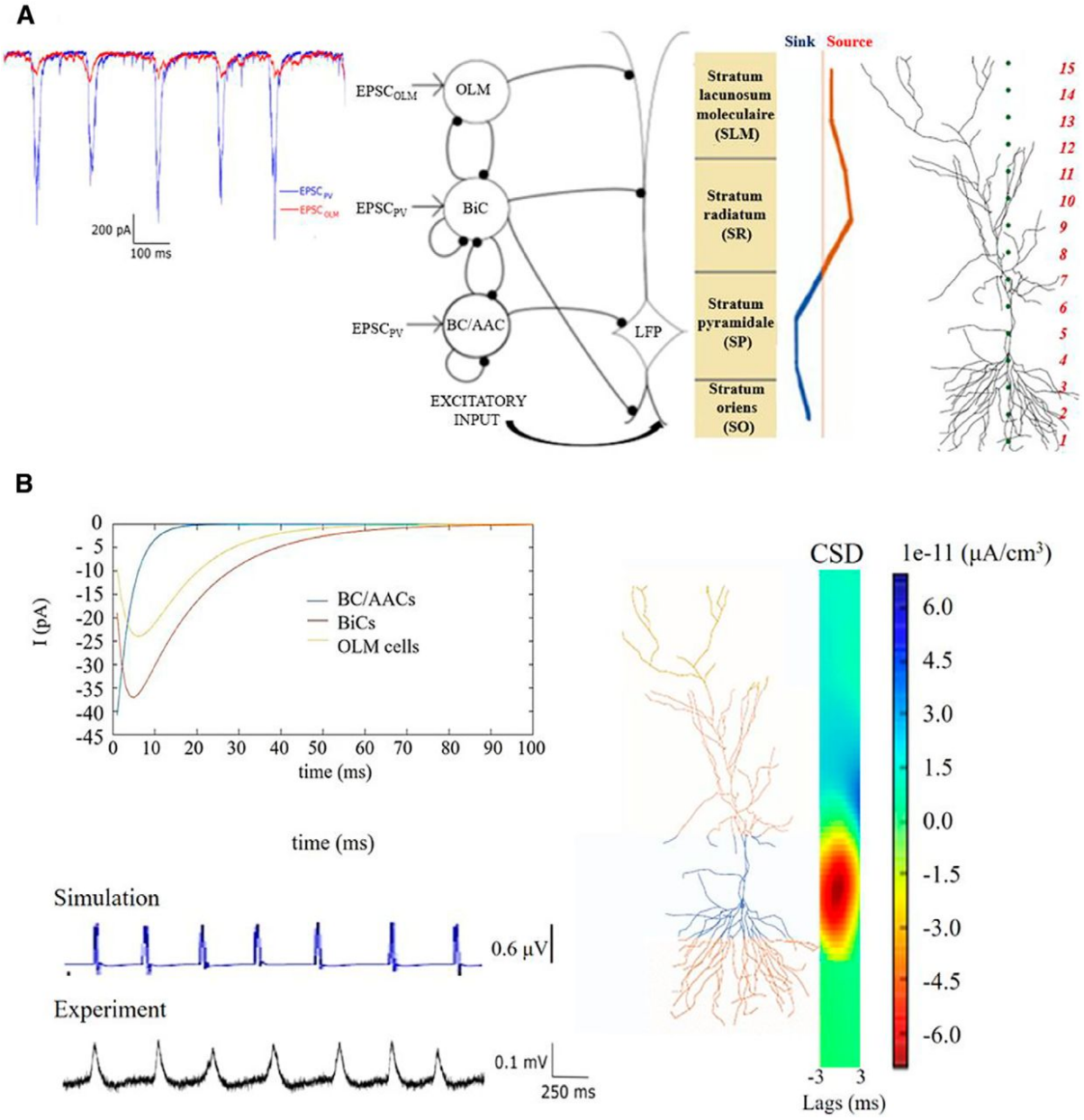
A
EPSC_PV
EPSC_OLM
200 pA
100 ms
EPSC_OLM
OLM
EPSC_PV
BiC
EPSC_PV
BC/AAC
LFP
EXCITATORY INPUT
Stratum lacunosum moleculaire (SLM)
Stratum radiatum (SR)
Stratum pyramidale (SP)
Stratum oriens (SO)
Sink
Source
15
14
13
12
11
10
9
8
7
6
5
4
3
2
1
B
I (pA)
0
- 5
-10
-15
-20
-25
-30
-35
-40
-45
0 10 20 30 40 50 60 70 80 90 100
time (ms)
BC/AACs
BiCs
OLM cells
time (ms)
Simulation
0.6 µV
Experiment
0.1 mV
250 ms
CSD
1e-11 (µA/cm³)
6.0
4.5
3.0
1.5
0.0
-1.5
-3.0
-4.5
-6.0
-3 3
Lags (ms)

Figure 6.1: Model setup and experimental essence. A. A schematic of the network model used by [55] is shown in the middle. The network model contains single compartment representations for OLM cells, BiCs, and BC/AACs. Inhibitory synapses are represented by filled black circles. Each inhibitory cell receives EPSCs that is taken from experimental intracellular recordings as shown on the far left (adapted from [55]). Each inhibitory cell synapses onto the PYR cell model as schematized. There are 350 OLM cells, 120 BiCs and 380 BC/AACs. Basal excitatory input is included. An illustration of the laminar polarity profile (source/sink distribution) estimated from LFP experimental recordings is shown on the right, and the detailed PYR cell morphology that is used along with the 15 equidistant electrode locations in the different layers is shown as red numbers on the far right. **B**. IPSCs from the different cell types (colored as indicated) are shown on the left to show their different kinetics. Parameter values are given in Table 6.1, and the same coloring is used on the detailed PYR cell morphology to indicate the synaptic location regions for the different cell types. An example simulation of a computed LFP from the SR layer (using parameter values of g_{sb}=6 and g_{bs}=1.25 nS, c_{sb}=0.21) is shown below, and the computed current source density (CSD) is shown on the right (averaged over time). On the bottom is an example of an experimental LFP recording from the SR layer (adapted from [55]).

puts across the dendritic tree. The network model framework is shown in Fig. 6.1A and a summary of the network model is provided in the Methods. We note that this model was designed to explore cellular interactions and contributions to the ongoing intrinsic theta rhythms, and not to the generation of the theta rhythms explicitly.

As schematized in Fig. 6.1A, the inhibitory cell populations encompassed BC/AACs, BiCs and OLM cells that were driven by experimentally-derived EPSCs. These EPSCs were recorded during an ongoing rhythm and were of theta frequency (see Fig. 6.1A). Spiking output from the inhibitory cell populations led to IPSCs on the PYR cell. They were distributed on the PYR cell according to where the particular cell population targeted. Thus, BC/AAC IPSCs targeted somatic regions, BiC IPSCs targeted middle apical and basal regions and OLM cell IPSCs targeted distal apical regions. IPSCs generated by the different cell types are shown in Fig. 6.1B (see Methods for details). The spatial integration of the inhibitory postsynaptic potentials at the soma of a passive PYR cell model was used as a simplistic LFP representation [55]. This representation was in fact indicative of the intracellular somatic potential rather than the extracellular one, but it did allow the distal OLM cell inputs relative to more proximal PV+ cell inputs to be taken into consideration. Using this computational model framework, multiple simulations were performed and it was shown that there were parameter balances where OLM cells did or did not affect theta power [55], depending on whether compensatory effects with BiCs occurred as a result of the synaptic interactions between these cell types. Thus,

the size and strength of synaptic interactions between OLM cells and BiCs seemed to be an important aspect for the presence of intrinsic LFP theta rhythms. However, since an ad-hoc LFP representation was used, it was not possible to do any direct comparisons with experimentally recorded LFPs.

In the work presented in this Chapter, we build on this model framework and we develop biophysical LFP models. An example of the intrinsic LFP rhythm is shown in Fig. 6.1B. We use these models to decipher the complex contributions of OLM cells to ongoing theta rhythms. We use the inhibitory spiking output generated in [55] as a basis for generating biophysical LFPs, and the same PYR cell model. However, unlike the previous work, we use the framework of volume conductor theory (see Methods) and generate actual extracellular potential output as a result of the overall activity of the inhibitory cell firings across the CA1 layers. In addition, we include excitatory inputs onto the basal dendrites to represent recurrent CA1 inputs (see schematic in Fig. 6.1A and Methods for details), and directly compare with characteristics of experimental LFP recordings.

6.3 Methods

6.3.1 Network model details

This work builds on previously developed models described in [55]. Here we provide a summary of specifics that are salient to the present study.

Inhibitory cell types and numbers, PYR cell model: The inhibitory network model consists of 850 cells and represents a volume of 1 mm^3 as shown to be appropriate to obtain spontaneous theta rhythms in the *in vitro* whole hippocampus preparation [55, 57, 67]. Four different types of inhibitory cells are included: BCs/AACs, BiCs and OLM cells. BCs/ AACs comprise a 380-cell population and target somatic, perisomatic and axo-axonic regions of PYR cells. The BiCs comprise a 120-cell population and target middle, apical and basal regions of PYR cells. Finally the OLM cells comprise a 350-cell population and target the distal, apical dendrites of PYR cells. As in [55], the structure of the PYR cell model was based on the one used in [116] as implemented in the NEURON Simulator [33] (see ModelDB Accession number 144541). The PYR cell model was used as a passive integrator of inputs from cell firings at the various layers of the hippocampus, and all active, voltage-gated channel conductances were set to zero. This overall network model is schematized in Fig 6.1A. With the exception of basal excitatory input, it is the same as used in [55].

Inhibitory cell models and drives: The inhibitory cell models are single compartment, they have an Izhikevich mathematical structure [82] and are constructed by fitting to experimental data from whole cell patch clamp recordings in the whole hippocampus preparation [55]. All of the cell model parameter values are given in [55]. PV+ cell types are the BCs/AACs, the BiCs and the SOM+ cells which are OLM cells. Each cell model is driven by excitatory postsynaptic currents (EPSCs) taken directly from experiment [79] during ongoing spontaneous theta rhythms for PV+ or SOM+ cells. The EPSCs were designed to ensure that the inhibitory cells receive frequency-matched current inputs and at the same time have amplitudes and peak alignments that were consistent with theta oscillations in experiment [55] - see EPSC_{PV} and EPSC_{OLM} examples in Fig 6.1A. Importantly, the experimental variability in amplitude and timing of EPSCs across cells was captured by varying the gain (factor by which the EPSC was scaled to alter the amplitude) and timing of the EPSCs across cells with a normal distribution in accordance with the experimental recordings. Thus, each inhibitory cell model received a unique set of excitatory synaptic inputs reflecting the range of amplitudes and timing of those recorded experimentally.

Inhibitory network connectivity and output: PV+ cells (BCs/AACs and BiCs) were randomly connected with probabilities and synaptic conductance values based on experimental estimates from the literature and previous modeling work [57]. Connections between BiCs and OLM cells are known to exist [96] and a range of values from the literature was previously estimated, with the connection probability from BiCs to OLM cells taken as 0.64 times the connection probability from OLM cells to BiCs [55]. Although OLM-BiC connections exist, their synaptic conductance values are unclear but can be roughly estimated from the literature. In previous work, the balance of parameter values important for theta rhythms was specifically examined by exploring a wide range of values that encompassed determined estimates [55]. Inhibitory synapses were modeled using a first order kinetic process with appropriate rise and decay time constants. The spiking output of the inhibitory network models briefly described here, were computed for the range of synaptic conductance strengths and connection probabilities given in Table 6.1. For the work in this paper we use output from these inhibitory networks. Specifically, our simulations last 5 seconds; the connection probability from OLM cells to BiCs (c_{sb}) varied from 0.01 to 0.33 with a step size of 0.02 producing 16 sets of connection probabilities; synaptic conductance values ranged from 0-6 nS for OLM cells to BiCs (g_{sb}) and for BiCs to OLM cells (g_{bs}). By changing g_{sb} and g_{bs} with a step size resolution of 0.25 nS, 625 raster plots were produced. So the total number of raster plots

Table 6.1: Connectivity parameter values.

Cell Type X to Cell Type Y (X – Y)	Connection Probability	Maximal Synaptic Conduc.(nS) or Synaptic Weight (μS) to PYR cell	Synaptic Rise Time (ms)	Synaptic Decay Time (ms)
BC/AAC – BC/AAC	0.12	3	0.27	1.7
BC/AAC – BiC	0.12	3	0.27	1.7
BC/AAC – OLM cell	0	N/A	N/A	N/A
BC/AAC – PYR cell	1	0.00038	0.3	3.5
BiC – BC/AAC	0.12	3	0.27	1.7
BiC – BiC	0.12	3	0.27	1.7
BiC – OLM cell	0-0.224	0-6	2	16.1
BiC – PYR cell	1	0.00044	2	16.1
OLM cell – BC/AAC	0	N/A	N/A	N/A
OLM cell – BiC	0-0.33	0-6	2	16.1
OLM cell – OLM cell	0	N/A	N/A	N/A
OLM cell – PYR cell	1	0.00067	3.5	11.8
Excitatory Input to PYR cell (197 contacts to basal tree)	1	0.00044	0.5	3

N/A = not applicable

in our study as computed in [55] is (625 × 16) 10,000, and they are all available on Open Science Framework (osf.io/vw3jh).

Synaptic weights and distribution onto the PYR cell Inhibitory inputs to the PYR cell model are distributed in the same way as done in [55]. That is, we distinguish between synapses at the distal layer (SLM), medial and basal layers (SR and SO), and the perisomatic/somatic layer (SP). Distal synapses are defined as those that are $> 475\mu$m from the soma; apical and basal synapses are defined as those that are $> 50 - 375\mu$m from the soma; perisomatic/somatic synapses are defined as those that are $< 30\mu$m from the soma. We created three lists of components (where each component points to a specific segment of a section in the PYR cell model), for the possible distal, proximal apical/basal, and perisomatic/somatic synaptic targets. For each individual, presynaptic inhibitory cell model, we randomly chose a synaptic location on the passive CA1 PYR cell model from the respective list (distal dendrites for OLM cell models, apical/basal dendrites for BiC models, and perisomatic/somatic locations for BCs/AACs). Then the

spike times from the individual, inhibitory cell models filled a vector, and an artificial spiking cell was defined to generate spike events at the times stored in that vector at the specific location at which that cell created a synaptic target. We used the Exp2Syn function in NEURON to define the synaptic kinetic scheme of the synapse. This function defines a synapse as a synaptic event with exponential rise and decay, that is triggered by presynaptic spikes, and has a specific weight that determines its synaptic strength, and an inhibitory reversal potential of -85 mV, as measured in the whole hippocampus preparation. Synaptic weight values onto the PYR cell from the different cell populations are estimated using somatic IPSCs values for OLM cells onto PYR cells [107]. As these synaptic weights were not clearly known, we used different synaptic weight profiles in the explorations as was been done previously [55]. The main profile used was graded such that the different cell types lead to similar somatic IPSCs amplitudes, considering that 0.00067 μS can be estimated from the OLM cells IPSCs currents (see Table 6.1). Several other synaptic weight profiles were examined. Finally, we note that an ad-hoc representation for LFPs was previously used [55] as given by an inverted summation of all integrated inputs as measured at the PYR cell soma. That is, the postsynaptic potentials on the PYR cell are due to the various inhibitory cell firings that comprised the presynaptic spike populations.

6.3.2 Additional network model details for this study

For the study, inhibitory inputs are distributed in the same way as in [55]. In [55] the literature was used to estimate synaptic conductances between OLM cells and BiCs as 3-4 nS, and [14] used 10 synapses/connection as estimates in their detailed data-driven computational models. This implies that a single synapse would be 0.3-0.4 nS, representing an approximate minimum connection weight.

As we make direct comparisons with theta LFPs experimental recordings, it is important to include excitatory input to the PYR cell model. Thus we also include excitation due to CA1 recurrent collaterals which synapse on basal dendrites [161]. In [55] excitatory feedback was not included in a direct fashion as the focus was on ongoing theta rhythms and OLM-BiC interactions, and not on theta generation mechanisms explicitly. Thus, model excitatory cell populations were not specifically modelled. This means that we did not have explicit spike rasters for excitatory populations as we did for the inhibitory cell populations. Rather than generate an arbitrary set of spike times to simulate excitatory inputs, we use spike times from a BiC raster (g_{sb}=3.75, g_{bs}=1.75 nS, c_{sb}=0.21) in which the neuron order was randomized, and with comparable synaptic weights. Using these

random spike trains we generate spike vectors exactly as in the case of interneurons and randomly distribute them on basal dendrites using 197 synapses based on number estimates from [15] and [14]. In this way, we do not have a spatiotemporal dominance of inhibitory or excitatory input in basal dendrites. We use an excitatory reversal potential of -15 mV as measured in the whole hippocampus preparation, and synaptic time constants in line with modeling work [53]. In essence, we simulate EPSCs using random spike trains of theta frequency instead of explicitly modeling PYR cell spiking activity. We note that with these choices, somatically recorded currents in our PYR cell models are similar to what is observed in experiments [79]. All parameter values are summarized in Table 6.1.

We note that the inhibitory cell spike rasters computed in [55] used random connectivities between the different inhibitory cell populations. Consider that a given set of parameters (c_{sb}, g_{sb}, g_{bs}) defines a connectivity map. Each cell within a given population is randomly assigned a synaptic location within the boundaries of the dendritic tree on which it projects. Based on a given connectivity map the spiking activity of the various cell populations will differ. Therefore the characteristics of the produced biophysical LFPs will depend on the spike distribution of a given population defined by the connectivity map and also the number and location of synapses on the dendritic tree. To ensure that our LFP output is not dependent on the specific synaptic location that every cell is assigned to, we generalize our observations by performing many trials for a given connectivity map, assigning randomly different location to the cells of each population to ensure that the LFPs output is not dependent on that aspect.

6.3.3 Biophysical computation of LFPs

Extracellular potentials are generated by transmembrane currents [124]. In the commonly used volume conductor theory, also used here, the extracellular medium is modeled as a smooth three-dimensional continuum with transmembrane currents representing volume current sources. The fundamental formula [129] relating neural activity in an infinite volume conductor to the generation of the LFPs $\phi(r,t)$, at a position r is given by Eq. 2.16 of the Background, also repeated here for convenience:

$$\phi(r,t) = \frac{1}{4\pi\sigma} \sum_{k=1}^{n} \frac{I_k(t)}{|r - r_k|} \tag{6.1}$$

Here I_{k} denotes the transmembrane current (including the capacitive current) in a neural compartment k positioned at r_k, and the extracellular conductivity, here assumed real

(ohmic), isotropic (same in all directions) and homogeneous (same at all positions), is denoted by σ. In the hippocampus the mean extracellular conductivity σ is equal to 0.3S m^{-1} [104] which is the value that we used for our simulations. A key feature of Equation 6.1 is that it is linear, i.e., the contributions to the LFPs from the various compartments in a neuron sum up. Likewise the contributions from all the neurons in a population would add up linearly. The transmembrane currents I_k setting up the extracellular potentials according to Equation 6.1 were calculated by means of standard multi-compartment modeling techniques, here by use of the simulation tool NEURON [33]. The CSDs in Fig. 6.1B were computed using the 1D kCSD inverse method proposed in [131]. The CSDs were computed from the LFPs measured by electrodes that are arranged along a straight line, in this case along the cellular axis of the PYR cell.

The same PYR cell multi-compartment model as described above was used to compute the extracellular biophysical LFPs, and we used the set of 10,000 5-second raster plots (of inhibitory spikes) as described above for our presynaptic populations with the addition of basal excitation. That is, we generated extracellular potential traces (5 sec each) due to the various inhibitory cell firings. We used a single multi-compartment PYR cell to compute the biophysical LFPs. While an experimental LFPs is generated by many cells, we still referred to our extracellular output as an 'LFPs' for consistency with the computational literature, where the 'LFPs' term has been used for an extracellular field from single or multiple cells.

6.3.4 Simulation details

The computational simulations and analyses were performed using the LFPy python package [99], NEURON [33] and MATLAB [112]. The large scale network simulations were conducted using high-performance computing at SciNet [102]. The code/software described in the paper is freely available online at `https://github.com/FKSkinnerLab/LFP_microcircuit`.

6.4 Results

6.4.1 Overall characteristics of biophysical LFP models

From the previous modeling study of [55], several sets of inhibitory spiking output with particular connection probabilities and synaptic conductances between OLM cells and BiCs were available. The connection probability from OLM cells to BiCs (c_{sb}) varied from 0.01 to 0.33 with a step size of 0.02 producing 16 sets of connection probabilities;

synaptic conductance values ranged from 0-6 nS for OLM cells to BiCs (g_{sb}) and for BiCs to OLM cells (g_{bs}) with a step size of 0.25 nS. Thus, for a given connection probability, there were 625 sets of spiking outputs from inhibitory cells, where each set represented a 850-cell inhibitory network with particular synaptic conductances. We considered a set to be a connectivity map representing the inhibitory cell populations.

For each connectivity map, we generate a biophysical, extracellular LFP. A virtual electrode probe is placed along the vertical axis of the PYR cell model to record its LFP output in a layer dependent manner. This PYR cell model is the "processor" of the LFP signal as it integrated postsynaptic inputs from different presynaptic populations. We compute LFPs at 15 equidistant sites along a linear axis - see Fig. 6.1A. The PYR cell output corresponds to readouts of the postsynaptic activity elicited by the afferent inhibitory cell populations that targeted the PYR cell in appropriate regions, referred to as the LFP "generators". We note that although there was a single connectivity map representing the randomly connected inhibitory cell population, we performed several trials when randomly targeting the PYR cell to ensure the robustness of our results (see Methods). To achieve effective electroneutrality, the extracellular sink needed to be balanced by an extracellular source, that is, an opposing ionic flux from the intracellular to the extracellular space, along the neuron; this flux is termed the 'return current'.

We developed some initial intuition regarding the generation of our biophysical LFPs by computing them *without* including basal excitation. That way, all of the inputs received by the PYR cell model were inhibitory. Fig. 6.2A,B illustrates the process and shows some examples. Let us first focus on Fig. 6.2A(i). Next to each cell population in the network schematic are two examples of 1-second raster plots of spiking outputs (from the previously computed 5-second inhibitory network simulations in [55]), produced for particular parameter sets. These spikes gave rise to IPSCs on the PYR cell model and the computed extracellular LFP at the somatic layer is shown in Fig. 6.2A(ii). As shown, these particular parameter sets produced LFPs with positive or negative deflections. Let us next focus on Fig. 6.2B(i). One example of a 1-second raster plot is shown, and for this parameter set, the LFP only has a few positive deflections, as shown in Fig. 6.2B(ii). Assuming that one population burst in the raster plot leads to a single peak in the LFP, there would be about 29 peaks in the LFP for a 5-second simulation (i.e., about 5.8 Hz frequency) since our inhibitory cell raster plots have 28-29 population bursts. Note that the raster plots in Fig. 6.2B(i) were not very different from the examples shown in Fig. 6.2A(i). We computed LFPs at all layers as represented by the 15 virtual electrodes shown in Fig. 6.1A, for the 625 sets of inhibitory spiking outputs across g_{sb} and g_{bs} values at a particular connection probability c_{sb}. The colored plot in Fig. 6.2A(iii) shows the

polarity of the LFPs at the somatic layer, and the color plot in Fig. 6.2B(iii) shows the number of LFP peaks in the somatic layer. In Fig. 6.2C normalized spike numbers for all interneuron populations are shown.

As a first approximation, given the network model framework and previous work we can say the following about the LFPs: Those governed mainly by synaptic inputs and not return currents are characterized by narrow waveform shapes as the synaptic inputs from any particular interneuron population enter the PYR cell in a synchronized fashion. This is due to the rhythmic EPSCs driving the inhibitory cells, giving rise to coherently firing populations (see example raster plots). We note that the EPSCs that were used in the simulations were not designed to be perfectly synchronized but instead the measured experimental variability was included (see Methods). On the other hand, return currents constituted a summation of less synchronized exiting currents that originally entered the cell at different locations. Therefore, LFP deflections governed by return currents were generally wider. Further, we would expect that the LFP recorded from different layers would first and foremost be influenced by the interneurons that project to that region. We also note that the width of the LFP deflection would not only be influenced by the nature of the current (synaptic inputs or return currents) but also by the synaptic time constants defining the shape of the IPSCs. IPSCs for the different cell populations are shown in Fig. 6.1B where it can be seen that the IPSCs produced by OLM cells and BiCs are wider relative to the IPSCs from BC/AACs. Thus, we expected that positive LFP deflections would be recorded in locations where OLM cells, BiCs and BCs project, with wider LFPs for OLM cell projection locations, and that LFPs dominated by return currents would be recorded in locations where there are no direct inputs from interneurons. However, due to interactions between BiCs and OLM cells, this is not necessarily the case as return currents from distant interneuronal inputs can prevail in regions where other interneurons directly projected. In fact, interactions between OLM cells and BiCs can strongly modulate the relative balance between synaptic inputs and return currents, which in turn can strongly modulate the distribution of sinks and sources in the resulting LFP.

The two examples of LFP output at the somatic layer in Fig. 6.2A(ii) show one with narrow positive deflections and the other with wider negative deflections. This thus indicates that the BC/AAC inputs that synapse at the somatic layer dominate for the positive deflection LFP example whereas BiC and OLM cell inputs that synapse more distally dominate for the negative wider deflection LFP example. The example in Fig. 6.2B(ii) of LFP output at the somatic layer indicates that a loss of peaks can occur due to the superposition of synaptic inputs and return currents. Another “loss of peaks”

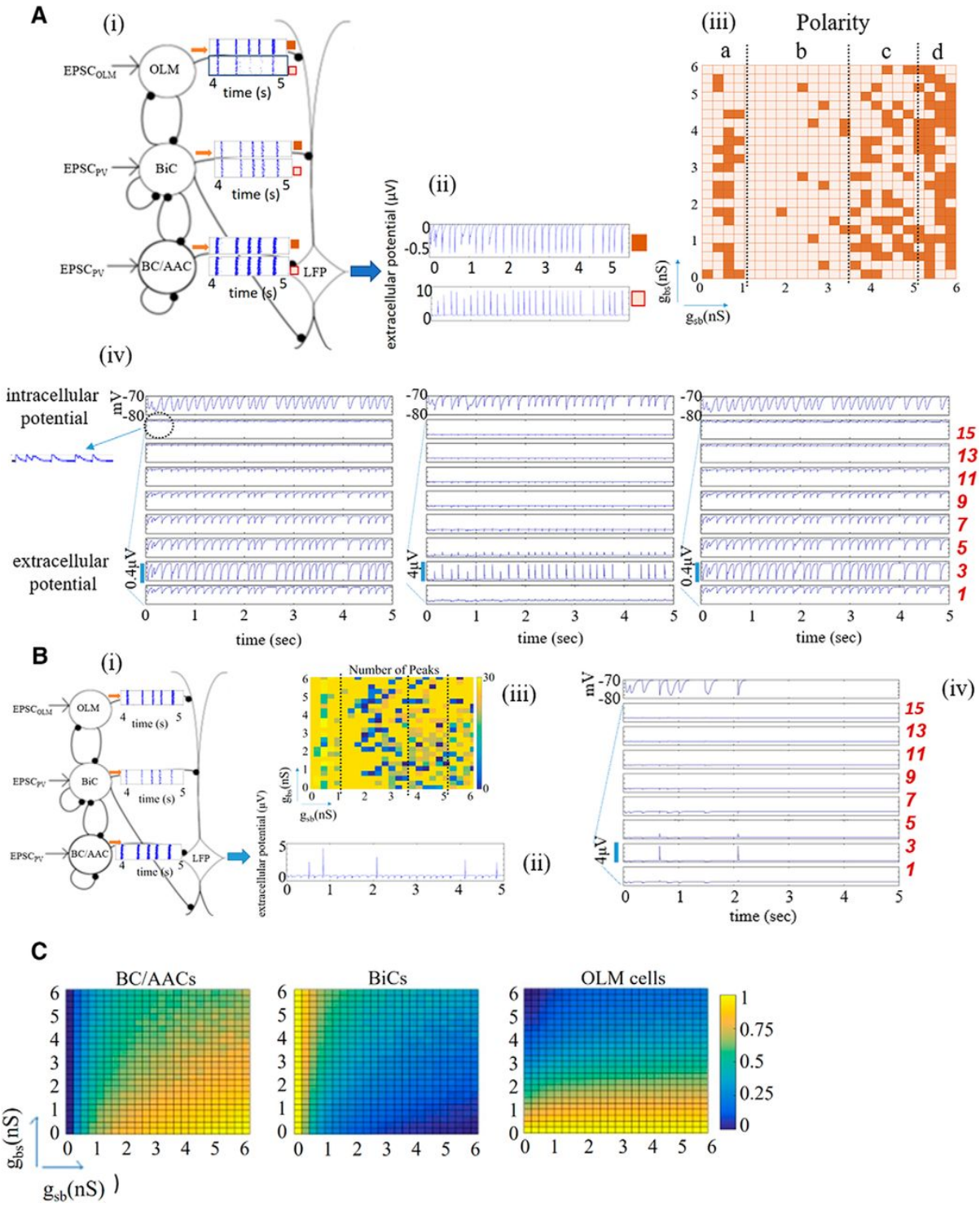
A
(i)
EPSC_OLM
OLM
EPSC_PV
BiC
EPSC_PV
BC/AAC
LFP
time (s)
(ii)
extracellular potential (μV)
(iii)
Polarity
a
b
c
d
g_bs(nS)
g_sb(nS)
(iv)
intracellular potential
mV
-70
-80
extracellular potential
0.4μV
4μV
time (sec)
15
13
11
9
7
5
3
1
B
(i)
(ii)
(iii)
Number of Peaks
(iv)
C
BC/AACs
BiCs
OLM cells
g_bs(nS)
g_sb(nS)
1
0.75
0.5
0.25
0

Figure 6.2: Biophysical LFP computation: features, examples and interneuron activities. A. (i) Schematic shows 2 raster plot examples for the given inhibitory cell population rasters. **(ii)** The resulting LFPs at the somatic layer, with positive and negative deflections is shown for the examples, labelled with dark- or light-colored squares. Parameter values are g_{sb}=1.5, g_{bs}=5.5 nS for positive and g_{sb}=0.5, g_{bs}=0.75 nS for negative deflections. **(iii)** The color plot on the right shows the polarity at the somatic layer, SP, electrode 4. Dotted lines delineate 4 regions labelled as a, b, c, d. Negative polarity: dark-colored squares, positive polarity: light-colored squares. **(iv)** LFP output for all layers are shown for 3 examples where the polarity is negative, positive and negative at electrode 3 (left to right). Parameter values are (left to right): g_{sb}=0.5, g_{bs}=0.75; g_{sb}=1.5, g_{bs}=5.5; g_{sb}=5.75, g_{bs}=0.75 nS. Inset shows a blow up of LFP output at electrode 13 (SLM) to show positive deflections. Also shown is the intracellular somatic potential of the PYR cell. No basal excitation is present, c_{sb}=0.21. **B. (i)** Schematic includes 1 raster plot example. **(ii)** The resulting LFP output at SP has 5 peaks. A maximum of 29 peaks is possible (see text). Parameter values are g_{sb}=2, g_{bs}=0.75 nS. **(iii)** The color plot shows the number of peaks that appear in the 5-second LFP computation at SP, electrode 4. Dotted lines delineate the same regions as in A. **(iv)** An example of LFP output for all layers as well as the intracellular somatic output which also shows a loss of peaks. Parameter values are g_{sb}=2.25, g_{bs}=5.0 nS. No basal excitation is present, c_{sb}=0.21. **C.** Interneuron activity for each interneuron population, normalized such that the number of spikes for a given pair of synaptic conductances is divided by the maximal number considering all pairs of synaptic conductances. Maximal number (5-second trace): 16,327 (BC/AACs), 6,808 (OLM cells), 4,589 (BiCs).

example is shown in Fig. 6.2B(iv), and LFP output from multiple layers in addition to the intracellular somatic output. For this example, the peak loss was also partially reflected in the intracellular somatic output. However, loss of peaks in the LFP output is not necessarily reflected in the somatic intracellular recording. Note that since the PYR cell only receives inhibitory input in these set of simulations, somatic intracellular potentials always have negative deflections. How the extracellular potential features change as a function of the synaptic conductances between BiCs and OLM cells is summarized in the color plots of Fig. 6.2A(iii) for the polarity and Fig. 6.2B(iii) for the number of peaks (somatic layer).

Let us consider Fig. 6.2A(iii). In this Figure, we can approximately distinguish four regions as g_{sb} increases. These regions are separated by dotted lines in Fig. 6.2A(iii), labelled a to d. For small g_{sb} values (0-1 nS, region a) the amount of inhibition that the BiCs receive from the OLM cells is minimized allowing the BiCs to be at the peak of their activity (see Fig. 6.2C). Consequently, the inhibition that the OLM cells and BC/AACs receive from the BiCs is maximized causing their activities to be minimized (see Fig. 6.2C). As a result, the extracellular potential in the somatic region is governed by return currents leading to negative polarity LFPs in the somatic layer (i.e., mainly dark-colored in region a of Fig. 6.2A(iii)), primarily due to the BiC synaptic inputs on the 'middle' region (SR layer) and 'basal' region (SO layer) of the PYR cell. As we increase g_{sb} (1-3.5 nS, region b), we encounter mainly positive LFP polarity (i.e., light-colored in region b of Fig. 6.2A(iii)). In region b, the inhibition onto the BiCs is increased and thus their activity is decreased, as can be seen in Fig. 6.2C, causing a decrease in the amount of the inhibitory current onto the PYR cell from BiCs. As a result, the magnitude of the return currents caused by the BiC synaptic inputs is decreased at the somatic layer. Simultaneously their ability to inhibit the BC/AACs is also decreased so that the BC/AACs became more active and their direct inhibition onto the PYR cell also increases. Since both BiCs and OLM cells activity is low in region b while BC/AAC activity is increased, the somatic LFP is governed by BC/AAC inputs rendering the extracellular LFP positive. As we further increase g_{sb} (3.5-5 nS, region c) the silencing of the BiCs increases even further and their ability to silence the BC/AACs is further reduced. Simultaneously OLM cell activity increases. Thus, the somatic LFP is influenced by direct synaptic inputs from BC/AACs and also return currents from OLM cells (sparse dark-coloring region c). Interestingly, the majority of the "loss of peaks" in somatic LFP output occurs in regions b and c (see blue-green pixels in the Fig. 6.2B(iii)) where superposition of synaptic inputs and return currents is mostly present. That is, current cancellations in certain cases lead to the abolishment

of the entire rhythm. Finally, for g_{sb} from 5.0-6 nS (region *d*), the BiCs are maximally inhibited and BC/AACs are at the peak of their activity. While we might have expected domination from the BC/AAC synaptic inputs for these values, it turns out that return currents (negative polarity) dominate. This can be explained by the increased activity of OLM cells which are also at the peak of their activity producing strong return currents in the somatic region. In summary, light-colored regions in Fig. 6.2A(iii) signify that BC/AACs dominate the extracellular somatic potential and dark-colored regions signify that other inhibitory cell types (BiCs or OLM cells, or both) contribute more strongly.

In Fig. 6.2A(iv), we show three examples of LFP recordings at multiple layers as well as the somatic intracellular potential, for increasing values of g_{sb} from left to right. To allow an appreciation of the changing magnitude of the signal, we use the same resolution on the ordinate axis for all LFP plots shown. On the left (g_{sb}=0.5 nS) we see that the signal is governed by return currents (negative polarity) in the entire SP (electrodes 3 and 5), in SO (electrode 1) and in SR (electrodes 7,9 and 11). Synaptic events govern SLM (electrodes 13 and 15) where OLM cells directly project, leading to positive polarity. In the middle (g_{sb}=1.5 nS), the LFP in SP and SO are governed by synaptic inputs (positive polarity), and in SR and SLM by return currents (negative polarity). As expected, we find that the positive polarity LFP in SP is narrower relative to the positive polarity LFP in SLM on the left, because the IPSCs produced by OLM cells are wider relative to those of BC/AACs, as shown in Fig. 6.1B. On the right where g_{sb}=5.75 nS, we observe a similar trend as for the example on the left where g_{sb}=0.5 nS where return currents dominate.

We would like to use our computational LFPs to determine how the different inhibitory cell types contribute to theta LFPs as recorded experimentally in the *in vitro* whole hippocampus preparation. As described above, our overall network model (Fig. 6.1A) is intended to capture an intrinsic theta rhythm in the CA1 region of the *in vitro* preparation. CA3 input is not required but local excitatory input which occurs on basal dendrites [161] does need to be included. To do this, we take advantage of previous modeling studies [15, 55] as detailed in the Methods. We would expect that including excitatory input would clearly affect resulting biophysical LFP outputs. Specifically, we would anticipate that the LFP amplitude in SO might decrease even further in the presence of basal excitation, as excitatory and inhibitory BiC inputs could cause mutual cancellations in this region. As return currents mostly exit close to the somatic region where the surface area is larger, the effect of basal excitation might be stronger in SO and SP since most of the current might have exited before reaching SR and SLM. In general, we expect there to be a range of possible LFP characteristics based on the above

LFP computations in the absence of basal excitation. We expect that the addition of excitatory input will influence the LFP in non-intuitive and nonlinear ways and the intuition developed above will be helpful in deciphering and explaining the contribution of the different cell populations.

6.4.2 Constraining synaptic conductances and connection probabilities between BiCs and OLM cells

In this work we focus mainly on OLM cells. The previous model network framework [55] was developed based on the consideration of the recently discovered connections between BiCs and OLM cells [96]. Given this, there are two pathways to consider for how OLM cells could influence ongoing intrinsic theta LFP rhythms. They can influence LFP output indirectly through disinhibition of proximal/middle dendrites of the PYR cell (OLM-BiC-PYR, indirect pathway), or directly through inhibition of distal, apical dendrites of the PYR cell (OLM-PYR, direct pathway). As shown above, many different LFP features can be exhibited in the absence of basal excitation (see Fig. 6.2A,B). It is interesting to note that our biophysical LFP output does not necessarily exhibit theta frequencies, despite being driven by theta frequency EPSC inputs (see Fig. 6.2B(ii)). This is because cancellations in the extracellular space between synaptic inputs and return currents can result in loss or even abolishment of the rhythm. This underscores the importance of modeling biophysical LFPs as the interaction of synaptic and return currents can strongly affect the resulting LFP frequency.

We proceeded to include basal excitation and we perform a full set of computations for all connection probabilities (c_{sb}) and synaptic conductances (g_{sb}, g_{bs}). With these computed biophysical LFPs in hand, we do direct comparisons with experimental LFPs from the whole hippocampus preparation *in vitro*. We classify each set of network parameters as *selected* or *rejected* based on whether our computed LFPs are able to reproduce two robust characteristics exhibited experimentally. These are: (i) the laminar polarity profile exhibits a single dipole with sinks in the basal dendrites and sources in the apical dendrites, and (ii) the frequency of the LFP traces across all layers is in the theta frequency range. These characteristics are shown in Fig. 6.1A. We note that our model is expected to produce theta frequency LFP output due to the experimentally-derived theta frequency EPSCs inserted to the inhibitory cells. However, as we have shown above, the resulting biophysical LFP frequency can be below the theta range due to synaptic and return current interactions and cancellations (see Fig. 6.2B(ii)). Specifically, the frequency of the EPSCs used from experiment is about 5.8 Hz. Thus, in enforcing the theta fre-

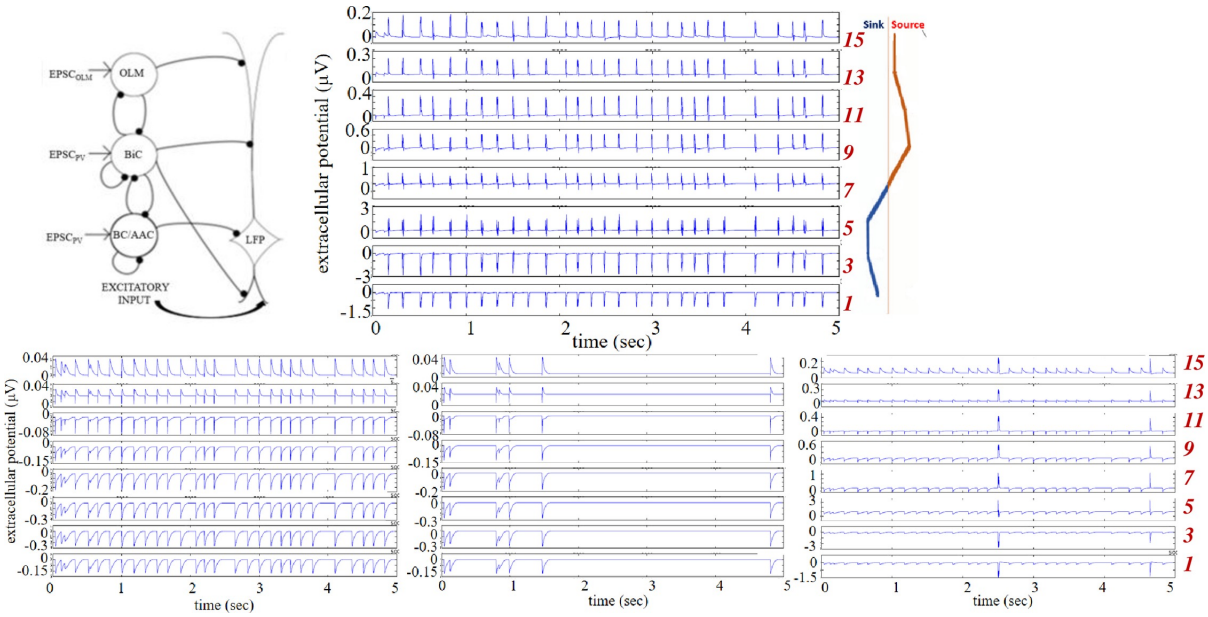

Figure 6.3: Example LFPs from selected and rejected parameter sets. Computed LFPs are shown across multiple layers. **Top:** Selected parameter set: g_{sb}=6, g_{bs}=1.25 nS. **Bottom:** Rejected parameter sets (left to right): g_{sb}=0.5, g_{bs}=0.75 nS; g_{sb}=0.5, g_{bs}=3.5 nS; g_{sb}=2.5, g_{bs}=1 nS. c_{sb}=0.21 for all.

quency on our LFP computations, it is only necessary to impose a lower bound. We used 3 Hz as the lower bound for theta range to be similar to experiment [67]. We applied a peak detection on the LFP trace and used a threshold to avoid detecting baseline peaks. We required that the number of peaks be larger than 15 which, given the 5 sec LFP trace, corresponds to 3 Hz. In Fig. 6.3 (top) we show an example of computed LFPs across the different layers for a parameter set that was selected. The bottom of Fig. 6.3 shows LFP outputs for three different parameter sets that were rejected - incorrect polarities and frequencies are apparent. Note that ordinate resolutions are adjusted across the layers so that the frequency and polarity of computed LFPs can be readily seen in each layer.

We summarize our results in Fig. 6.4 where selected parameter sets are shown in purple and rejected ones in yellow. We observe the following: For low c_{sb}, the plots have a checkered appearance since small changes in g_{sb} and g_{bs} causes the system to alternate between selected or rejected regimes. As c_{sb} increased, there is a clearer separation in (g_{sb}, g_{bs}) parameter space of selected or rejected regimes. This is observed from c_{sb}=0.19 to c_{sb}=0.25. In this range, we consider the system to be robust as it is not very sensitive to synaptic conductance perturbations. However, for c_{sb}=0.19, 0.23 and 0.25, the selected parameter sets are quite narrow. As c_{sb} is further increased, the checkered patterning returns. Note that the selected sets are mainly affected in one direction as c_{sb} changes.

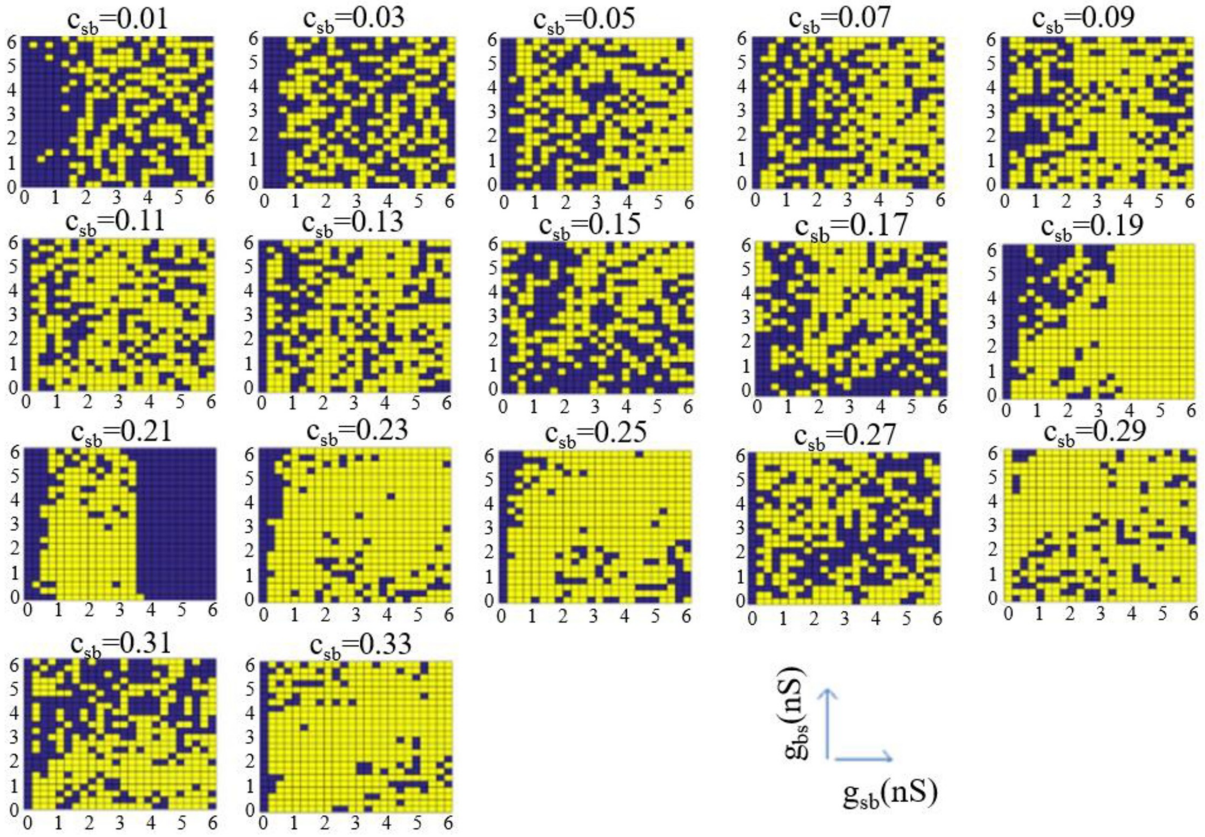

Figure 6.4: All selected and rejected parameter sets. Parameter sets are considered as selected (purple) if computed LFPs match LFPs from experiment in polarity and frequency (3 Hz lower bound). Otherwise, as rejected (yellow). A clear separation in parameter space occurs for $c_{sb} = 0.21$.

That is, across g_{sb} rather than g_{bs} values. Further, we note that in doing this classification, it is more the polarity criteria rather than the frequency criteria of the LFP signal that delineated selected and rejected parameter sets. This is shown in Fig. 6.5 where we do not apply any frequency bounds. While there is some variation in the selected and rejected parameter sets, they are minimal.

Since there is natural variability in biological systems, we assume that sensitivity to small perturbations in parameter values is anathema to having robust LFP theta rhythms. Noting that the synaptic conductance resolution in our simulations is 0.25 nS, we considered that (g_{sb}, g_{bs}) parameter sets that did not yield at least two complete, consecutive rows or columns of purple (selected) were inappropriate for the biological system. That is, variability that is less than the synaptic conductance resolution does not make sense. Looking at this in Fig. 6.4, we first note that there are never at least two complete purple rows for any c_{sb}, but there are cases of two or more complete purple columns, namely, c_{sb}=0.03 and 0.21. However, a complete purple column for g_{sb}=0 is

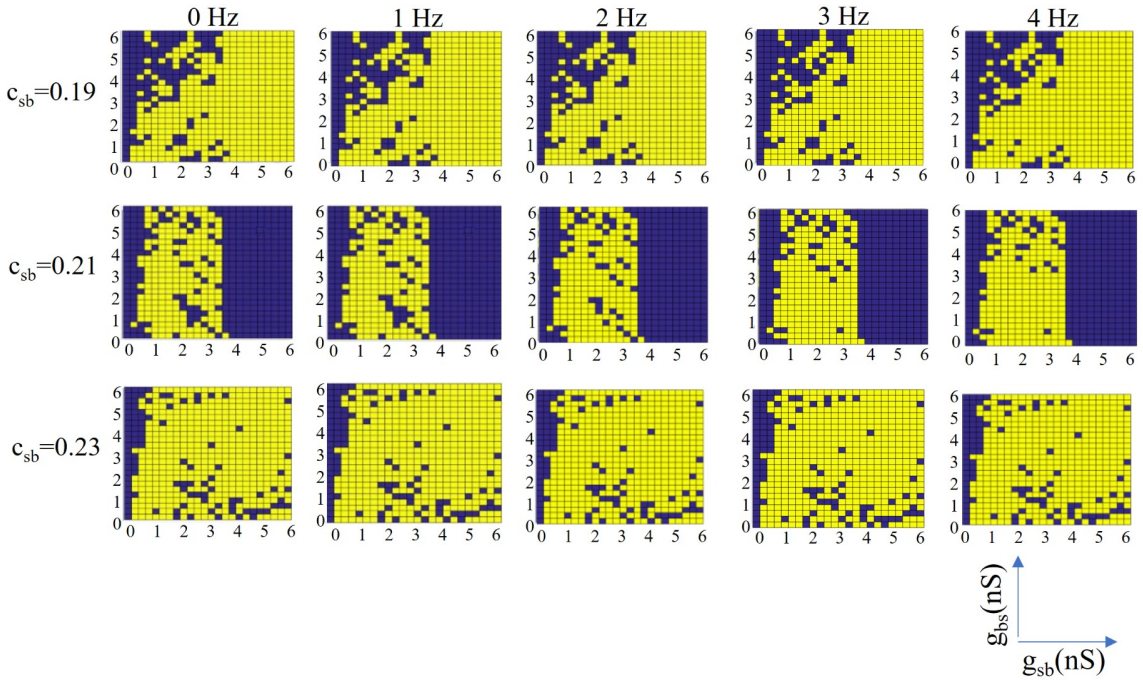

Figure 6.5: Selected and rejected parameter sets using different lower frequency bounds. The different frequency bounds used are shown at the top of each column and only 3 different c_{sb} values are shown. Note that we use 3 Hz as the frequency bound in Fig 6.4

.

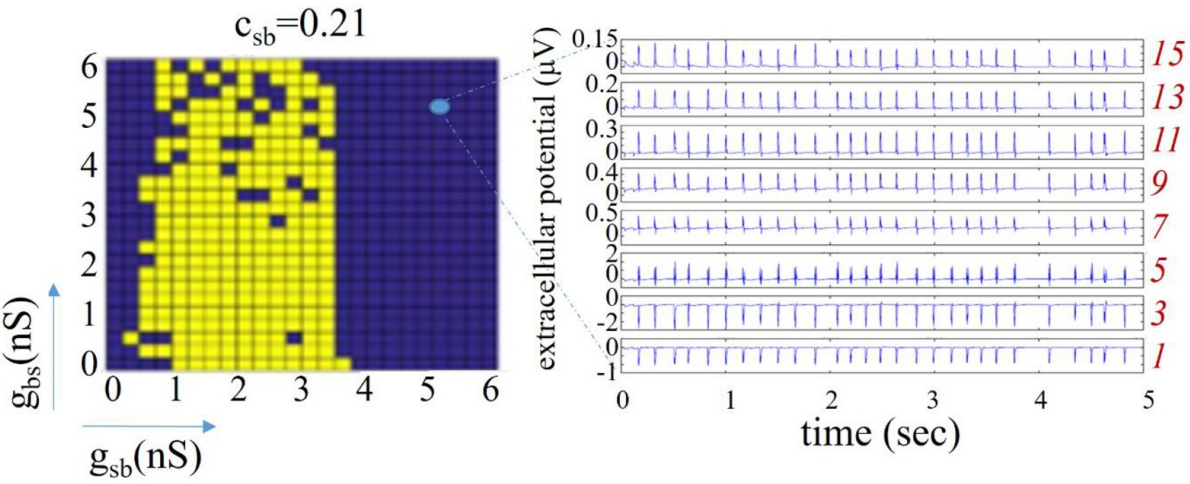

Figure 6.6: Predicted regime. For $c_{sb} = 0.21$, selected parameter sets (purple) include g_{sb} values of 3.5-6 nS, and all g_{bs} values. Rejected sets are in purple. On the right are LFP traces from 8 electrodes for a parameter set of $g_{sb} = 4.75$, $g_{bs} = 4.50$ nS.

invalid since it is known that OLM to BiC connections exist [96]. Thus, c_{sb}=0.03 can be eliminated leaving c_{sb}=0.21 as appropriate. For this connection probability, the transition from selected to rejected networks and vice versa strongly depends on g_{sb} rather than on g_{bs} values, revealing a more important role of the former. In summary, by directly comparing characteristics of our computed biophysical LFPs with those from experiment, we are able to constrain an appropriate connectivity as c_{sb}=0.21, with g_{sb} values of 3.5 to 6 nS, and the full set of g_{bs} values ($g_{sb} \neq 0$, $g_{bs} \neq 0$). We will refer to this set of parameter values as the *predicted* regime. In Fig. 6.6 we show example LFP responses across several layers for a set of parameter values from this *predicted* regime.

6.4.3 OLM cells ensure a robust theta LFP signal, but minimally affect LFP power, and only through disinhibition

Continuing our analysis, we now focus on the constrained parameter sets which we termed the *predicted* regime (c_{sb}=0.21). We decomposed the signals to be able to examine the contribution of the interneuron subtypes to the power of the LFP. We separate our interneuron subtypes into two groups - the PV+ subtypes which are BC/AACs and BiCs, and the SOM+ subtypes which consist of the OLM cells. These two groups were represented by distinct mathematical models of fast-firing PV+ and SOM+ inhibitory cells based on whole cell recordings from the whole hippocampus preparation [55]. We perform spectral analyses of our computed LFPs and use the peak amplitude as a measure of the power of the theta network activity. The peak power is computed for each of the

15 electrodes (i.e., all layers), and we plot the maximum value from all of the layers in the color plots of Fig. 6.7. This is illustrated on the right of Fig. 6.7A. We first simulate the spectral LFP power with all presynaptic inhibitory cell populations present. As shown in Fig. 6.7A, a robust power feature emerges. When all presynaptic origin populations are present, the predicted regime shown in purple in Fig. 6.6, produces LFP responses whose power show minimal variability. This is an interesting observation on its own, as the power of the LFP varies little across hippocampus preparations [67]. Thus, our predicted regime satisfies another characteristic of experimental LFPs. We note that outside of the predicted regime, the LFP output shows much more variability, and the LFP frequency across layers is not necessarily theta, as it is not part of the selected parameter sets. For completeness, we show peak power computations that are done for all connectivities in Fig. 6.8.

To examine the role of the presynaptic origin populations on the LFP we decompose the signal by selectively removing OLM to PYR cell connections or PV+ to PYR cell connections and then computing and plotting the peak power as described above. Selective removal of synapses from PV+ cells to the PYR cell yields an LFP response whose presynaptic origin population is the OLM cell population. The resulting LFP power is low and depends weakly on g_{bs} (Fig. 6.7B). These results show that OLM cells minimally contribute to the signal power as a presynaptic origin population. Viewing this from a broader perspective, these results indicate that disinhibition of non-distal apical dendrites via an indirect (OLM-BiC-PYR) pathway plays a much larger role relative to a direct (OLM-PYR) pathway in producing the LFP power. Along the same lines, disinhibition of distal dendrites through a BiC-OLM-PYR pathway does not have much of an effect on LFP power. Fig. 6.7C shows results of selectively removing the synapses from OLM cells to the PYR cell yielding an LFP response whose presynaptic origin population is the PV+ cell population. Comparison of the signal power in Fig. 6.7C relative to 6.7B shows that the theta power is indeed mainly due to the component from the PV+ cells rather than from the OLM cells. Interestingly, the previously seen robustness in the presence of all presynaptic cell populations (Fig. 6.7A) is now lost. To quantify all of this, we compute the mean and standard deviation (std) of the peak power in the predicted regime for Fig. 6.7A-C. Respectively, they are (mean, std) in units of mV^2/Hz: $(5.1 \times 10^{-9},\ 1.7 \times 10^{-23})$, $(9.7 \times 10^{-10},\ 5.6 \times 10^{-10})$, $(2.6 \times 10^{-8},\ 3.8 \times 10^{-8})$. When all of the cell populations are present, there is minimal variability, and when the PV+ cell populations are removed, the average power decreases five-fold and there is some variability. However, when only PV+ cell populations are present, there is an increase in the average power and the variability is large. It seems clear that the OLM cells do

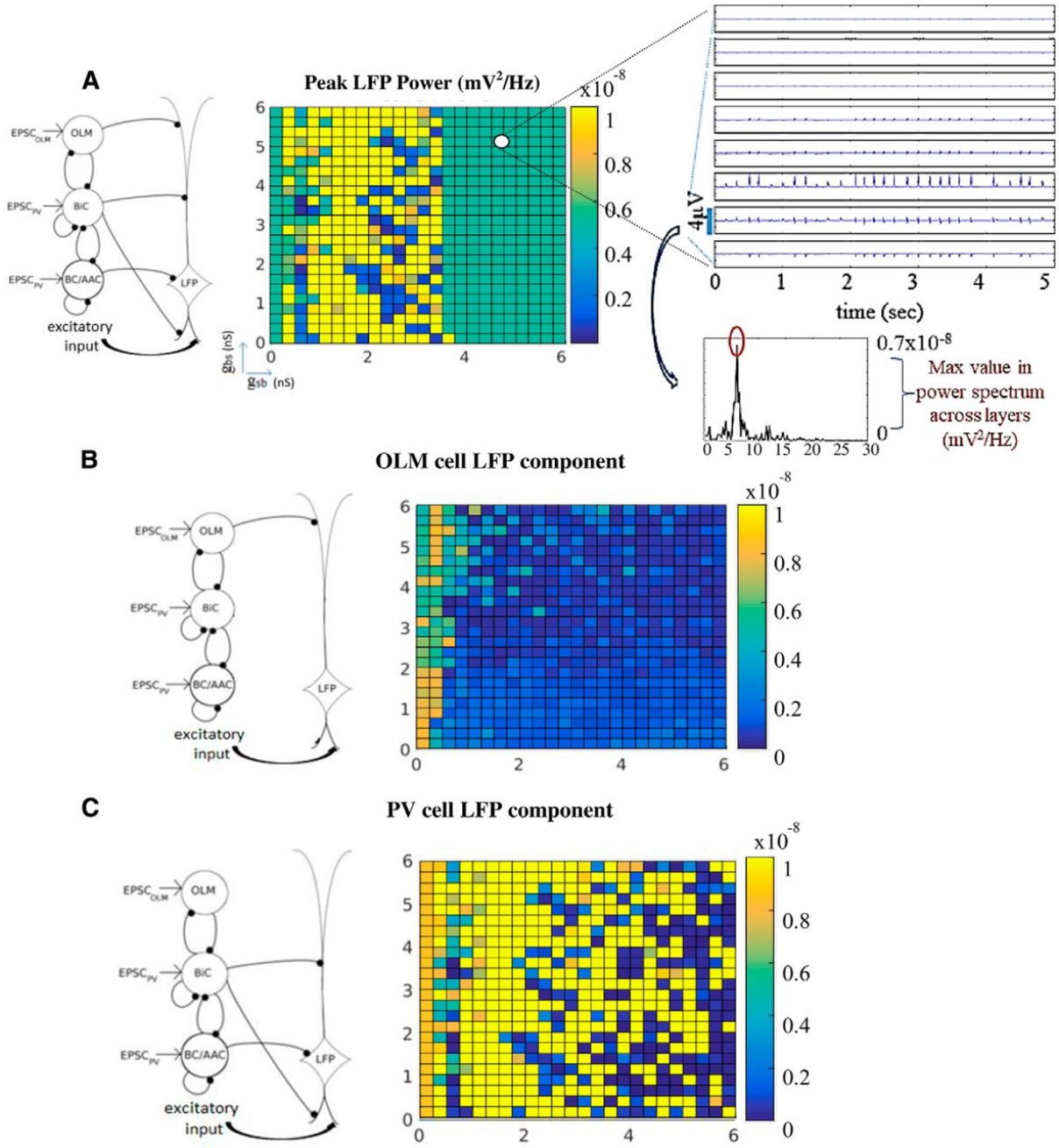

Figure 6.7: Decomposition of the LFP signal. A. All presynaptic cell populations are present. **B.** Only OLM cells are present. **C.** Only BiCs and BC/AACs are present. Schematics on the left show the cell populations projecting to the PYR cell. Computations are done across g_{sb} and g_{bs} parameter values where c_{sb} =0.21. For each parameter set, LFPs are computed across all layers and the power spectrum is computed for each layer. The maximum power across all layers is taken as the peak power and given in the color plot. Computation is illustrated to the right of A (see text for details).

not contribute much to the average LFP power but removing their inputs prominently affects the robustness of the LFP signal. Therefore, we propose that OLM cells have the capacity to regulate robustness of LFP responses without affecting the average power.

As we've mentioned before, Amilhon and colleagues [2] showed that SOM+ cells (putative OLM cells) do not appear to play a prominent role in the generation of intrinsic LFP theta rhythms, since there was only a weak effect on LFP theta power when they optogenetically silenced SOM+ cells. Our results are in agreement with this observation. As shown in Fig. 6.7B, the contribution of OLM cell inputs to the LFP power was small. To make a more accurate comparison with Amilhon and colleagues' OLM cell optogenetic silencing experiments we compared the power of the LFP in the predicted regime in Fig. 6.7A (mean value of $5.1 \times 10^{-9}\ mV^2/Hz$) with the power of the LFP in Fig. 6.7C for g_{sb}=0 and g_{bs}=0 when OLM cell to PYR cell connections were also removed ($8.5 \times 10^{-9}\ mV^2/Hz$). They are clearly comparable. It is interesting to note that it is already apparent from Fig. 6.7A that OLM cells minimally affect LFP power. Consider that for the parameter regime of $g_{sb} = 0$ and across all g_{bs}'s, the LFP power magnitude is the same ($5.1 \times 10^{-9}\ mV^2/Hz$) as the average power of the predicted regime in Fig. 6.7A. In this $g_{sb} = 0$ parameter regime, OLM cell to BiC connections are not present but the OLM cell to PYR cell connections are still present so that OLM cells can still contribute to the LFP response via a direct OLM-PYR pathway. Given that the power does not change indicates that any LFP power contribution due to OLM cells occurs mainly via the indirect OLM-BiC-PYR pathway. Overall, our results show that OLM cells do participate but in such a way that their presence would be unnoticed if one were only measuring LFP power.

To gain insight into how OLM cells affect the robustness of the LFP signal, we further examine our LFP decompositions. With PV+ or OLM cells removed, the impaired LFP output can be grouped into certain categories based on their laminar LFP profiles. In Fig. 6.9 we show the peak power plots for the PV+ cell (Fig. 6.9A) and OLM cell (Fig. 6.9B) decomposition components in which the non-predicted regime is overlaid with gray. For each component, we show three examples of the characterized LFP profiles identified in the groupings. Raster plots that correspond to each cell population are shown above the examples in the figure. It is evident that the different LFP patterns cannot be intuited from the raster plots alone. These examples illustrate the various cases of impaired LFP responses that occur when OLM or PV+ cell connections to the PYR cell are removed.

For the middle LFP response examples (low g_{bs} and high g_{sb}) of Fig. 6.9, we note that OLM cells and BC/AACs have maximal activities and BiCs have minimal activities (see Fig. 6.2C). Thus, synaptic current influences are obvious at the layers where

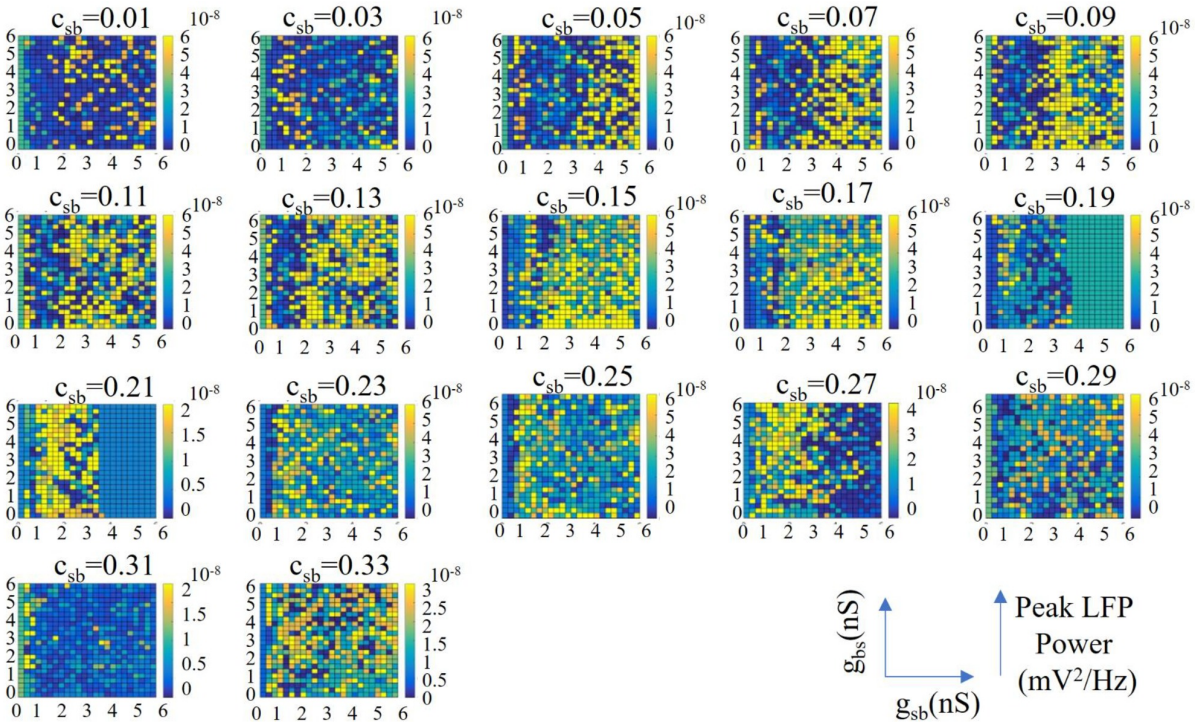

Figure 6.8: Peak power for all conductances and connectivities. Note that the color scale bars are not the same for all the plots. The plot for c_{sb}=0.21 corresponds to Fig 6.7

.

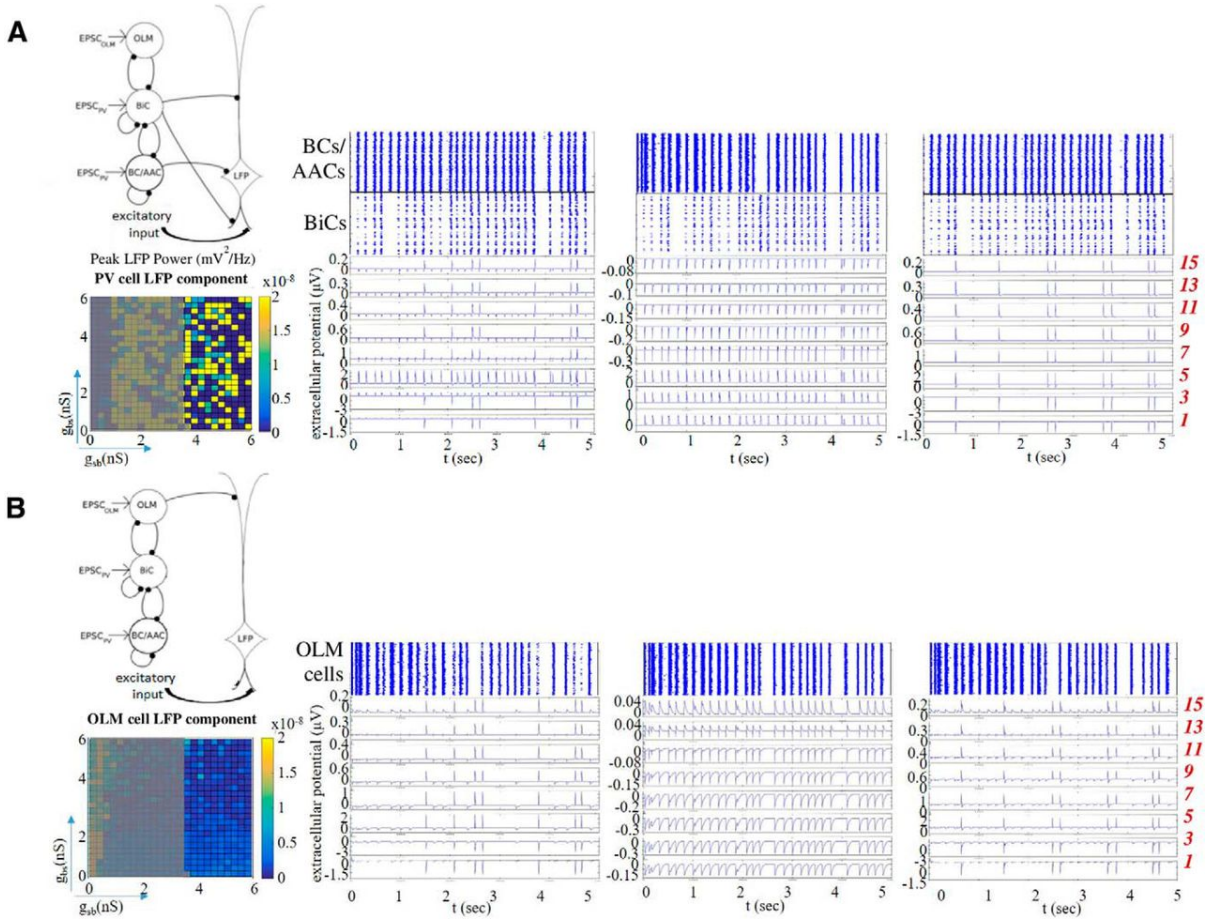

Figure 6.9: LFP pattern examples in predicted regime when only either PV or OLM cell populations are present. Peak power color plots as in Fig 6.7 are shown but with a different color resolution. A gray overlay is added to the plots to emphasize the predicted regime. Three examples of LFP responses (5 sec) across the different layers are shown to illustrate the different patterns observed. For each example, spike rasters for the particular example are shown for PV cells (BiCs and BC/AACs) or OLM cells. **A.** PV cell LFP component. **B.** OLM cell LFP component. Parameter values for left, middle and right columns are respectively: (g_{sb}, g_{bs}) = (5, 2.75), (5.5, 0.5), (5.75, 1) nS.

OLM or BC/AACs contact, while return current influences are obvious at other layers. Inappropriate polarity across the layers is manifest. This pattern of impaired LFP responses occurs in about a quarter of the PV+ cell LFP component parameter sets, and in less than half of the OLM cell LFP component parameter sets. For the PV+ cell LFP component, most of the other parameter sets yield LFP responses in which there is no rhythm, as shown in the right example of Fig. 6.9A. Interestingly, in the rest of the cases (less than a third) there is a loss of rhythmicity in all layers except for the somatic layer as illustrated in the left example. These patterns show that there is an ongoing 'battle' between basal excitation and PV+ cell inputs that can yield a wide range of LFP power values from low (no rhythm - right example) to high (left and middle examples). For the majority of the OLM cell LFP component parameter sets, there is a loss of rhythmicity as shown in the left and right examples of Fig. 6.9B. From the temporal profile and polarity, it is clear that the high amplitude LFP peaks are due to basal excitatory inputs. For larger g_{bs} values, OLM cells are less active (see Fig. 6.2C) and LFP responses across the layers became dominated by peaks due to basal excitation rather than synaptic and return currents due to OLM cells. Overall, cancellations and rhythm loss occurs due to interactions between OLM cells' synaptic and return currents and excitatory inputs. As summarized in the peak power plots of Fig. 6.7C or Fig. 6.9A, PV+ cell inputs alone are not capable of sustaining the robustness throughout the predicted regime and the impaired LFP signals show a large variability. With OLM cell inputs alone, there is low LFP power either because of loss of rhythmicity or because of low amplitude rhythms (Fig. 6.7B or Fig. 6.9B peak power plots).

With and without basal excitation

As one might expect, including basal excitation to incoming inhibitory inputs from different cell populations added to the complexity of untangling nonlinear, interacting components producing the LFP. We relied on our developed intuition when basal excitation was not included (Fig. 6.2A,B) and our LFP decompositions to reveal the different roles that OLM cells and PV+ cells might play in LFP theta rhythms. Specifically, we understand that the loss of LFP rhythm at some layers likely occurs because of having a 'balance' of synaptic and return currents for various conductance values leading to LFP rhythm cancellation or an inappropriate negative polarity domination (see Fig. 6.2A(iii) and B(iii)). Thus, in finding that the LFP power is a robust feature in the predicted regime of synaptic conductance and connection probabilities, we are able to understand that it is critically the OLM cell population that brings about this robust feature. However, this robust feature is apparent only when basal excitation is included. This is clearly

visualized in Fig. 6.10 where we plot the peak power color plots with and without basal excitation when all cells were present or with only OLM cell or PV+ cell LFP components. Removal of basal excitatory inputs in the case when all cells are present (Fig. 6.10, top) leads to a loss of robustness. The mean and std in the predicted regime without basal excitation is $6.2 \times 10^{-9}\ mV^2/Hz$ and $8.0 \times 10^{-9}\ mV^2/Hz$ respectively. While the mean is comparable to when basal excitation is present, the standard deviation is much larger (see values with basal excitation above). Co-activation of inhibition and excitation is clearly important for this robust feature to emerge.

From the LFP decompositions and different LFP patterns expressed (see Fig. 6.7B), and OLM cell activities (see Fig. 6.2C), we understand that the contribution of OLM cells is more dependent on g_{bs} than g_{sb} with the basal excitation affecting the peak power robustness more for larger g_{bs} values. This is apparent in the color variation of the plots of the OLM cell LFP component in Fig. 6.10 (middle). It is larger with basal excitation (left) than without basal excitation (right) for larger g_{bs} values. This is reflected in the mean and std without basal excitation ($5.2\times10^{-10}\ mV^2/Hz$, $2.2\times10^{-10}\ mV^2/Hz$) which was smaller than with basal excitation (see values with basal excitation above). With only the PV+ cell LFP component, the LFP theta rhythm is disrupted as the interactions between basal excitation and PV+ inhibitory inputs are missing the OLM cell inputs. Specifically, the mean and std without basal excitation is ($8.0\times10^{-9}\ mV^2/Hz$, $1.1\times10^{-8}\ mV^2/Hz$) which is smaller than with basal excitation (see values with basal excitation above). In essence, the inclusion of basal excitation can be considered as 'adding' to the magnitude and variance of the LFP power when OLM cells or PV+ cells were examined separately. In combination, a synergistic effect between inhibition and excitation occurs to generate a robust regime - a mean power with minimal variance. From Fig. 6.2C, it can be seen that the PV+ cells (BC/AACs and BiCs) have activities that are more dependent on g_{sb} than on g_{bs}, and that BC/AACs are relatively more active than BiCs in the predicted regime. Thus, at larger g_{bs} values when OLM cells are less active, BC/AACs would contribute more to keep a synergistic balance with the basal excitation.

LFP power across layers

As illustrated in Fig. 6.7A, the color peak power plots are the power in the layer (particular electrode) where the power is maximal. To fully express this, we plot the maximum LFP power across the dendritic tree for all parameter sets in the predicted regime. This is shown in Fig. 6.11A with insets showing the same for the OLM cell (top) and PV+ cell (bottom) LFP components. From this, we see that the maximum LFP power is recorded at electrode 4, and that with only the OLM cell component, the power is dis-

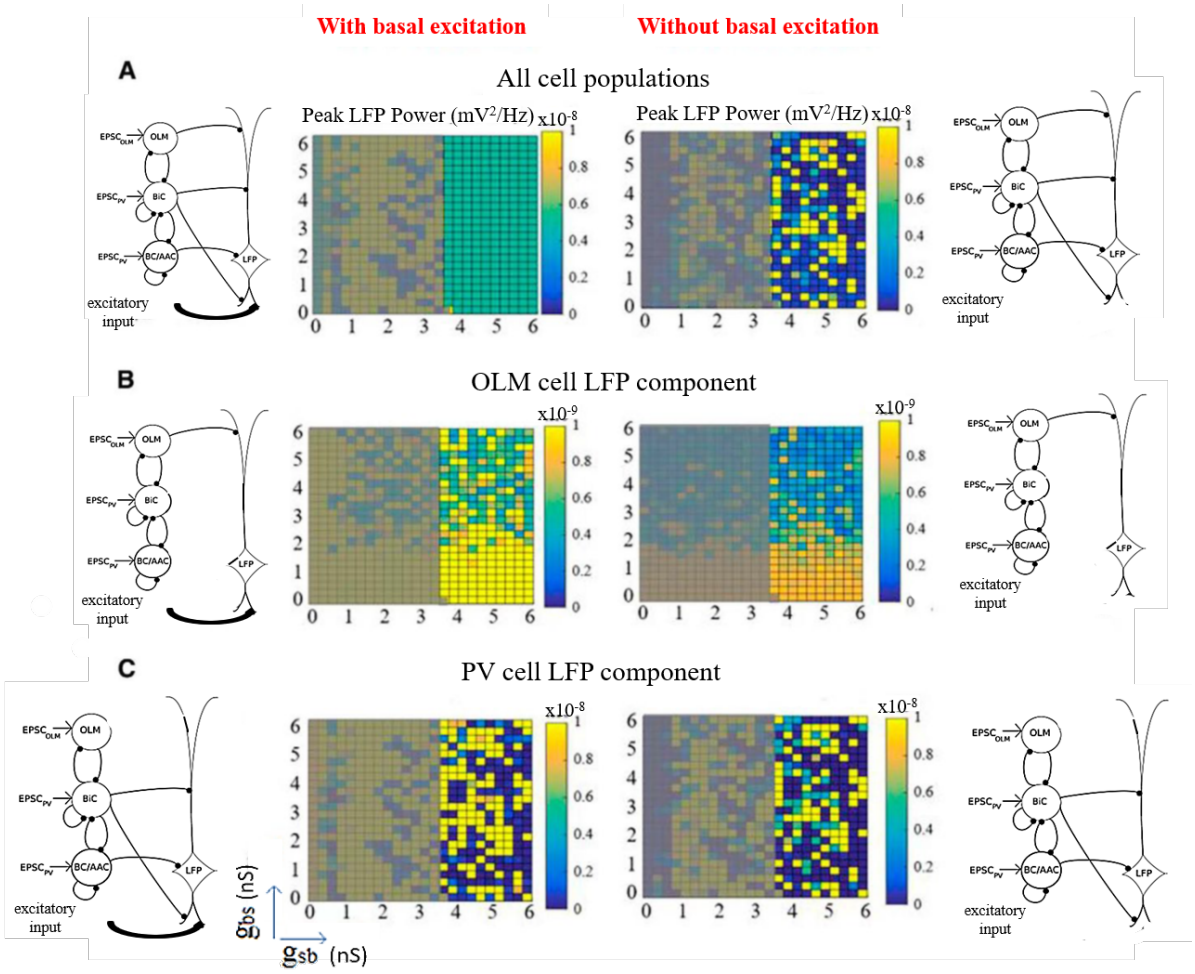

Figure 6.10: Peak power plots with and without basal excitation. The color plots represent peak power as described in Fig 6.7 and with a gray overlay as in Fig 6.9. Note that different color resolutions are used here to facilitate comparison for particular cell populations (i.e., any row). With and without basal excitation is shown on the left and right columns respectively. **Top:** All cell populations. **Middle:** OLM cell LFP component. **Bottom:** PV cell LFP component.

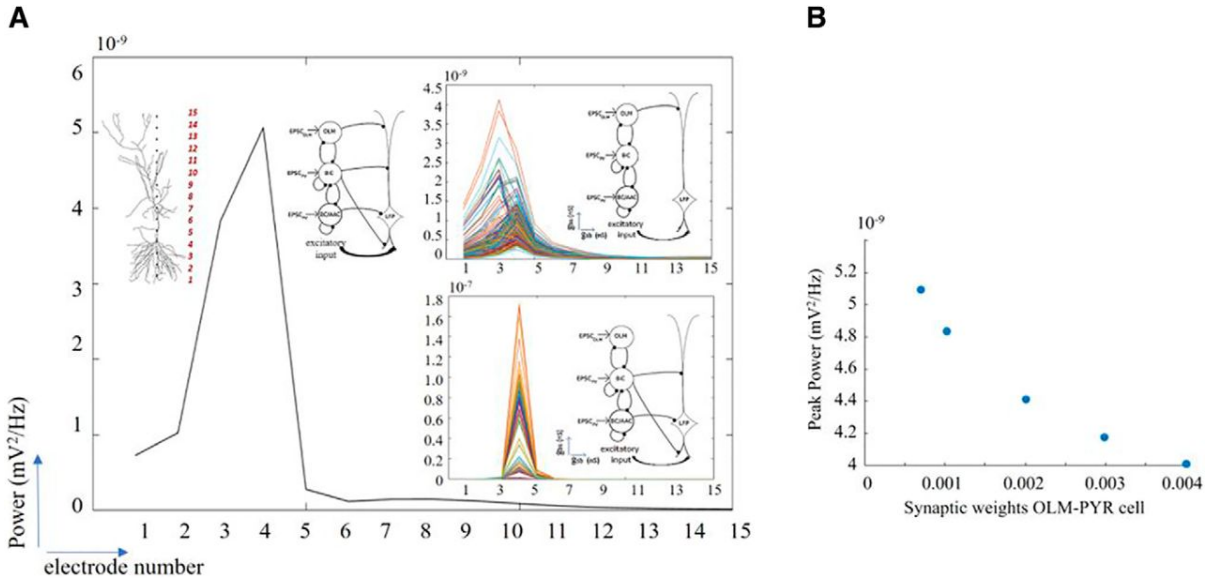

Figure 6.11: Laminar power and peak power changes with changing synaptic weights. A. Computed power at the different electrode locations to show laminar power distribution, for all sets of parameter values in the predicted regime. Top inset: Laminar power for OLM cell LFP component. Bottom inset: Laminar power for PV cell LFP component. Schematics shows the PYR cell model with the 15 extracellular electrodes and the different network configurations. **B.** Changing the synaptic weight from the OLM cells to the PYR cell does not lead to much change in the peak power, as illustrated by the peak power at electrode 4. Parameter values: $g_{sb} = 5.25, g_{bs} = 5.00$ nS. Synaptic weights of 0.00067, 0.001, 0.002, 0.003, 0.004 μS are shown.

tributed more widely and with only the PV+ cell component, more narrowly focused around the soma. This thus shows that the two populations differentially influence the location of LFP maxima. That the LFP power shows no discernible variability when all the cell populations are present, and that there is clear variability when not all of the cell populations are present is obvious in this Fig. 6.11A. We did several additional sets of simulations to explore whether changes in the synaptic weights on the PYR cell would affect whether the robust power feature in the predicted regime would still be present. In all the simulations presented so far, we used synaptic weights that did not bias the effect of one cell population type over the other based on their synaptic input location. So, for example, OLM cell inputs that are the furthest away from the soma, have the largest synaptic weight. In doing this, we are following what was done previously in [55] who used 'unbiased' synaptic weights as well as using the same synaptic weight for all of the cell types. In using the same synaptic weight for all the cell types, we found that the robust power feature in the predicted regime remained (not shown).

As described and shown above, it is already clear that OLM cells via a direct OLM-

PYR pathway minimally contribute to the LFP theta power. To show this directly, we did several, additional simulations where we changed the synaptic weight from OLM cells to the PYR cell. As an example, in Fig. 6.11B we show that increasing the synaptic weight by almost an order of magnitude decreases the peak power by only about 20%.

6.4.4 Estimating the number of PYR cells that contribute to the LFP signal

It is challenging to know how many cells contribute to an extracellular recording. The hippocampus has a regular cytoarchitecture with a nearly laminar, stratified structure of PYR cells [3]. This arrangement together with PYR cells being of similar morphologies and synaptic input profiles allows us to assume that any given PYR cell will generate a similar electric field leading to an additive effect in the extracellular space with multiple cells in resulting LFP dipole recordings. Further, for the *in vitro* intrinsic theta LFP generation considered in this work, the focus can be justified to the couple of synaptic pathways that we explored, and incoming inputs are synchronized amplifying the additive effect.

To estimate how many PYR cells contribute to an extracellular LFP recording in the *in vitro* whole hippocampus preparation, we define the 'spatial reach' of the LFP as the radius around the electrode where the LFP amplitude is decreased by 99%. Using our biophysical computational LFP models with parameter values taken from the predicted regime, we found that the spatial reach is 300 μm as measured extracellularly close to the soma since the LFP decreased from 10,000 nV to 100 nV within this radius. This is shown in Fig. 6.12 where the dotted arrow represents this radius. Therefore, from a "neuron-centric" approach the LFP declined to 1% of its original power within 300 μm. From an "electrode-centric" point of view this means that if we were to place an electrode extracellularly to the soma of a given neuron then that electrode would pick up signal from neurons within 300 μm as any neuron 300 μm further away would contribute to the recorded signal by less than 1% of its maximum power. To estimate the number of cells present within this spatial extent we turned to literature. Taking advantage of detailed quantitative assessment and modeling done by Bezaire and colleagues [15, 14], there are about 311,500 PYR cells in a volume of 0.2 mm^3 of 'stratum pyramidale' tissue (see model specifics in Fig. 1 of [14]). Given our spatial reach radius estimate, a cylindrical volume of stratum pyramidale would be 0.014 mm^3 or about 7% of the total number of PYR cells which is about 22,000. In this way we estimated that there would be about 22,000 PYR cells that contribute to the LFP signal. We note that this would be an upper bound, as

we assumed correlated activity across PYR cells and homogeneous extracellular electrical properties.

6.5 Summary and conclusions

To a large extent, understanding brain function and coding requires that we understand how oscillatory LFP signals are generated [50, 60, 80]. Further, given that particular inhibitory cell populations and abnormalities in theta rhythms are associated with disease states [39], we need to consider how different cell types and pathways contribute to LFP recordings. Ultimately, the challenge is to bring together data from both experimental and modeling LFP studies. In this work, we make steps toward this challenge by gaining insight into the contribution of OLM cells to intrinsic theta rhythms as exhibited by an *in vitro* whole hippocampus preparation.

6.5.1 Summary of results

While it is clear that different interneuron subtypes are involved in theta rhythms [38, 39], it is difficult to untangle the cellular contributions to resulting theta rhythms exhibited in extracellular LFP recordings. That the required circuitry for theta rhythms has been shown to be present in local circuits of the hippocampus [41] is both useful and helpful as it becomes more likely that biophysical LFP models can be linked to a cellular-based circuit understanding of theta rhythms. We took advantage of the *in vitro* whole hippocampus preparation that spontaneously expressed intrinsic theta rhythms [67], and previous inhibitory network models developed for this experimental context [55], to build biophysical LFP models.

The LFP is generated on the basis of transmembrane currents. This means that the LFP is a weighted sum of inward and outward currents. How the LFP changes as a function of location is not trivial. In our work here, when the LFP is governed by synaptic inputs the LFP peaks are narrower since the synaptic inputs are synchronized because of the coherent inhibitory spike rasters. On the other hand, LFP signals governed by return currents would produce LFP peaks that are less narrow as the signal slows down as it travels down the dendrites producing a time lag. This all thus translates to synaptic input location dependencies. Thus, while we can visualize and appreciate the synergistic balances between excitation and inhibition from different cell populations, we note that these combinations are not easily seen as summated balances. Signal decompositions and intuitions from many simulations are required. We leveraged our LFP models to make

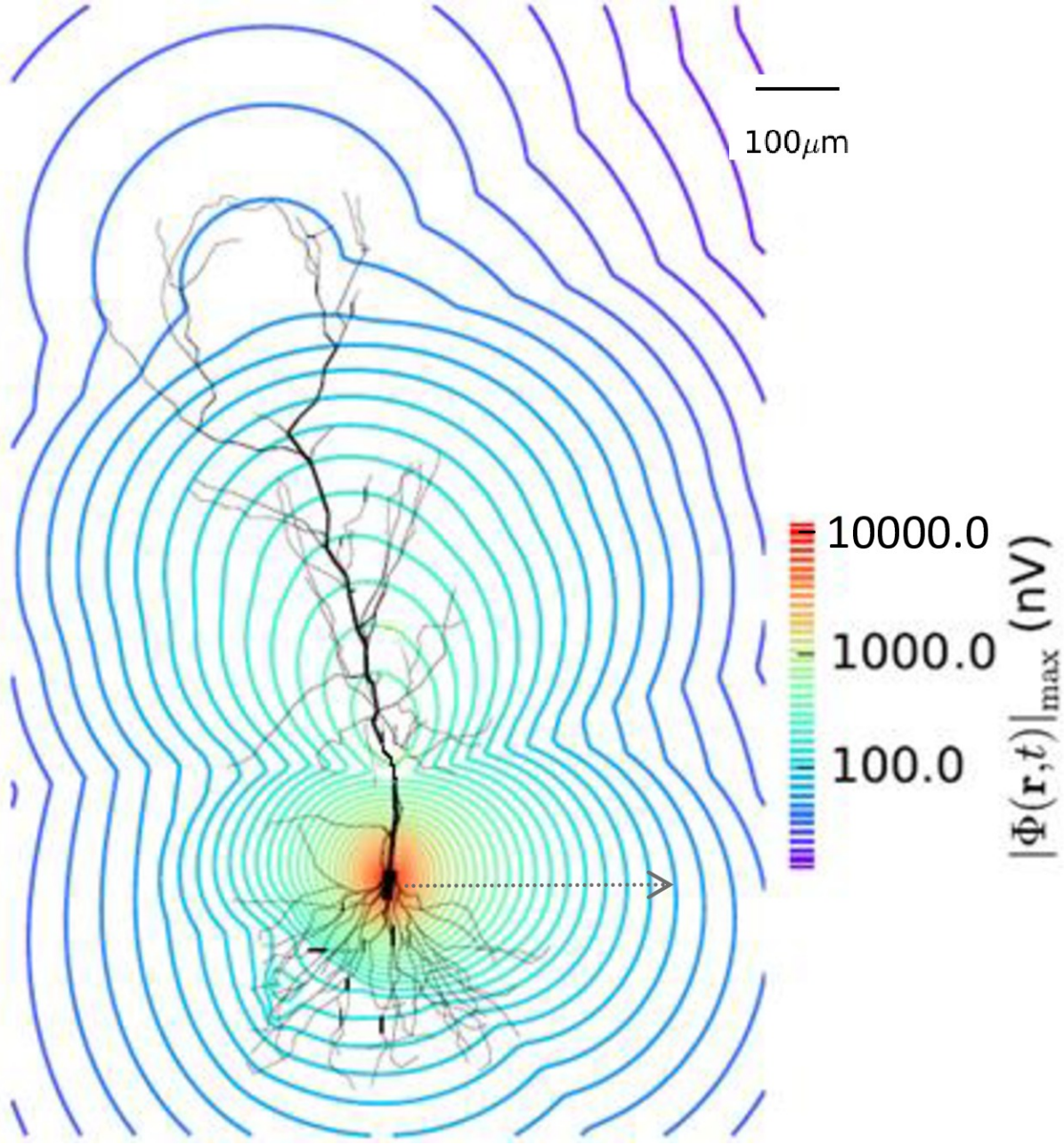

Figure 6.12: Spatial attenuation. We estimated the spatial extent of the generated LFP using our models. PYR cell model morphology is shown with calculated signal decrease from a electrode positioned near the cell soma. The dotted arrow shows the extent of the spatial reach of the signal that is taken as a 99% decrease in the signal, and is approximately 300 μm. Parameter values used are from the predicted regime. g_{sb}=5, g_{bs}=5.75 nS, c_{sb}=0.21.

direct comparison with experimental LFP characteristics. This allowed us to constrain coupling parameters which in turn led us to understand the cellular contribution of interneuron subtypes, specifically OLM cells, to intrinsic theta LFP rhythms.

We showed how the extracellular theta field recorded along the cellular axis of a PYR cell was affected by the magnitude of the inhibitory synaptic currents inserted along its dendritic arbor. Fluctuations in the magnitude of the total inhibitory input occurred due to alterations in synaptic strength balances of the inhibitory networks. Our models exhibited network states in which interactions between OLM cells and BCs could invert the polarity of the recorded signal and produce extracellular potentials of high or low magnitude. We also distinguished regimes where these cellular interactions preserved the frequency of the signal versus those that led to lags or abolishments of the extracellular LFP rhythm. When we applied experimental characteristics of theta frequencies and polarities to our biophysical LFP models, a clear selection emerged and thus we were able to constrain parameter values regarding connectivities. Specifically, we found that the connection probability from OLM cells to BiCs needed to be 0.21 and that synaptic conductances from OLM cells to BiCs had to be larger than 3.5 nS, and we called this the *predicted* regime.

Unexpectedly, we found that this predicted regime also exhibited a robust power output. That is, so long as parameter values were within the predicted regime, the power did not change (Fig 6.7A), and in this regime we saw that BiCs were mostly silenced, BC/AACs were significantly active while OLM cell activity decreased from high to low values as g_{bs} increased (Fig 6.2C). By decomposing the signal we revealed that OLM cell inputs minimally contributed to the LFP power unlike the other cell populations (BiCs and BC/AACs or PV cells). The power of the OLM cell LFP component on its own, although low, showed some variation in the predicted regime (coefficient of variation or CV < 1). On the other hand, the power of the PV cell LFP component was a couple of orders of magnitude higher and showed more variation (CV > 1) in the predicted regime. This indicates that OLM cells contributed to LFP power robustness without contributing to average power whereas PV cells contributed to average power but their effect was more sensitive to perturbations in OLM-BiC interactions. Therefore their contribution was variable. It is however interesting to note that the PV LFP component average power was larger than the average power of the predicted regime with all cells being present. Thus our results indicated that adding OLM cells in the network can overall cause a small decrease in LFP average power as compared to when only PV cells were present and of course induce robustness. It was also interesting to observe that in almost half of the cases the OLM cell LFP component was arrhythmic or non-oscillatory

despite the fact that OLM cells were driven by theta-paced EPSCs. That is, OLM cell inputs alone in most cases were not able to generate a theta LFP signal as recorded in the extracellular space of the PYR cell even though OLM cell populations themselves were firing at theta frequency. Further LFP signal analysis decomposition showed that removing only basal excitation disrupted the robustness of the predicted regime. This suggests that a synergy of OLM cell inputs and basal excitatory inputs as co-activation of distal inhibition and proximal excitation is important to produce robustness in the predicted regime. Overall, an essential aspect in comparing model and experiment LFPs to predict model parameters and decipher cellular contributions was to match sources and sinks at different layers. Thus, having recordings from multiple layers is important.

Morphological details, synaptic locations and related studies

As the main contribution to the LFP is thought to stem from synaptic input to neurons and the subthreshold dendritic processing, various studies have investigated how morphological characteristics and intrinsic resonances shape the features of the LFP signal. In most cases input synapses are activated according to Poissonian statistics [98, 100, 122]. However, in our study here the origin population consisted of point neuron cell representations that had been constrained based on experimental patch clamp recordings from the whole hippocampus preparation. We used a scheme which is a combination of point neuron origin populations and a multi-compartment PYR cell model which served as a processor of synaptic inputs and produced the LFP. This scheme is conceptually very similar to the hybrid scheme proposed in [69].

One factor modulating the amplitude of LFPs was related to the somatodendritic location of synaptic inputs on the PYR cell tree. Different populations of GABAergic interneurons target different dendritic domains and the domain-specific targeting of various interneurons supports the hypothesis of domain-specific synaptic integration in CA1 PYR cells [153]. In CA1 PYR cells, distal and middle apical dendrites comprise two distinct dendritic domains with separate branching connected by a thick apical dendrite. This cytoarchitectonic separation of the cluster of distal dendrites relative to middle and proximal dendrites was shown to critically reduce the effect of distal EPSCs to somatic excitability [154]. The presence of a single apical dendrite with many obliques in stratum radiatum caused a large shunting of EPSCs traveling from the tuft dendrites to the soma. Thus we can appreciate our observation that OLM cells, which target distal dendrites, minimally affected LFP power in stratum pyramidale considering the limited ability of distal inhibition to reach more proximal and somatic regions of the CA1 PYR where

maximum power was recorded. This is not just due to the distal location of these inputs but more due to the cytoarchitectonic separation of the cluster of distal dendrites relative to middle and proximal dendrites. This separation prohibited inhibitory inputs in distal regions from effectively propagating to somatic and proximal regions of CA1 PYR cells and thus being reflected in the extracellular space.

We can further consider our results in light of another theoretical modeling study by [62] which showed that inhibitory inputs can affect excitatory inputs locally and/or globally, depending on the relative locations of the excitatory and inhibitory synapses. In particular this can help us understand the loss of robust power in the predicted regime after removal of OLM cells. The predicted regime consists of different connectivities that generated different spiking patterns that gave rise to fluctuations in inhibitory input in different synaptic locations. First, inhibitory input hyperpolarized the membrane potential, which resulted in shunting of the adjacent dendritic compartments. Activation of excitatory synapses within the shunted compartments will thus generate smaller depolarization, compared with non-shunted dendrites ("local" effect). Second, the local shunting would suppress excitatory input in a nonlinear fashion at locations that were not directly affected by the shunting ("global" effect). Thus, when inhibitory inputs were activated simultaneously with excitatory inputs, the average evoked membrane potential within shunted dendritic compartments should be smaller compared with compartments that had no inhibitory input. At the same time, excitatory effects throughout the entire dendritic tree would be reduced in a nonlinear fashion, and which can be quantified as the change (with versus without inhibitory input) of the trial-to-trial variability of the membrane potential. In our case the activation of excitatory inputs occurred in regions not close by the OLM cell inhibitory inputs, thus the overall power did not increase but the robustness was affected. In [62] the authors examined the spread of shunt level implications using a CA1 reconstructed neuron model receiving inhibition at three distinct dendritic subdomains: the basal, the apical, and the oblique dendrites as innervated by inhibitory synapses. They found that the shunt level spread effectively hundreds of micrometers centripetally to the contact sites themselves spanning from the distal dendrites to the somatic area. This observation thus showed that the somatic area was indeed influenced by shunting inhibition which means that excitatory input non-linearities in our model will be reduced in the presence of global inhibition in the somatic area leading to a decrease in variability and thus robustness in the membrane potential. Of course, the LFP is a measurement of transmembrane currents and not membrane potential. However the reduction of excitatory input mediated non-linearities will also reduce the variability in the distribution of return currents and thus the variability in the LFP.

Limitations and future considerations

Our present study was limited in terms of not considering more inhibitory cell types (e.g., see [14]) and by considering *ongoing* intrinsic theta rhythms since theta frequency inputs were used (Fig 6.1). However, our inhibitory network models were constrained by the experimental context and our less complex model representations enabled us to explore many thousands of simulations and directly compare our biophysical LFPs with experimental LFP features. This aspect was key in allowing us to constrain parameter value sets and to gain insights.

Theta rhythms are foremost generated due to subthreshold activity and dendritic processing of synaptic inputs. Here we used a passive PYR cell model as the spiking component has been shown to mainly contribute to the LFP at frequencies higher than 90Hz [139] while the active voltage-gated channels that were eliminated here were shown to influence LFP characteristics more prominently in frequencies above the theta range [136]. Thus, although the presence of voltage-gated channels will influence the exact distribution of return currents, we thought that it was a reasonable simplification to not include them in this study. Indeed in an additional set of simulation (data not shown) we observed that the presence of h-channels on the PYR cell did not influence the sink-source LFP profile and frequency examined here although it did affect the waveform characteristics.

Another limitation is the usage of a single PYR cell to predict network dynamics. However we note here that since the LFP is a linear summation of the transmembrane currents in the extracellular space (Equation 1), incorporating more PYR cells could result in a linear additive effect in the extracellular space. This would lead to the same LFP profiles as in the case of a single cell only significantly magnified provided that the cells have a similar morphology, physically arborizing in ways that facilitate superposition rather than cancellations of fields, and receive similar presynaptic inputs. Indeed, there is a homogeneous cytoarchitecture disposition of the PYR cells across the CA1 layer [3] and is one of the factors responsible for the extracellular sinks and sources recorded in CA1. Also, PYR cells receive similar presynaptic inputs from the presynaptic populations which project upon the same layers across cells. For this reason we do think that the conclusions derived from the single cell LFP output will remain on the network level to some extent. Of course, important variabilities across PYR cells also exist and considering them in future studies will be important (e.g., see [151]). Therefore careful network modelling will be required to assess the network-generated LFP output.

Extracellular studies suggest that the main current generators of field theta waves are the coherent dendritic and somatic membrane potential fluctuations of the orderly

aligned PYR cells [174, 25, 22]. Thus, distal and local ascending pathways onto PYR cells can in principle contribute to extracellular LFP deflections. To understand theta rhythms one needs to consider the populations projecting onto the PYR cells in CA1. During *in vivo* behaviors, medial septum and entorhinal cortical inputs onto CA1 PYR cells are prominent modulators of the amplitude, phase and waveform features of theta rhythms in conjunction with local inhibitory and excitatory cells. However, spatiotemporal coincidence of inputs makes separation difficult and thus it is challenging to determine cellular contributions to LFP recordings. As there is significant spatiotemporal overlap on PYR cell dendrites across ascending pathways it would be hard to disentangle the cellular composition of these pathways and assess the cellular contribution to theta LFP characteristics. As shown in previous studies [109] blind separation techniques such as Independent Component Analysis produce poor results when trying to disentangle combinations of rhythmic synaptic sources with extensive spatiotemporal overlap. By focusing on intrinsic theta rhythms in the *in vitro* whole hippocampus preparation here, we reduced the spatiotemporal overlap of different pathways and unravelled the cellular composition of the different pathways projecting to the PYR cell. We were thus able to decipher the contribution of OLM cells to intrinsic theta rhythms. This work could potentially be used as a basis to understand OLM cell contributions during *in vivo* theta LFP recordings.

Moving forward we aim to take advantage of the insights gained here to build hypothesis-driven theta generating networks. In this way, we hope to be able to determine the contribution of different cell types and pathways to LFP recordings that are so heavily used and interpreted in neuroscience today.

Chapter 7

Discussion

7.1 Summary

In this thesis we have focused on the generation of theta rhythms in the CA1 hippocampus and we have analyzed the cell-type contributions to these rhythms. In Chapter 3, we considered a piece of the whole CA1, the segment model, and we showed that theta rhythms are initiated by the PYR cells and that their frequency is controlled by the net input the PYR cells receive. In Chapter 4, we considered the segment model embedded in the CA1 network, driven by the rest of the CA1, the EC/CA3 and the recently discovered connections from the SUB, giving rise to the adapted CA1 model. We fitted and then validated the model against available experimental data. Decomposition of external input drives showed that the theta rhythms still emerge if driven separately by these regions. In Chapter 5, we extended the predictions that stemmed from analysis of the segment and adapted models to describe how inhibitory cells contribute to theta rhythms in the full CA1 model with its stronger cellular connectivity and larger cell numbers. Finally in Chapter 6, we focused on the OLM cell population, a strong candidate of theta rhythms, whose contribution to these activities has been ambiguous. We demonstrate the role of the OLM cells in contributing to the robustness of the LFP profile across the CA1 layers, and we compute the reach of the LFP signal.

Overall, our work constitutes a strong foundation from which state-dependent theta and theta-gamma activities in health and disease can be elucidated. The realistic LFP representations that we have used allowed for direct comparisons with experimental data, while considering biophysical models with cell type intricacies and cell diversity offered a fine, micro-level cellular perspective.

7.2 Implications of this work

7.2.1 Alzheimer's disease

AD is an age-related neurodegenerative disorder characterized by progressive memory impairments, leading to global loss of cognitive and executive functions [158]. Accordingly, increasing evidence suggests that oscillatory activity in the theta [168] and gamma [74] is altered in AD patients, and changes in theta oscillations are viewed as a possible predictor for the disease [87]. For example in human studies AD patients showed increased gamma rhythm power and lack of theta power [32], while in mice studies theta-gamma coupling was shown to be impaired [180].

To explore whether fine alterations in hippocampal network activity might be present at the very early stages before amyloid beta overproduction, Goutagny and colleagues [66] used intact hippocampal preparations [67] from young transgenic TgCRND8 mice, following earlier studies in the same preparation [85] which had reported the presence of low/high gamma oscillations coupled with theta. The authors in [66] investigated possible alterations in hippocampal theta and gamma oscillations as well as in the cross-frequency coupling pattern between these two rhythms in AD mice. Their results show that theta oscillations within the distal CA1 area of the hippocampus are impaired early in the TgCRND8 mice, prior to amyloid beta accumulation. In addition, they observed drastic impairments in theta/gamma cross frequency coupling. As the amount of amyloid beta is negligible in 1-month old TgCRND8 mice their data indicated that network alterations are present before amyloid beta overproduction and that theta/gamma coupling may serve as an early electrophysiological signature of hippocampal network dysfunction in animal models of AD.

The PAC mechanism we propose in this thesis can shed light on the observations in [66]. In Chapter 4, we show how the theta and slow gamma LFP rhythms are generated by different mechanisms and as such their power can be modulated separately. The theta rhythm is a PYR cell mediated rhythm, while the slow gamma rhythm relies on the gamma-paced entrainment of the noisy-firing PYR cells. As such, the power of the theta rhythm mainly relies on the strong participation of the PYR cells (assuming that the net input they receive is appropriate to drive their rhythmic theta bursting), while the power of the slow gamma rhythm relies not only on the number of PYR cells firing, but also on the inhibitory connections between gamma bursting inhibitory cells (PV+BCs, AACs, but also CCK+BC) and the PYR cells. As such, if these inhibitory-excitatory connections are impaired, that would have negative effects on the power of the slow gamma rhythm and consequently on theta/gamma PAC.

7.2.2 Epilepsy

Cognitive functions including memory are impaired in numerous other pathologies including temporal lobe epilepsy (TLE). Epilepsy along with AD are two of the most common forms of neurodegenerative disorders characterized by the loss of cells and progressive irreversible alteration of cognitive functions, such as attention and memory.

TLE is the most common and pharmacologically resistant type of adult focal epilepsy. In patients with TLE, a selective and marked degradation of episodic (autobiographic) memory was shown, in which specific memory items are placed within temporal context during encoding and retrieval [47]. Animals with TLE also exhibited a highly specific impairment of the episodic-like memory while preserving other forms of hippocampal-dependent memories [24]. The analysis of hippocampal LFPs in neurosurgical patients during the execution of episodic memory tasks revealed a sharp increase of gamma oscillations before successful item encoding in non-epileptogenic hippocampi. At the same time, the epileptogenic hippocampi exhibited a significant decrease in the gamma band power, which predicts successful item encoding [97]. Thus, typical changes in the gamma band power during this process are reversed for human epileptogenic hippocampus [97]. Besides, it was shown in the TLE model [81] that kainate-treated rats with deficit of episodic-like memory exhibited reduction of hippocampal theta power and coherence along the CA1–dentate axis. In TLE animals, decreased theta coherence in the LFP signals was concentrated between the hippocampal SLM and DG. Inostroza and colleagues [81] claimed that these data point to dis-coordination of hippocampal inputs from layers III and II of the EC and from the contralateral hippocampus as a possible cause for dysfunction of episodic-like memory in TLE animals.

Early diagnosis of these diseases is very important for their successful treatment. Many efforts have been made for defining new biomarkers that would reflect changes of cognitive disturbances within few milliseconds, as well as biomarkers that would detect these diseases at early stages. In that vein, theta/gamma activities are promising biomarker candidates.

7.2.3 Brain stimulation

Considering the role of theta/gamma activities as potential cognitive biomarkers, brain stimulation techniques such as deep brain stimulation (DBS) have been used to induce cognitive enhancement. A number of studies have attempted to enhance memory and cognitive function by stimulating different DBS targets in humans and rodents. Recently, it has been reported that DBS has the ability to activate local and network-wide electrical

effects and modulate oscillatory activities [73]. Additionally, several studies have revealed that DBS may modulate LFPs by phase desynchronization and rhythmic oscillations [45]. In Parkinson's patients, DBS in the basal ganglia has been shown to inhibit beta LFP oscillations in the motor cortex, thereby improving cortical functions [45]. Furthermore, in movement-disorder patients, DBS in the ventral internal capsule/ventral striatum increases theta oscillations in the prefrontal cortex, leading to enhanced performance of cognitive control tasks [173]. In humans, stimulation of the EC served to enhance spatial memory and increase theta oscillations in the hippocampus [159]. In rodents, theta oscillations in the hippocampus were restored by stimulating the fornix, and spatial working memory task performance was improved [17].

7.2.4 Reflections

As it has become evident, alterations in the features of theta/gamma LFPs represent pathological changes in the underlying circuitry. This relation reveals that individuals with 'weak' rhythms are expected to have poor/impaired memory. The strong correlation between theta/gamma rhythms and cognitive performance suggests that the same circuitry that underlies theta generation underlies cognitive functioning. Thus, understanding how theta rhythms are generated could point us to the direction of circuit interventions to help restore cognition in pathologies. Even more, as we unveil the generation mechanism of these rhythms, by extension, we unveil mechanistic aspects of memory.

7.3 Future and ongoing work

As discussed in Chapter 5, OLM cells contribute to the robustness of the LFP laminar profile. One aspect to explore further is the effect of the OLM cells on the laminar profile of the theta LFP in the adapted model in conjunction with inputs from the EC/CA3 and the SUB. This investigation is part of our ongoing work.

As discussed in Chapter 3, the PYR cells-mediated theta generation mechanism involves other intrinsic properties of the biophysical PYR cell models such as the h-channels and the t-type calcium channels [88]. The h-current has been shown to be a pacemaking current which contributes to sub-threshold resonance [18] and has been shown to play an important role in shaping the output of LFP recordings, as determined from multi-compartment LFP modeling studies [122, 123, 146]. How exactly h-channels in PYR cells influence the dynamics and frequency of LFP theta rhythms in CA1 microcircuits will be interesting to investigate further.

Chapter 8

Appendix

8.1 Complementary projects I've worked on and contributed to

Along with Drs. Katie Ferguson and Frances Skinner I've also contributed to the analysis of the minimal model in [53] and I am a co-author in the paper. Additionally, I have written two book Chapters with Dr. Frances Skinner [149, 150].

8.2 Supplementary figures

```
for axoaxoniccell_weight in 0.000000 0.000000 0.000000 0.000000 0.000000
do
        for bistratifiedcell_weight in 0.004500  0.006750 0.009000 0.011250 0.013500
        do
                for cckcell_weight in 0.004500 0.006750 0.009000 0.011250 0.013500
                do
                        for ivycell_weight in 0.000350 0.000525 0.000700 0.000875 0.001050
                        do
                                for ngfcell_weight in 0.000350 0.000525 0.000700 0.000875 0.001050
                                do
                                        for olmcell_weight in 0.000550  0.000825 0.001100 0.001375 0.001650
                                        do
                                                for pvbasketcell_weight in 0.000800 0.001200 0.001600 0.002000 0.002400
                                                do
                                                        for pyramidalcell_weight in 0.000350 0.000525 0.000700 0.000875 0.001050
```

Figure 8.1: The exploration of post-synaptic weights to the PV+BC. The iteration over eight post-synaptic weights yields 390594 configurations.

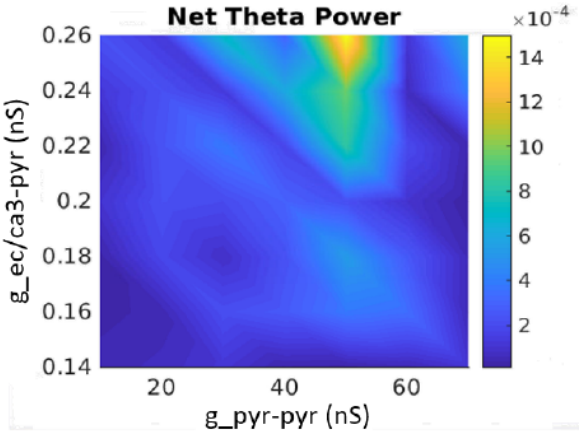

Figure 8.2: Dependence of net theta power on the PYR cells' excitatory drives. Heatmaps of net theta power as a function of $g_{pyr-pyr}$ and $g_{ec/ca3-pyr}$.

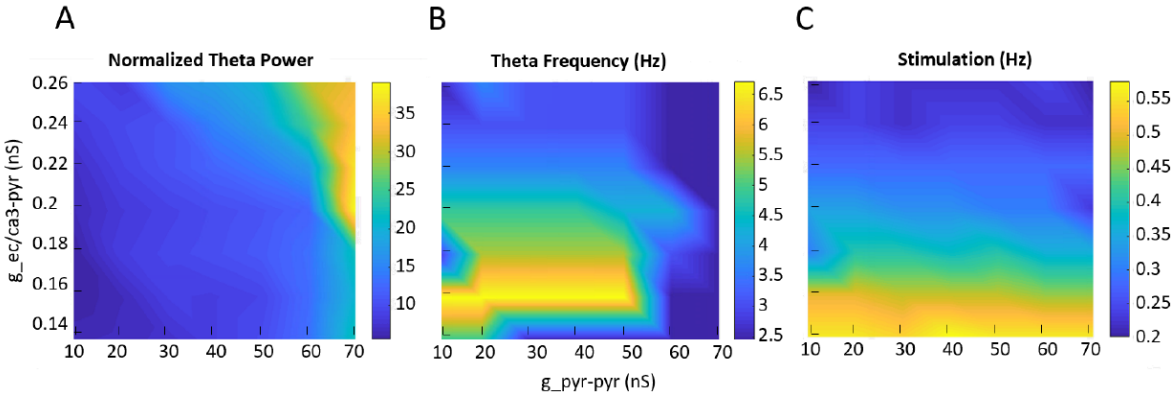

Figure 8.3: Dependence of theta and delta power on the PYR cells' excitatory drives. Heatmaps of A. Normalized power to include both theta and delta power (between 2-12 Hz), as opposed to just theta (3-12 Hz) as shown in Fig. 3.4B, B. frequency and C. afferent input stimulation as a function of $g_{pyr-pyr}$ and $g_{ec/ca3-pyr}$.

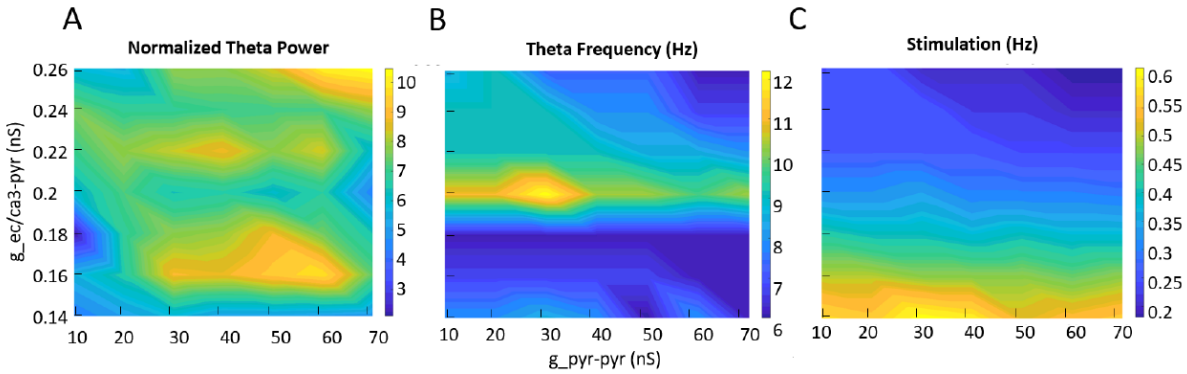

Figure 8.4: Dependence of "high" theta (6-12 Hz) power on the PYR cells' excitatory drives. Heatmaps of A. Normalized "high" theta power, B. frequency and C. afferent input stimulation as a function of $g_{pyr-pyr}$ and $g_{ec/ca3-pyr}$.

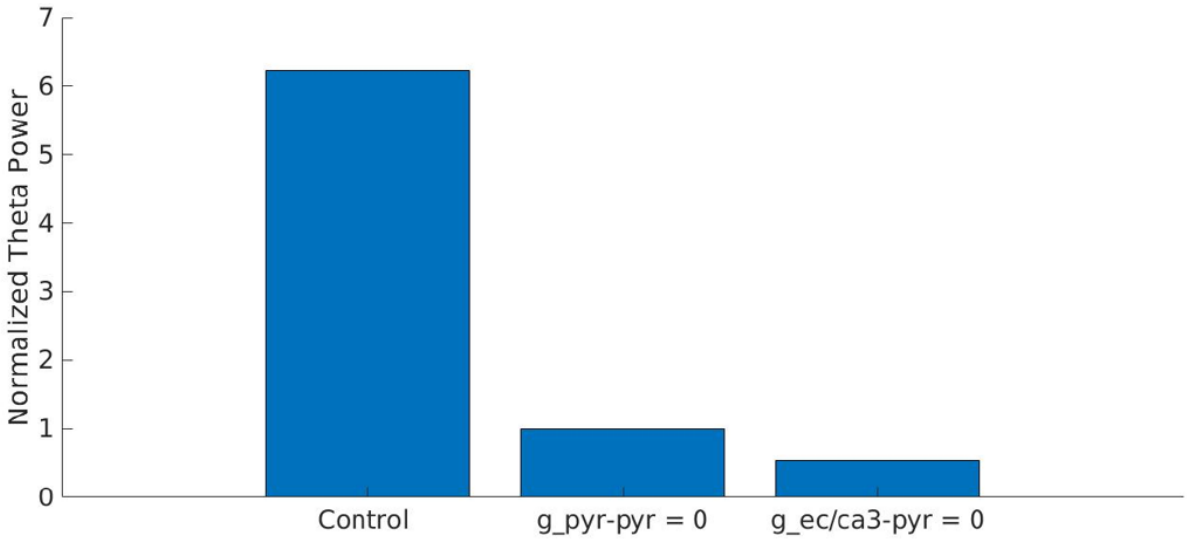

Figure 8.5: Recurrent excitation and feed-forward external drive to the PYR cells is needed for theta rhythms. Normalized theta power of the segment model Fig. 3.3A with parameter values as shown in Fig. 3.3B is eliminated with the removal of feed-forward external drive and recurrent excitation to the PYR cells, i.e., $g_{pyr-pyr}$ and $g_{ec/ca3-pyr}$ set to zero.

Bibliography

[1] David Amaral and Pierre Lavenex. Hippocampal neuroanatomy. In *The hippocampus book*, pages 37–114. Oxford University Press, 2007.

[2] Bénédicte Amilhon, Carey Y. L. Huh, Frédéric Manseau, Guillaume Ducharme, Heather Nichol, Antoine Adamantidis, and Sylvain Williams. Parvalbumin Interneurons of Hippocampus Tune Population Activity at Theta Frequency. *Neuron*, 86(5):1277–1289, June 2015.

[3] Per Andersen, Richard Morris, David Amaral, Tim Bliss, and John O'Keefe. *The Hippocampus Book*. Oxford University Press, USA, 1 edition, November 2006.

[4] Dmitriy Aronov, Rhino Nevers, and David W. Tank. Mapping of a non-spatial dimension by the hippocampal-entorhinal circuit. *Nature*, 543(7647):719–722, 2017.

[5] Giorgio A. Ascoli, Sonia Gasparini, Virginia Medinilla, and Michele Migliore. Local Control of Postinhibitory Rebound Spiking in CA1 Pyramidal Neuron Dendrites. *The Journal of Neuroscience*, 30(18):6434–6442, May 2010.

[6] Oscar J. Avella Gonzalez, Huibert D. Mansvelder, Jaap van Pelt, and Arjen van Ooyen. H-channels affect frequency, power and amplitude fluctuations of neuronal network oscillations. *Frontiers in Computational Neuroscience*, 9, 2015.

[7] Marlene Bartos, Imre Vida, and Peter Jonas. Synaptic mechanisms of synchronized gamma oscillations in inhibitory interneuron networks. *Nature Reviews. Neuroscience*, 8(1):45–56, 2007.

[8] Francesco P. Battaglia, Karim Benchenane, Anton Sirota, Cyriel M.A. Pennartz, and Sidney I. Wiener. The hippocampus: hub of brain network communication for memory. *Trends in Cognitive Sciences*, 15(7):310–318, July 2011.

[9] Agnès Baude, Catherine Bleasdale, Yannis Dalezios, Peter Somogyi, and Thomas Klausberger. Immunoreactivity for the GABAA Receptor α1 Subunit, Somato-

statin and Connexin36 Distinguishes Axoaxonic, Basket, and Bistratified Interneurons of the Rat Hippocampus. *Cerebral Cortex*, 17(9):2094–2107, September 2007.

[10] Maxim Bazhenov, Mark Stopfer, Mikhail Rabinovich, Henry D.I. Abarbanel, Terrence J. Sejnowski, and Gilles Laurent. Model of cellular and network mechanisms for odor-evoked temporal patterning in the locust antennal lobe. *Neuron*, 30(2):569–581, 2001.

[11] Andrei Belitski, Stefano Panzeri, Cesare Magri, Nikos K. Logothetis, and Christoph Kayser. Sensory information in local field potentials and spikes from visual and auditory cortices: time scales and frequency bands. *Journal of Computational Neuroscience*, 29(3):533–545, 2010.

[12] N. Benito, A. Fernández-Ruiz, V. A. Makarov, J. Makarova, A. Korovaichuk, and O. Herreras. Spatial Modules of Coherent Activity in Pathway-Specific LFPs in the Hippocampus Reflect Topology and Different Modes of Presynaptic Synchronization. *Cerebral Cortex*, 24(7):1738–1752, July 2014.

[13] Marianne J. Bezaire, Ivan Raikov, kelly Burk, Caren Armstrong, and Ivan Soltesz. SimTracker tool and code template to design, manage and analyze neural network model simulations in parallel NEURON. *bioRxiv*, 2016.

[14] Marianne J. Bezaire, Ivan Raikov, Kelly Burk, Dhrumil Vyas, and Ivan Soltesz. Interneuronal mechanisms of hippocampal theta oscillation in a full-scale model of the rodent CA1 circuit. *eLife*, 5:e18566, December 2016.

[15] Marianne J Bezaire and Ivan Soltesz. Quantitative assessment of CA1 local circuits: Knowledge base for interneuron-pyramidal cell connectivity. *Hippocampus*, May 2013.

[16] Aanchal Bhatia, Sahil Moza, and Upinder Singh Bhalla. Precise excitation-inhibition balance controls gain and timing in the hippocampus. *eLife*, 8:e43415, April 2019.

[17] Sarah K. B. Bick and Emad N. Eskandar. Neuromodulation for restoring memory. *Neurosurgical Focus*, 40(5):E5, 2016.

[18] Martin Biel, Christian Wahl-Schott, Stylianos Michalakis, and Xiangang Zong. Hyperpolarization-Activated Cation Channels: From Genes to Function. *Physiological Reviews*, 89(3):847–885, January 2009.

[19] Sam A. Booker and Imre Vida. Morphological diversity and connectivity of hippocampal interneurons. *Cell and Tissue Research*, 373(3):619–641, 2018.

[20] James M. Bower and David Beeman. *The Book of GENESIS: Exploring Realistic Neural Models with the GEneral NEural SImulation System.* Springer-Verlag, 2 edition, 1998.

[21] Mark P. Brandon, Andrew R. Bogaard, Christopher P. Libby, Michael A. Connerney, Kishan Gupta, and Michael E. Hasselmo. Reduction of Theta Rhythm Dissociates Grid Cell Spatial Periodicity from Directional Tuning. *Science*, 332(6029):595 –599, April 2011.

[22] Jurij Brankačk, Mark Stewart, and Steven E. Fox. Current source density analysis of the hippocampal theta rhythm: associated sustained potentials and candidate synaptic generators. *Brain Research*, 615(2):310–327, July 1993.

[23] Andres Buehlmann and Gustavo Deco. The neuronal basis of attention: Rate versus synchronization modulation. *Journal of Neuroscience*, 28(30):7679–7686, 2008.

[24] Neil Burgess, Eleanor A. Maguire, and John O'Keefe. The human hippocampus and spatial and episodic memory. *Neuron*, 35(4):625–641, 2002.

[25] Gyorgy Buzsaki and Eduardo Eidelberg. Phase relations of hippocampal projection cells and interneurons to theta activity in the anesthetized rat. *Brain Research*, 266(2):334–339, May 1983.

[26] György Buzsáki. Theta oscillations in the hippocampus. *Neuron*, 33(3):325–340, January 2002.

[27] György Buzsáki, Costas A. Anastassiou, and Christof Koch. The origin of extracellular fields and currents — EEG, ECoG, LFP and spikes. *Nature Reviews Neuroscience*, 13(6):407–420, June 2012.

[28] György Buzsáki and Xiao-Jing Wang. Mechanisms of gamma oscillations. *Annual Review of Neuroscience*, 35:203–225, 2012.

[29] Claude Bédard, Helmut Kröger, and Alain Destexhe. Modeling extracellular field potentials and the frequency-filtering properties of extracellular space. *Biophysical Journal*, 86(3):1829–1842, March 2004.

[30] R. T. Canolty, E. Edwards, S. S. Dalal, M. Soltani, S. S. Nagarajan, H. E. Kirsch, M. S. Berger, N. M. Barbaro, and R. T. Knight. High gamma power is phase-locked to theta oscillations in human neocortex. *Science (New York, N.Y.)*, 313(5793):1626–1628, 2006.

[31] Ryan T. Canolty and Robert T. Knight. The functional role of cross-frequency coupling. *Trends in Cognitive Sciences*, 14(11):506–515, November 2010.

[32] Giuseppe Caravaglios, Giuseppe Castro, Erminio Costanzo, Giulia Di Maria, Danielle Mancuso, and Emma Gabriella Muscoso. Theta power responses in mild alzheimer's disease during an auditory oddball paradigm: lack of theta enhancement during stimulus processing. *Journal of Neural Transmission*, 117(10):1195–1208, 2010.

[33] Nicholas T. Carnevale and Michael L. Hines. *The NEURON Book*. Cambridge University Press, Cambridge, 2006.

[34] Alexandra P Chatzikalymniou, Melisa Gumus, Anton R Lunyov, Scott Rich, Jeremie Lefebvre, and Frances K Skinner. Linking minimal and detailed models of ca1 microcircuits reveals how theta rhythms emerge and how their frequencies are controlled. *bioRxiv*, 2020.

[35] Alexandra P. Chatzikalymniou and Frances K. Skinner. Deciphering the Contribution of Oriens-Lacunosum/Moleculare (OLM) Cells to Intrinsic θ Rhythms Using Biophysical Local Field Potential (LFP) Models. *eNeuro*, 5(4):ENEURO.0146–18.2018, July 2018.

[36] Anastasios Chatzikonstantinou. Epilepsy and the hippocampus. *The Hippocampus in Clinical Neuroscience*, 34:121–142, 2014.

[37] Laëtitia Chauvière. Update on temporal lobe-dependent information processing, in health and disease. *European Journal of Neuroscience*, 51(11):2159–2204, 2020. _eprint: https://onlinelibrary.wiley.com/doi/pdf/10.1111/ejn.14594.

[38] Laura Lee Colgin. Mechanisms and Functions of Theta Rhythms. *Annual Review of Neuroscience*, 36(1):295–312, 2013.

[39] Laura Lee Colgin. Rhythms of the hippocampal network. *Nature Reviews Neuroscience*, 17(4):239–249, April 2016.

[40] Laura Lee Colgin, Tobias Denninger, Marianne Fyhn, Torkel Hafting, Tora Bonnevie, Ole Jensen, May-Britt Moser, and Edvard I. Moser. Frequency of gamma oscillations routes flow of information in the hippocampus. *Nature*, 462(7271):353–357, 2009.

[41] Laura Lee Colgin and Edvard I. Moser. Hippocampal theta rhythms follow the beat of their own drum. *Nature Neuroscience*, 12(12):1483–1484, December 2009.

[42] Laura Lee Colgin and Edvard I. Moser. Gamma oscillations in the hippocampus. *Physiology (Bethesda, Md.)*, 25(5):319–329, 2010.

[43] Vassilis Cutsuridis, Stuart Cobb, and Bruce P Graham. Encoding and retrieval in a model of the hippocampal CA1 microcircuit. *Hippocampus*, 20(3):423–446, March 2010.

[44] Chandan Dasgupta. Mathematical modelling of neurons and neural networks. *Current Science*, 68(2):162–167, 1995.

[45] Coralie de Hemptinne, Nicole C. Swann, Jill L. Ostrem, Elena S. Ryapolova-Webb, Marta San Luciano, Nicholas B. Galifianakis, and Philip A. Starr. Therapeutic deep brain stimulation reduces cortical phase-amplitude coupling in parkinson's disease. *Nature Neuroscience*, 18(5):779–786, 2015.

[46] Olton D.S. and Samuelson R.J. Remembrance of places passed: Spatial memory in rats. *Journal of Experimental Psychology*, 2(2):97–116, 1976.

[47] S. Dupont, P. F. Van de Moortele, S. Samson, D. Hasboun, J. B. Poline, C. Adam, S. Lehéricy, D. Le Bihan, Y. Samson, and M. Baulac. Episodic memory in left temporal lobe epilepsy: a functional MRI study. *Brain*, 123(8):1722–1732, 2000.

[48] András Ecker, Armando Romani, Sára Sáray, Szabolcs Káli, Michele Migliore, Joanne Falck, Sigrun Lange, Audrey Mercer, Alex M. Thomson, Eilif Muller, Michael W. Reimann, and Srikanth Ramaswamy. Data-driven integration of hippocampal CA1 synaptic physiology in silico. *Hippocampus*, n/a(n/a), 2020. _eprint: https://onlinelibrary.wiley.com/doi/pdf/10.1002/hipo.23220.

[49] Gaute T. Einevoll, Alain Destexhe, Markus Diesmann, Sonja Grün, Viktor Jirsa, Marc de Kamps, Michele Migliore, Torbjørn V. Ness, Hans E. Plesser, and Felix Schürmann. The Scientific Case for Brain Simulations. *Neuron*, 102(4):735–744, May 2019.

[50] Gaute T. Einevoll, Christoph Kayser, Nikos K. Logothetis, and Stefano Panzeri. Modelling and analysis of local field potentials for studying the function of cortical circuits. *Nature Reviews Neuroscience*, 14(11):770–785, November 2013.

[51] Arne Ekstrom, Indre Viskontas, Michael Kahana, Josh Jacobs, Kristen Upchurch, Susan Bookheimer, and Itzhak Fried. Contrasting roles of neural firing rate and local field potentials in human memory. *Hippocampus*, 17(8):606–617, 2007.

[52] K. A. Ferguson, F. Njap, W. Nicola, F. K. Skinner, and S. A. Campbell. Examining the limits of cellular adaptation bursting mechanisms in biologically-based excitatory networks of the hippocampus. *Journal of Computational Neuroscience*, 39(3):289–309, October 2015.

[53] Katie A. Ferguson, Alexandra P. Chatzikalymniou, and Frances K. Skinner. Combining Theory, Model, and Experiment to Explain How Intrinsic Theta Rhythms Are Generated in an In Vitro Whole Hippocampus Preparation without Oscillatory Inputs. *eNeuro*, 4(4), August 2017.

[54] Katie A. Ferguson, Carey Y. L. Huh, Benedicte Amilhon, Sylvain Williams, and Frances K. Skinner. Simple, biologically-constrained CA1 pyramidal cell models using an intact, whole hippocampus context. *F1000Research*, June 2015.

[55] Katie A. Ferguson, Carey Y. L. Huh, Bénédicte Amilhon, Frédéric Manseau, Sylvain Williams, and Frances K. Skinner. Network models provide insights into how oriens-lacunosum-moleculare and bistratified cell interactions influence the power of local hippocampal CA1 theta oscillations. *Frontiers in Systems Neuroscience*, 9:110, 2015.

[56] Katie A Ferguson, Carey Y L Huh, Bénédicte Amilhon, Sylvain Williams, and Frances K Skinner. Experimentally constrained CA1 fast-firing parvalbumin-positive interneuron network models exhibit sharp transitions into coherent high frequency rhythms. *Frontiers in computational neuroscience*, 7:144, 2013.

[57] Katie A Ferguson, Carey Y L Huh, Bénédicte Amilhon, Sylvain Williams, and Frances K Skinner. Experimentally constrained CA1 fast-firing parvalbumin-positive interneuron network models exhibit sharp transitions into coherent high frequency rhythms. *Frontiers in Computational Neuroscience*, 7:144, 2013.

[58] Katie A. Ferguson and Frances K. Skinner. Hippocampal theta, gamma, and theta/gamma network models. In Dieter Jaeger and Ranu Jung, editors, *Encyclopedia of Computational Neuroscience*, pages 1340–1352. Springer, 2015.

[59] T. F. Freund and G. Buzsáki. Interneurons of the hippocampus. *Hippocampus*, 6(4):347–470, 1996.

[60] Karl J Friston, André M Bastos, Dimitris Pinotsis, and Vladimir Litvak. LFP and oscillations—what do they tell us? *Current Opinion in Neurobiology*, 31:1–6, April 2015.

[61] Arantius G. De humano foetu. ejusdem anatomico- rum observationum liber, etc. *Venice*, page 44–45, 1587.

[62] Albert Gidon and Idan Segev. Principles Governing the Operation of Synaptic Inhibition in Dendrites. *Neuron*, 75(2):330–341, July 2012.

[63] M. J. Gillies, R. D. Traub, F. E. N. LeBeau, C. H. Davies, T. Gloveli, E. H. Buhl, and M. A. Whittington. A Model of Atropine-Resistant Theta Oscillations in Rat Hippocampal Area CA1. *The Journal of Physiology*, 543(3):779–793, September 2002.

[64] Julijana Gjorgjieva, Guillaume Drion, and Eve Marder. Computational implications of biophysical diversity and multiple timescales in neurons and synapses for circuit performance. *Current Opinion in Neurobiology*, 37:44–52, April 2016.

[65] Shepherd GM. *Foundations of the neuron doctrine*. Oxford University Press., 1978.

[66] Romain Goutagny, Ning Gu, Chelsea Cavanagh, Jesse Jackson, Jean-Guy Chabot, Rémi Quirion, Slavica Krantic, and Sylvain Williams. Alterations in hippocampal network oscillations and theta-gamma coupling arise before amyloid beta overproduction in a mouse model of alzheimer's disease. *The European Journal of Neuroscience*, 37(12):1896–1902, 2013.

[67] Romain Goutagny, Jesse Jackson, and Sylvain Williams. Self-generated theta oscillations in the hippocampus. *Nature Neuroscience*, 12(12):1491–1493, December 2009.

[68] Ning Gu, Jesse Jackson, Romain Goutagny, Germaine Lowe, Frédéric Manseau, and Sylvain Williams. NMDA-dependent phase synchronization between septal

and temporal CA3 hippocampal networks. *Journal of Neuroscience*, 33(19):8276–8287.

[69] Espen Hagen, David Dahmen, Maria L. Stavrinou, Henrik Lindén, Tom Tetzlaff, Sacha J. van Albada, Sonja Grün, Markus Diesmann, and Gaute T. Einevoll. Hybrid Scheme for Modeling Local Field Potentials from Point-Neuron Networks. *Cerebral Cortex (New York, N.Y.: 1991)*, 26(12):4461–4496, December 2016.

[70] M. Hajós, W. E. Hoffmann, G. Orbán, T. Kiss, and P. Erdi. Modulation of septo-hippocampal Theta activity by GABAA receptors: an experimental and computational approach. *Neuroscience*, 126(3):599–610, 2004.

[71] Michael E Hasselmo, Clara Bodelón, and Bradley P Wyble. A proposed function for hippocampal theta rhythm: separate phases of encoding and retrieval enhance reversal of prior learning. *Neural Computation*, 14(4):793–817, April 2002.

[72] Etay Hay, Albert Gidon, Michael London, and Idan Segev. *A theoretical view of the neuron as an input–output computing device*. Oxford University Press, 2016.

[73] Todd M. Herrington, Jennifer J. Cheng, and Emad N. Eskandar. Mechanisms of deep brain stimulation. *Journal of Neurophysiology*, 115(1):19–38, 2016.

[74] C. S. Herrmann and T. Demiralp. Human EEG gamma oscillations in neuropsychiatric disorders. *Clinical Neurophysiology: Official Journal of the International Federation of Clinical Neurophysiology*, 116(12):2719–2733, 2005.

[75] James R. Hinman, Holger Dannenberg, Andrew S. Alexander, and Michael E. Hasselmo. Neural mechanisms of navigation involving interactions of cortical and subcortical structures. *Journal of Neurophysiology*, 119(6):2007–2029, February 2018.

[76] A. L. Hodgkin and A. F. Huxley. A quantitative description of membrane current and its application to conduction and excitation in nerve. *The Journal of Physiology*, 117(4):500–544, 1952.

[77] Gilles Huberfeld, Thomas Blauwblomme, and Richard Miles. Hippocampus and epilepsy: findings from human tissues. *Revue neurologique*, 171(3):236–251, 2015.

[78] Patriclo T. Huerta and John E. Lisman. Heightened synaptic plasticity of hippocampal CA1 neurons during a cholinergically induced rhythmic state. *Nature*, 364(6439):723–725, 1993.

[79] Carey Y. L. Huh, Bénédicte Amilhon, Katie A. Ferguson, Frédéric Manseau, Susana G. Torres-Platas, John P. Peach, Stephanie Scodras, Naguib Mechawar, Frances K. Skinner, and Sylvain Williams. Excitatory inputs determine phase-locking strength and spike-timing of CA1 stratum oriens/alveus parvalbumin and somatostatin interneurons during intrinsically generated hippocampal theta rhythm. *Journal of Neuroscience*, 36(25):6605–6622, 2016.

[80] Alexandre Hyafil, Anne-Lise Giraud, Lorenzo Fontolan, and Boris Gutkin. Neural Cross-Frequency Coupling: Connecting Architectures, Mechanisms, and Functions. *Trends in Neurosciences*, 38(11):725–740, November 2015.

[81] Marion Inostroza, Jorge R. Brotons-Mas, François Laurent, Elena Cid, and Liset Menendez de la Prida. Specific impairment of "what-where-when" episodic-like memory in experimental models of temporal lobe epilepsy. *Journal of Neuroscience*, 33(45):17749–17762, 2013.

[82] E. M. Izhikevich. Simple model of spiking neurons. *IEEE Transactions on Neural Networks*, 14(6):1569–1572, November 2003.

[83] Eugene M. Izhikevich. *Dynamical Systems in Neuroscience: The Geometry of Excitability and Bursting*. The MIT Press, 1 edition, November 2006.

[84] Jesse Jackson, Bénédicte Amilhon, Romain Goutagny, Jean-Bastien Bott, Frédéric Manseau, Christian Kortleven, Steven L. Bressler, and Sylvain Williams. Reversal of theta rhythm flow through intact hippocampal circuits. *Nature Neuroscience*, 17(10):1362–1370, 2014.

[85] Jesse Jackson, Romain Goutagny, and Sylvain Williams. Fast and slow γ rhythms are intrinsically and independently generated in the subiculum. *The Journal of Neuroscience: The Official Journal of the Society for Neuroscience*, 31(34):12104–12117, 2011.

[86] Jorge Jaramillo and Richard Kempter. Phase precession: a neural code underlying episodic memory? *Current Opinion in Neurobiology*, 43:130–138, April 2017.

[87] V. Jelic, S. E. Johansson, O. Almkvist, M. Shigeta, P. Julin, A. Nordberg, B. Winblad, and L. O. Wahlund. Quantitative electroencephalography in mild cognitive impairment: longitudinal changes and possible prediction of alzheimer's disease. *Neurobiology of Aging*, 21(4):533–540, 2000.

[88] Srdjan M. Joksimovic, Pierce Eggan, Yukitoshi Izumi, Sonja Lj Joksimovic, Vesna Tesic, Robert M. Dietz, James E. Orfila, Michael R. DiGruccio, Paco S. Herson, Vesna Jevtovic-Todorovic, Charles F. Zorumski, and Slobodan M. Todorovic. The role of t-type calcium channels in the subiculum: to burst or not to burst? *The Journal of Physiology*, 595(19):6327–6348, 2017.

[89] Ilgam Khalilov, Monique Esclapez, Igor Medina, Djamila Aggoun, Karri Lamsa, Xavier Leinekugel, Roustem Khazipov, and Yehezkel Ben-Ari. A novel in vitro preparation: the intact hippocampal formation. *Neuron*, 19(4):743–749, 1997-10-01.

[90] Tilman J. Kispersky, Fernando R. Fernandez, Michael N. Economo, and John A. White. Spike resonance properties in hippocampal o-LM cells are dependent on refractory dynamics. *Journal of Neuroscience*, 32(11):3637–3651, 2012.

[91] Thomas Klausberger and Peter Somogyi. Neuronal Diversity and Temporal Dynamics: The Unity of Hippocampal Circuit Operations. *Science*, 321(5885):53 –57, July 2008.

[92] Julie Koenig, Ashley N. Linder, Jill K. Leutgeb, and Stefan Leutgeb. The Spatial Periodicity of Grid Cells Is Not Sustained During Reduced Theta Oscillations. *Science*, 332(6029):592 –595, April 2011.

[93] Osung Kwon, Linqing Feng, Shaul Druckmann, and Jinhyun Kim. Schaffer Collateral Inputs to CA1 Excitatory and Inhibitory Neurons Follow Different Connectivity Rules. *Journal of Neuroscience*, 38(22):5140–5152, May 2018.

[94] C. Köhler. Intrinsic projections of the retrohippocampal region in the rat brain. i. the subicular complex. *The Journal of Comparative Neurology*, 236(4):504–522, 1985.

[95] Philip W. Landfield, Ronald J. Tusa, and James L. McGaugh. Effects of posttrial hippocampal stimulation on memory storage and EEG activity. *Behavioral Biology*, 8(4):485–505, 1973.

[96] Richardson N. Leão, Sanja Mikulovic, Katarina E. Leão, Hermany Munguba, Henrik Gezelius, Anders Enjin, Kalicharan Patra, Anders Eriksson, Leslie M. Loew, Adriano B. L. Tort, and Klas Kullander. OLM interneurons differentially modulate CA3 and entorhinal inputs to hippocampal CA1 neurons. *Nature Neuroscience*, 15(11):1524–1530, 2012.

[97] Bradley Lega, John Burke, Joshua Jacobs, and Michael J. Kahana. Slow-theta-to-gamma phase–amplitude coupling in human hippocampus supports the formation of new episodic memories. *Cerebral Cortex*, 26(1):268–278, 2016.

[98] Szymon Leski, Henrik Linden, Tom Tetzlaff, Klas H. Pettersen, and Gaute T. Einevoll. Frequency Dependence of Signal Power and Spatial Reach of the Local Field Potential. *PLoS Comput Biol*, 9(7):e1003137, July 2013.

[99] Henrik Lindén, Espen Hagen, Szymon Leski, Eivind S. Norheim, Klas H. Pettersen, and Gaute T. Einevoll. LFPy: a tool for biophysical simulation of extracellular potentials generated by detailed model neurons. *Frontiers in Neuroinformatics*, 7:41, 2014.

[100] Henrik Lindén, Klas H. Pettersen, and Gaute T. Einevoll. Intrinsic dendritic filtering gives low-pass power field potentials. *Journal of Computational Neuroscience*, 29(3):423–444, December 2010.

[101] John Lisman and György Buzsáki. A neural coding scheme formed by the combined function of gamma and theta oscillations. *Schizophrenia Bulletin*, 34(5):974–980, 2008.

[102] Chris Loken, Daniel Gruner, Leslie Groer, Richard Peltier, Neil Bunn, Michael Craig, Teresa Henriques, Jillian Dempsey, Ching-Hsing Yu, Joseph Chen, L. Jonathan Dursi, Jason Chong, Scott Northrup, Jaime Pinto, Neil Knecht, and Ramses Van Zon. SciNet: Lessons learned from building a power-efficient top-20 system and data centre. *Journal of Physics: Conference Series*, 256(1):012026, 2010.

[103] Evgueniy V. Lubenov and Athanassios G. Siapas. Hippocampal theta oscillations are travelling waves. *Nature*, 459(7246):534–539, May 2009.

[104] L López-Aguado, J. M Ibarz, and O Herreras. Activity-dependent changes of tissue resistivity in the CA1 region in vivo are layer-specific: modulation of evoked potentials. *Neuroscience*, 108(2):249–262, December 2001.

[105] Víctor J. López-Madrona, Elena Pérez-Montoyo, Efrén Álvarez Salvado, David Moratal, Oscar Herreras, Ernesto Pereda, Claudio R. Mirasso, and Santiago Canals. Different theta frameworks coexist in the rat hippocampus and are coordinated during memory-guided and novelty tasks. *eLife*, 2020.

[106] Gianmaria Maccaferri. Stratum oriens horizontal interneurone diversity and hippocampal network dynamics. *The Journal of Physiology*, 562(Pt 1):73–80, January 2005.

[107] Gianmaria Maccaferri, J. David, B. Roberts, Peter Szucs, Carol A. Cottingham, and Peter Somogyi. Cell surface domain specific postsynaptic currents evoked by identified GABAergic neurones in rat hippocampus in vitro. *The Journal of Physiology*, 524(1):91–116, April 2000.

[108] Gianmaria Maccaferri and Chris J. McBain. Long-term potentiation in distinct subtypes of hippocampal nonpyramidal neurons. *Journal of Neuroscience*, 16(17):5334–5343, 1996.

[109] Julia Makarova, Jose M. Ibarz, Valeri A. Makarov, Nuria Benito, and Oscar Herreras. Parallel Readout of Pathway-Specific Inputs to Laminated Brain Structures. *Frontiers in Systems Neuroscience*, 5, 2011.

[110] Frédéric Manseau, Romain Goutagny, Marc Danik, and Sylvain Williams. The hippocamposeptal pathway generates rhythmic firing of GABAergic neurons in the medial septum and diagonal bands: an investigation using a complete septohippocampal preparation in vitro. *The Journal of Neuroscience: The Official Journal of the Society for Neuroscience*, 28(15):4096–4107, April 2008.

[111] Gonzalo Martín-Vázquez, Nuria Benito, Valeri A. Makarov, Oscar Herreras, and Julia Makarova. Diversity of LFPs Activated in Different Target Regions by a Common CA3 Input. *Cerebral Cortex*, 26(10):4082–4100, January 2016.

[112] The MathWorks. Matlab and statistics toolbox release 2019b. *Inc., Natick, Massachusetts, United States.*, 2019.

[113] C. J. McBain and A. Fisahn. Interneurons unbound. *Nature Reviews. Neuroscience*, 2(1):11–23, 2001.

[114] Sarah Melzer and Hannah Monyer. Diversity and function of corticopetal and corticofugal GABAergic projection neurons. *Nature Reviews Neuroscience*, 21(9):499–515, 2020.

[115] Jason W. Middleton, Cyrus Omar, Brent Doiron, and Daniel J. Simons. Neural Correlation Is Stimulus Modulated by Feedforward Inhibitory Circuitry. *Journal of Neuroscience*, 32(2):506–518, January 2012. Publisher: Society for Neuroscience Section: Articles.

[116] Michele Migliore and Rosanna Migliore. Know Your Current I h : Interaction with a Shunting Current Explains the Puzzling Effects of Its Pharmacological or Pathological Modulations. *PLOS ONE*, 7(5):e36867, May 2012.

[117] Joshua N. Milstein and Christof Koch. Dynamic moment analysis of the extracellular electric field of a biologically realistic spiking neuron. *Neural Computation*, 20(8):2070–2084, 2008.

[118] Bratislav Mišić, Joaquín Goñi, Richard F. Betzel, Olaf Sporns, and Anthony R. McIntosh. A Network Convergence Zone in the Hippocampus. *PLoS Comput Biol*, 10(12):e1003982, December 2014.

[119] Rawlins J. Morris R., Garrud P. Place navigation impaired in rats with hippocampal lesions. *Animal Behavior Processes*, 1982.

[120] Edvard I. Moser, Emilio Kropff, and May-Britt Moser. Place cells, grid cells, and the brain's spatial representation system. *Annual Review of Neuroscience*, 31:69–89, 2008.

[121] Andrea Navas-Olive, Manuel Valero, Teresa Jurado-Parras, Adan de Salas-Quiroga, Robert G. Averkin, Giuditta Gambino, Elena Cid, and Liset M. de la Prida. Multimodal determinants of phase-locked dynamics across deep-superficial hippocampal sublayers during theta oscillations. *Nature Communications*, 11(1):1–14, 2020. Number: 1.

[122] Torbjørn V Ness, Michiel W H Remme, and Gaute T Einevoll. Active subthreshold dendritic conductances shape the local field potential. *The Journal of Physiology*, page 3809—3825, April 2016.

[123] Torbjørn V. Ness, Michiel W. H. Remme, and Gaute T. Einevoll. h-Type Membrane Current Shapes the Local Field Potential from Populations of Pyramidal Neurons. *Journal of Neuroscience*, 38(26):6011–6024, June 2018.

[124] Paul L. Nunez and Ramesh Srinivasan. *Electric Fields of the Brain: The Neurophysics of EEG*. Oxford University Press, January 2006.

[125] J. O'Keefe and J. Dostrovsky. The hippocampus as a spatial map. preliminary evidence from unit activity in the freely-moving rat. *Brain Research*, 34(1):171–175, 1971.

[126] John O'Keefe and Lynn Nadel. *The Hippocampus as a Cognitive Map*. Oxford: Clarendon Press, 1978.

[127] Petilla Interneuron Nomenclature Group, Giorgio A. Ascoli, Lidia Alonso-Nanclares, Stewart A. Anderson, German Barrionuevo, Ruth Benavides-Piccione, Andreas Burkhalter, György Buzsáki, Bruno Cauli, Javier Defelipe, Alfonso Fairén, Dirk Feldmeyer, Gord Fishell, Yves Fregnac, Tamas F. Freund, Daniel Gardner, Esther P. Gardner, Jesse H. Goldberg, Moritz Helmstaedter, Shaul Hestrin, Fuyuki Karube, Zoltán F. Kisvárday, Bertrand Lambolez, David A. Lewis, Oscar Marin, Henry Markram, Alberto Muñoz, Adam Packer, Carl C. H. Petersen, Kathleen S. Rockland, Jean Rossier, Bernardo Rudy, Peter Somogyi, Jochen F. Staiger, Gabor Tamas, Alex M. Thomson, Maria Toledo-Rodriguez, Yun Wang, David C. West, and Rafael Yuste. Petilla terminology: nomenclature of features of GABAergic interneurons of the cerebral cortex. *Nature Reviews. Neuroscience*, 9(7):557–568, 2008.

[128] H. Petsche. The quantitative analysis of EEG data. In J. P. Schadé and J. Smith, editors, *Progress in Brain Research*, volume 33 of *Computers and Brains*, pages 63–86. Elsevier, 1970.

[129] K H Pettersen, H Lindén, A M Dale, and G T Einevoll. Extracellular spikes and CSD. In R Brette and A Destexhe, editors, *Handbook of Neural Activity Measurement*, chapter 4, pages 92–135. Cambridge University Press, 2012.

[130] Marcelo Ponce, Ramses van Zon, Scott Northrup, Daniel Gruner, Joseph Chen, Fatih Ertinaz, Alexey Fedoseev, Leslie Groer, Fei Mao, Bruno C. Mundim, Mike Nolta, Jaime Pinto, Marco Saldarriaga, Vladimir Slavnic, Erik Spence, Ching-Hsing Yu, and W. Richard Peltier. Deploying a top-100 supercomputer for large parallel workloads: the niagara supercomputer. In *Proceedings of the Practice and Experience in Advanced Research Computing on Rise of the Machines (learning)*, PEARC '19, pages 1–8. Association for Computing Machinery, 2019.

[131] J Potworowski, W Jakuczun, S Łęski, and D K Wójcik. Kernel current source density method. *Neural Computation*, 24:541 — 575, 2012.

[132] W. Rall and G. M. Shepherd. Theoretical reconstruction of field potentials and dendrodendritic synaptic interactions in olfactory bulb. *Journal of Neurophysiology*, 31(6):884–915, 1968.

[133] Wilfrid Rall. Branching dendritic trees and motoneuron membrane resistivity. *Experimental Neurology*, 1(5):491–527, 1959.

[134] Wilfrid Rall. Theoretical significance of dendritic trees for neuronal input-output relations. *Neural Theory and Modeling*, 1964.

[135] Wilfrid Rall. Time constants and electrotonic length of membrane cylinders and neurons. *Biophysical Journal*, 9(12):1483–1508, 1969.

[136] Michael W. Reimann, Costas A. Anastassiou, Rodrigo Perin, Sean L. Hill, Henry Markram, and Christof Koch. A Biophysically Detailed Model of Neocortical Local Field Potentials Predicts the Critical Role of Active Membrane Currents. *Neuron*, 79(2):375–390, July 2013.

[137] David Robbe and György Buzsáki. Alteration of theta timescale dynamics of hippocampal place cells by a cannabinoid is associated with memory impairment. *Journal of Neuroscience*, 29(40):12597–12605, 2009.

[138] Horacio G Rotstein, Dmitri D Pervouchine, Corey D Acker, Martin J Gillies, John A White, Eberhardt H Buhl, Miles A Whittington, and Nancy Kopell. Slow and fast inhibition and an H-current interact to create a theta rhythm in a model of CA1 interneuron network. *Journal of Neurophysiology*, 94(2):1509–1518, August 2005.

[139] Erik W. Schomburg, Costas A. Anastassiou, György Buzsáki, and Christof Koch. The Spiking Component of Oscillatory Extracellular Potentials in the Rat Hippocampus. *The Journal of Neuroscience*, 32(34):11798–11811, August 2012.

[140] Erik W. Schomburg, Antonio Fernández-Ruiz, Kenji Mizuseki, Antal Berényi, Costas A. Anastassiou, Christof Koch, and György Buzsáki. Theta phase segregation of input-specific gamma patterns in entorhinal-hippocampal networks. *Neuron*, 84(2):470–485, 2014.

[141] William Beecher Scoville and Brenda Milner. Loss of recent memory after bilateral hippocampal lesions. *Journal of Neurology, Neurosurgery and Psychiatry*, 20(1):11–21, 1957.

[142] I. Segev, John Rinzel, and G. M. Shepherd. The theoretical foundation of dendritic function: Selected papers of wilfrid rall with commentaries. *NYU Scholars*, 1994.

[143] Sharay E. Setti, Holly C. Hunsberger, and Miranda N. Reed. Alterations in hippocampal activity and alzheimer's disease. *Translational issues in psychological science*, 3(4):348–356, 2017.

[144] Tristan Shuman, Daniel Aharoni, Denise J. Cai, Christopher R. Lee, Spyridon Chavlis, Lucia Page-Harley, Lauren M. Vetere, Yu Feng, Chen Yi Yang, Irene Mollinedo-Gajate, Lingxuan Chen, Zachary T. Pennington, Jiannis Taxidis, Sergio E. Flores, Kevin Cheng, Milad Javaherian, Christina C. Kaba, Naina Rao, Mimi La-Vu, Ioanna Pandi, Matthew Shtrahman, Konstantin I. Bakhurin, Sotiris C. Masmanidis, Baljit S. Khakh, Panayiota Poirazi, Alcino J. Silva, and Peyman Golshani. Breakdown of spatial coding and interneuron synchronization in epileptic mice. *Nature Neuroscience*, pages 1–10, January 2020.

[145] Joshua H. Siegle and Matthew A. Wilson. Enhancement of encoding and retrieval functions through theta phase-specific manipulation of hippocampus. *eLife*, 3:e03061, July 2014.

[146] Manisha Sinha and Rishikesh Narayanan. HCN channels enhance spike phase coherence and regulate the phase of spikes and LFPs in the theta-frequency range. *Proceedings of the National Academy of Sciences*, 112(17):E2207–E2216, April 2015.

[147] F K Skinner, C Wu, and L Zhang. Phase-coupled oscillator models can predict hippocampal inhibitory synaptic connections. *The European Journal of Neuroscience*, 13(12):2183–2194, June 2001.

[148] Frances K. Skinner. Conductance-based models. *Scholarpedia*, 1(11):1408, 2006.

[149] Frances K. Skinner and Alexandra Chatzikalymniou. Alzheimer's disease: Rhythms, local circuits, and model-experiment interactions. In Vassilis Cutsuridis, editor, *Multiscale Models of Brain Disorders*, Springer Series in Cognitive and Neural Systems, pages 149–156. Springer International Publishing, 2019.

[150] Frances K. Skinner and Alexandra Pierri Chatzikalymniou. Oscillatory dynamics of brain microcircuits. In *Computational Models of Brain and Behavior*, pages 85–98. John Wiley and Sons, Ltd, 2017.

[151] I. Soltesz and A. Losonczy. CA1 pyramidal cell diversity enabling parallel information processing in the hippocampus. *Nature neuroscience*, 21(4):484–493, April 2018.

[152] Ivan Soltesz and Kevin Staley. High times for memory: cannabis disrupts temporal coordination among hippocampal neurons. *Nature Neuroscience*, 9(12):1461–1463, 2006.

[153] Nelson Spruston. Pyramidal neurons: dendritic structure and synaptic integration. *Nature Reviews Neuroscience*, 9(3):206–221, March 2008.

[154] Kalyan V. Srinivas, Eric W. Buss, Qian Sun, Bina Santoro, Hiroto Takahashi, Daniel A. Nicholson, and Steven A. Siegelbaum. The Dendrites of CA2 and CA1 Pyramidal Neurons Differentially Regulate Information Flow in the Cortico-Hippocampal Circuit. *Journal of Neuroscience*, 37(12):3276–3293, March 2017.

[155] Greg J. Stuart and Nelson Spruston. Dendritic integration: 60 years of progress. *Nature Neuroscience*, 18(12):1713–1721, December 2015.

[156] Yanjun Sun, Suoqin Jin, Xiaoxiao Lin, Lujia Chen, Xin Qiao, Li Jiang, Pengcheng Zhou, Kevin G. Johnston, Peyman Golshani, Qing Nie, Todd C. Holmes, Douglas A. Nitz, and Xiangmin Xu. CA1-projecting subiculum neurons facilitate object–place learning. *Nature Neuroscience*, 22(11):1857–1870, 2019.

[157] Yanjun Sun, Amanda Q. Nguyen, Joseph P. Nguyen, Luc Le, Dieter Saur, Jiwon Choi, Edward M. Callaway, and Xiangmin Xu. Cell-type-specific circuit connectivity of hippocampal CA1 revealed through cre-dependent rabies tracing. *Cell Reports*, 7(1):269–280, 2014.

[158] Trey Sunderland, Harald Hampel, Masatoshi Takeda, Karen T. Putnam, and Robert M. Cohen. Biomarkers in the diagnosis of alzheimer's disease: are we ready? *Journal of Geriatric Psychiatry and Neurology*, 19(3):172–179, 2006.

[159] Nanthia Suthana, Zulfi Haneef, John Stern, Roy Mukamel, Eric Behnke, Barbara Knowlton, and Itzhak Fried. Memory enhancement and deep-brain stimulation of the entorhinal area. *New England Journal of Medicine*, 366(6):502–510, 2012.

[160] Bogousslavsky J. Szabo K., Hennerici M.G. *The Hippocampus in Clinical Neuroscience*. Krager, 2014.

[161] Virág T. Takács, Thomas Klausberger, Peter Somogyi, Tamás F. Freund, and Attila I. Gulyás. Extrinsic and local glutamatergic inputs of the rat hippocampal CA1 area differentially innervate pyramidal cells and interneurons. *Hippocampus*, 22(6):1379–1391, 2012.

[162] Alex Tendler and Shlomo Wagner. Different types of theta rhythmicity are induced by social and fearful stimuli in a network associated with social memory. *eLife*, 4:e03614, February 2015.

[163] Marije ter Wal and Paul Tiesinga. Hippocampal oscillations, mechanisms (PING, ING, sparse). In Dieter Jaeger and Ranu Jung, editors, *Encyclopedia of Computational Neuroscience*, pages 1–14. Springer, 2013.

[164] Edward C. Tolman. Cognitive maps in rats and men. *Psychological Review*, 55(4):189–208, 1948.

[165] Adriano B. L. Tort, Mark A. Kramer, Catherine Thorn, Daniel J. Gibson, Yasuo Kubota, Ann M. Graybiel, and Nancy J. Kopell. Dynamic cross-frequency couplings of local field potential oscillations in rat striatum and hippocampus during performance of a t-maze task. *Proceedings of the National Academy of Sciences*, 105(51):20517–20522, 2008.

[166] Gergely Farkas Turi, Wen-Ke Li, Spyridon Chavlis, Ioanna Pandi, Justin O'Hare, James Benjamin Priestley, Andres Daniel Grosmark, Zhenrui Liao, Max Ladow, Jeff Fang Zhang, Boris Valery Zemelman, Panayiota Poirazi, and Attila Losonczy. Vasoactive Intestinal Polypeptide-Expressing Interneurons in the Hippocampus Support Goal-Oriented Spatial Learning. *Neuron*, 101(6):1150–1165.e8, March 2019.

[167] Peter J. Uhlhaas, Frederic Roux, Wolf Singer, Corinna Haenschel, Ruxandra Sireteanu, and Eugenio Rodriguez. The development of neural synchrony reflects late maturation and restructuring of functional networks in humans. *Proceedings of the National Academy of Sciences*, 106(24):9866–9871, 2009.

[168] K. van der Hiele, A. A. Vein, A. van der Welle, J. van der Grond, R. G. J. Westendorp, E. L. E. M. Bollen, M. A. van Buchem, J. G. van Dijk, and H. a. M. Middelkoop. EEG and MRI correlates of mild cognitive impairment and alzheimer's disease. *Neurobiology of Aging*, 28(9):1322–1329, 2007.

[169] Guido Van Rossum and Fred L Drake Jr. *Python reference manual*. Centrum voor Wiskunde en Informatica Amsterdam, 1995.

[170] Xiao-Jing Wang. Pacemaker Neurons for the Theta Rhythm and Their Synchronization in the Septohippocampal Reciprocal Loop. *Journal of Neurophysiology*, 87(2):889–900, January 2002.

[171] M. A. Whittington, R. D. Traub, and J. G. Jefferys. Synchronized oscillations in interneuron networks driven by metabotropic glutamate receptor activation. *Nature*, 373(6515):612–615, 1995.

[172] M. A. Whittington, R. D. Traub, N. Kopell, B. Ermentrout, and E. H. Buhl. Inhibition-based rhythms: experimental and mathematical observations on network dynamics. *International Journal of Psychophysiology: Official Journal of the International Organization of Psychophysiology*, 38(3):315–336, 2000.

[173] A. S. Widge, S. Zorowitz, I. Basu, A. C. Paulk, S. S. Cash, E. N. Eskandar, T. Deckersbach, E. K. Miller, and D. D. Dougherty. Deep brain stimulation of the internal capsule enhances human cognitive control and prefrontal cortex function. *Nature Communications*, 10(1):1536, 2019.

[174] J. Winson. Loss of hippocampal theta rhythm results in spatial memory deficit in the rat. *Science*, 201(4351):160–163, July 1978.

[175] Menno P. Witter and David G. Amaral. Hippocampal formation. *The Rat Nervous System*, pages 635–704, 2004.

[176] Chiping Wu, Hui Shen, Wah Ping Luk, and Liang Zhang. A fundamental oscillatory state of isolated rodent hippocampus. *The Journal of Physiology*, 540(2):509–527, 2002.

[177] Peer Wulff, Alexey A. Ponomarenko, Marlene Bartos, Tatiana M. Korotkova, Elke C. Fuchs, Florian Bähner, Martin Both, Adriano B. L. Tort, Nancy J. Kopell, William Wisden, and Hannah Monyer. Hippocampal theta rhythm and its coupling with gamma oscillations require fast inhibition onto parvalbumin-positive interneurons. *Proceedings of the National Academy of Sciences*, 106(9):3561–3566, 2009.

[178] Chi-Jen Yang, Kuo-Ting Tsai, Nan-Fu Liou, and Ya-Hui Chou. Interneuron diversity: Toward a better understanding of interneuron development in the olfactory system. *Journal of Experimental Neuroscience*, 13:1179069519826056, 2019. Publisher: SAGE Publications Ltd STM.

[179] Honghui Zhang, Andrew J. Watrous, Ansh Patel, and Joshua Jacobs. Theta and Alpha Oscillations Are Traveling Waves in the Human Neocortex. *Neuron*, 98(6):1269–1281.e4, June 2018.

[180] Xiaomin Zhang, Wewei Zhong, Jurij Brankačk, Sascha W. Weyer, Ulrike C. Müller, Adriano B. L. Tort, and Andreas Draguhn. Impaired theta-gamma coupling in APP-deficient mice. *Scientific Reports*, 6:21948.